

AD-A083 780

SCRIPPS INSTITUTION OF OCEANOGRAPHY LA JOLLA CA
MODELS OF THE EQUATORIAL OCEAN CIRCULATION.(U)
1980 M J MCPHADEN

F/8 8/3

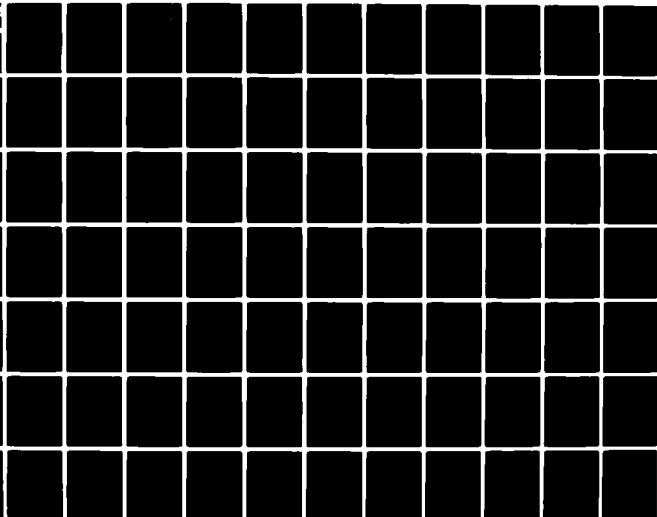
N00014-75-C-0152

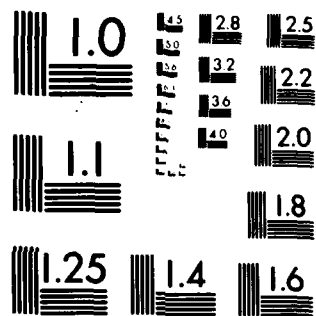
UNCLASSIFIED

NL

1-2

REMARKS





MICROCOPY RESOLUTION TEST CHART
NATIONAL BUREAU OF STANDARDS 1963 A

ADA083780

unclassified

SECURITY CLASSIFICATION OF THIS PAGE (When Data Entered)

REPORT DOCUMENTATION PAGE		READ INSTRUCTIONS BEFORE COMPLETING FORM
1. REPORT NUMBER	2. GOVT ACCESSION NO.	3. RECIPIENT'S CATALOG NUMBER
	AD-A083 780	
4. TITLE (and Subtitle)	5. TYPE OF REPORT & PERIOD COVERED	
(6) MODELS OF THE EQUATORIAL OCEAN CIRCULATION,		
7. AUTHOR(s)	8. CONTRACT OR GRANT NUMBER(s)	
(10) Michael James McPhaden	(15) N00014-75-C-0152	
9. PERFORMING ORGANIZATION NAME AND ADDRESS	10. PROGRAM ELEMENT, PROJECT, TASK AREA & WORK UNIT NUMBERS	
Scripps Institution of Oceanography / La Jolla, CA 92093	(12) 125	
11. CONTROLLING OFFICE NAME AND ADDRESS	13. REPORT DATE	
Office of Naval Research Arlington, VA 22217	(11) 1980	
14. MONITORING AGENCY NAME & ADDRESS (if different from Controlling Office)	14. NUMBER OF PAGES	
(9) Doctoral thesis	121	
	15. SECURITY CLASS. (of this report)	
	unclassified	
	15a. DECLASSIFICATION/DOWNGRADING SCHEDULE	
16. DISTRIBUTION STATEMENT (of this Report)		
Approved for public release. Distribution unlimited.		
17. DISTRIBUTION STATEMENT (of the abstract entered in Block 20, if different from Report)		
18. SUPPLEMENTARY NOTES		
Doctoral Dissertation		
19. KEY WORDS (Continue on reverse side if necessary and identify by block number)		
20. ABSTRACT (Continue on reverse side if necessary and identify by block number)		
<p>In this dissertation I investigate equatorial ocean dynamics using analytical and simple numerical models. The steady circulation is first examined using a linear equatorial beta-plane formulation in which continuous density stratification is a key element. The basin is horizontally unbounded and forced by either winds or a surface temperature boundary condition. Two vertically diffusive models are proposed to examine the effects...</p>		

FORM 1 JAN 73 1473

EDITION OF 1 NOV 65 IS OBSOLETE
S/N 0102-LF-014-6601

329200
SECURITY CLASSIFICATION OF THIS PAGE (When Data Entered)

UNIVERSITY OF CALIFORNIA

C

San Diego

Models of the Equatorial Ocean Circulation

A dissertation submitted in partial satisfaction of the
requirement for the degree Doctor of Philosophy
in Oceanography

by

Michael James McPhaden



Committee in charge:
Professor Myrl C. Hendershott, Co-Chairman
Doctor Robert A. Knox, Lecturer, Co-Chairman
Professor Richard L. Salmon
Professor Robert L. Parker
Professor Sinai Rand

1980

Accession For	
NTIS	GRA&I
DDC	TAB
Unannounced	
Justification	
By	
Distribution/	
Availability Codes	
Dist	Avail and/or special
A	

The dissertation of Michael James McPhaden is approved, and it is acceptable in quality and form for publication on microfilm:

Richard L Salmon

Eric R...

Ree Parke

Robert A. Kew

Co-Chairman

Myrl C Hendershott

Co-Chairman

University of California, San Diego

1980

To Christine

for her encouragement and understanding

and

To my parents, William and Irene

for a lifetime of patience

TABLE OF CONTENTS

	Page
List of Symbols	vi
List of Figures and Tables	viii
Acknowledgments	xi
Vita, Publications and Fields of Study	xii
Abstract.	xiv
 I Introduction.	 1
 II Steady State Models	 5
A. Observational Background	5
B. Previous Theories	8
1. Constant Density Models	9
2. Stratified Models	12
C. Newtonian Cooling Model.	16
1. Formulation	16
2. Zonal Winds	27
3. Variation of Parameters	47
4. Meridional Winds.	60
5. Discussion.	64
D. Biharmonic Friction Model.	71
1. Formulation	71
2. Zonal Winds	74
3. Thermal Forcing	79
4. Discussion.	83

	Page
III Equatorial Kelvin and Inertio-gravity Waves in Zonal Shear Flow	85
References	102

LIST OF COMMONLY USED SYMBOLS

x, y, z	Longitude, latitude, depth
u, v	Zonal, meridional velocity perturbation
w	Vertical velocity perturbation
p	Pressure perturbation
$\theta, \bar{\theta}, \bar{\theta}_z$	Temperature perturbation, background temperature, background vertical temperature gradient
U, V, P	Vertically integrated velocities and pressure
q, Q	Generalized dependent variable and its depth integral
$\tau, \tau^{(x)}, \tau^{(y)}$	Wind stress and its zonal, meridional components
ρ_0	Average density of seawater (1 g cm^{-3})
g	Gravitational acceleration ($9.8 \times 10^2 \text{ cm sec}^{-2}$)
α	Coefficient of thermal expansion ($2.5 \times 10^{-4} \text{ }^\circ\text{C}^{-1}$)
f	Coriolis parameter
β	Meridional gradient of planetary vorticity ($2.3 \times 10^{-13} \text{ cm}^{-1} \text{ sec}^{-1}$)
A, K	Eddy momentum and heat diffusivities
H	Depth of the ocean
D	Depth scale
L	Length scale
u, w	Horizontal, vertical velocity scales

P	Pressure scale
T	Temperature scale
τ_0	Wind stress scale
γ	Meridional decay scale of surface forcing
ℓ, ℓ_0	Zonal wavenumber
i	$(-1)^{\frac{1}{2}}$
n, H_n, ψ_n	Hermite index, polynomial, function
y_t	Turning latitude
ϕ	Depth dependence
j	Dispersion index
$m_{n,j}$	Complex vertical wavenumber
$(a_{n,j}) \vec{A}$	(One element of) amplitude vector of ψ_n
$(b_n) \vec{B}$	(One element of) vector projection of surface forcing onto ψ_n
\vec{C}	Coefficient matrix for boundary conditions
N	Upper limit of n
Pr	Prandtl number
C_{xz}	Slope of constant phase lines on x - z plane
w_e	Ekman pumping velocity
D_e	Ekman depth
D_g	Depth scale of geostrophic flow
D_T	Depth scale of the background temperature field
S	Measure of relative importance of stratification vs. rotation

LIST OF FIGURES AND TABLES

	Page
Figure 1. (a) Meridional section of zonal velocity at 170°E. (b) Corresponding meridional section of temperature. (after Hisard, <i>et al.</i> , 1970).	6
Figure 2. Profiles of zonal velocity at the equator computed from the constant density models of (a) Stommel (1960) and (b) Charney (1960).	11
Figure 3. A plot of $\text{Im}(m^2)$ vs. λ from the dispersion relation (12).	26
Figure 4. (a) Meridional and (b) longitudinal variations of zonal wind.	29
Figure 5. Depth profiles of perturbation variables on the equator.	31
Figure 6. Depth profiles of perturbation variables outside the equatorial boundary layer.	33
Figure 7a. Meridional section of zonal velocity.	34
Figure 7b. Meridional circulation corresponding to the zonal velocity section shown in Figure 7a.	35
Figure 8. Zonal velocity on the equatorial plane.	36
Figure 9. Meridional section of deep zonal velocity.	38
Figure 10. Meridional sections of (a) zonal and (b) meridional Ekman velocity.	41
Figure 11. Balance of forces at the sea surface computed from just the Ekman modes in the (a) zonal and (b) meridional direction.	42

	Page
Figure 12. Balance of forces at the sea surface computed from all modes excluding the Ekman modes in the (a) meridional and (b) zonal direction.	45
Figure 13. Depth profiles of perturbation variables on the equator computed from just the Kelvin mode.	46
Figure 14. Percentage of zonal wind stress that projects onto the Ekman, Kelvin and geostrophic modes as a function of nondimensional latitude.	48
Figure 15. Effects of varying zonal wavenumber (ℓ_0) on (a) zonal velocity at the equator and (b) width of the equatorial current system.	51
Table 1. Power law dependence of various scales on diffusivity (A,K) and stratification ($\bar{\theta}_z$).	52
Figure 16. Effects of varying diffusivity (A,K) on (a) zonal velocity at the equator and (b) width of the equatorial current system.	54
Figure 17. Effects of varying stratification ($\bar{\theta}_z$) or Prandtl number (Pr) on (a) zonal velocity at the equator and (b) width of the equatorial current system.	55
Figure 18. Approximate solution computed from just the Kelvin mode on the equator.	59
Figure 19. Depth profiles of perturbation variables in the equatorial boundary layer for southward winds.	61
Figure 20. Meridional circulation in the equatorial boundary layer for southward winds.	63

	Page
Figure 21. Nonlinear tendencies as a function of nondimensional latitude at the depth of the EUC core.	68
Figure 22. Meridional section of total temperature.	69
Figure 23. Depth profiles of perturbation variables on the equator for the biharmonic friction model.	76
Figure 24. Meridional section of zonal velocity for the biharmonic friction model.	77
Figure 25. Meridional section of total temperature for the biharmonic friction model.	78
Figure 26. Depth profiles of perturbation variables on the equator for surface temperature forcing.	81
Figure 27. Balance of forces at the sea surface for surface temperature forcing computed from just the Ekman modes in the (a) zonal and (b) meridional direction.	82

ACKNOWLEDGMENTS

The text of this dissertation in part is a reprint of material as it appears in the *Journal of Physical Oceanography*. The coauthor listed in that publication, Dr. Robert A. Knox, directed and supervised the research which forms the basis for this dissertation. His academic and scientific guidance over the past 5 years have been much appreciated.

I would like to thank all the members of my doctoral committee for their encouragement and advice in the development of this work. I am especially indebted to Dr. Julian P. McCreary of Nova University for his many hours of enthusiastic and stimulating discussion.

Jane Malloy, Ruth, Jeannie and Renate all deserve mention for their help in preparing the manuscript. Annette Pickens typed the original draft to Chapter III and brewed the coffee every morning. Moral support was provided by the La Jolla Hash House Harriers and the Scripps Ghetto.

I am likewise grateful for financial support provided by the Office of Naval Research under Contract N00014-75-C-0152.

VITA

October 22, 1950 - Born - Buffalo, New York

- | | |
|-----------|--|
| 1973- | B.S., Physics, State University of New York
at Buffalo |
| 1973-1974 | Science Instructor, Saint John the Baptist School,
Kenmore, New York |
| 1974-1980 | Research Assistant
Scripps Institution of Oceanography
University of California, San Diego |
| 1980- | Doctor of Philosophy |

PUBLICATIONS

"Equatorial Kelvin and Inertio-gravity Waves in Zonal Shear Flow"
(with R. A. Knox), *J. Phys. Oceanogr.*, 9, pp. 263-277, 1979.

FIELDS OF STUDY

Major Field: Physical Oceanography

Studies in Physical Oceanography
Professors R.S. Arthur, C.S. Cox, R.E. Davis,
M.C. Hendershott, W.H. Munk and J.L. Reid

Studies in Fluid Mechanics
Professor R.E. Davis

Studies in Geophysical Measurements
Professor R.A. Haubrich

Studies in Applied Mathematics
Professors S. Rand and F.A. Williams

Studies in Marine Geology
Professors W.H. Berger, J.R. Curaray and H.W. Menard

Studies in Marine Chemistry
Professor J.M.T.M. Gieskes

Studies in Marine Biology
Professors R.R. Hessler, J.A. McGowan, M.M. Mullin,
W.A. Newman and R.H. Rosenblatt

ABSTRACT OF THE DISSERTATION

Models of the Equatorial Ocean Circulation

by

Michael James McPhaden

Doctor of Philosophy in Oceanography

University of California, San Diego, 1980

Professor Myrl C. Hendershott, Co-Chairman

Doctor Robert A. Knox, Lecturer, Co-Chairman

In this dissertation I investigate equatorial ocean dynamics using analytical and simple numerical models. The steady circulation is first examined using a linear equatorial beta-plane formulation in which continuous density stratification is a key element. The basin is horizontally unbounded and forced by either winds or a surface temperature boundary condition. Two vertically diffusive models are proposed to examine the effects of different turbulence parameterizations. One is characterized by temperature dissipation proportional to temperature itself, the other has biharmonic friction proportional to a fourth

derivative of velocity. Both lead to equations for the steady state that are in many ways analogous to the well-known equations governing equatorial wave motion. The analogies are exploited both in obtaining analytical solutions and in describing the flow dynamics.

Steady zonal winds drive geostrophic flows such as the Equatorial Undercurrent and South Equatorial Current as well as equatorial upwelling and a weakening of the equatorial thermocline. Examination of the dynamics reveals that in a stratified ocean equatorial Ekman layers are well behaved due to the presence of meridional baroclinic pressure gradients. These pressure gradients are not geostrophically balanced and therefore imply an error of $O(10\%)$ or greater in the geostrophic calculation of near surface zonal currents from the density field. Furthermore, the geostrophic balance is modified near the equator to allow for direct wind forcing and vertical diffusion of zonal momentum. Nonlocal wind effects are important in the model results suggesting a possible dynamical connection between maximum westward winds in the central equatorial Pacific and maximum undercurrent speeds in the eastern Pacific. Nonlinearity is important in the zonal momentum balance, but its effects on the undercurrent can be qualitatively predicted by quadratic corrections to the linear model. The above results apply to either turbulence parameterization scheme; only the magnitude of various flow quantities changes.

Large scale meridional winds or zonal winds with meridional shear excite a frictional response that is too shallow to displace deeper geostrophic zonal flows off the equator. Thus either time dependence or strong nonlinearity must be invoked to account for observations of an undercurrent structure asymmetric about the equator. Surface zonal tem-

perature gradients drive a current system similar to that driven by zonal winds suggesting that the equatorial mixed layer will have a significant impact on the deeper circulation.

The interaction of prescribed geostrophic zonal mean currents in an equatorial ocean with free, neutrally stable Kelvin and inertio-gravity waves is investigated next. The equations are formulated for a two layer ocean, then solved either analytically or by simple numerical methods. It is found that the zonal velocity of inertio-gravity waves is strongly affected in regions where mean currents have a large meridional shear. This coupling can be interpreted as mean current meanders similar to those observed during GATE. Conversely, sea level fluctuations proportional to wave pressure are not as greatly influenced by mean currents. These results may be of importance when attempting to fit equatorial wave theories to sea level observations on one hand and current measurements on the other.

Solutions in the Kelvin wave range indicate that at low frequencies, the presence of mean currents leads to a small meridional wave velocity and a Doppler shift in frequency. This latter effect may influence the speed at which the equatorial ocean adjusts to transient forcing. At higher frequencies, the Kelvin wave becomes more gravity-like and may appear in current records as varicose meanders of the mean flow.

CHAPTER I

INTRODUCTION

The equatorial ocean has been a continuing source of interest to oceanographers since the first modern observations of the Pacific Equatorial Undercurrent in 1952 (Montgomery and Stroup, 1962). This strong eastward current flows below a generally westward wind drift and extends no further than 2° latitude from the equator. Similar undercurrents were discovered shortly thereafter in both the Indian Ocean during the Northeast Monsoon (Taft and Knauss, 1967) and the Atlantic (Neumann, 1960). Even more subsurface structure emerges from recent analyses. Taft *et al.* (1973) summarize evidence for a persistent westward flow below the permanent undercurrents; Tsuchiya (1975) and Cochrane *et al.* (1979) describe eastward subsurface countercurrents flanking this westward flow. Luyten and Swallow (1976) and Luyten and Eriksen (1980) have observed zonal jets trapped near the equator down to 4000 m. In addition to this rich spatial structure, there is a full spectrum of geophysically interesting temporal fluctuations. For example, evidence of a sea level signal at periods of 4-5 days exists in the equatorial Pacific (Wunsch and Gill, 1975). Undercurrents have meandered about the equator at periods of 0(10 days) in both the Atlantic (Düing *et al.*, 1975) and

Pacific (Titov, 1977). At longer time scales, the equatorial Indian and Pacific Oceans respond to seasonal monsoon forcing. Interannually, large scale coupled ocean-atmosphere disturbances known as El Niño occur.

Daunted by the variety and complexity of oceanic phenomena, Melville wrote in 1851, "...the secrets of the currents in the seas have never yet been divulged, even to the most erudite research...". But through technological advances, systematic observations and the study of dynamical models, we have in the last 30 years gained a wealth of insight into the peculiar physics of the equatorial ocean. For instance, it has been possible to identify some of the important mechanisms that generate and maintain the undercurrent system. Likewise, linear equatorial wave theory (Moore and Philander, 1977) is a unified, elegant paradigm for describing a wide range of time dependent phenomena. From this body of research, two fundamental concepts emerge. First, the equatorial ocean is unique dynamically because horizontal Coriolis forces, of primary importance in mid-latitude flows, vanish at the equator. Second, vertical structure near the equator depends intimately on density stratification.

From a broader perspective, progress in equatorial oceanography moves us closer to understanding the ocean-atmosphere-biosphere complex and its impact on human affairs. For example, in some years a sudden warming of waters off the Peruvian coast devastates the anchovy fishery and produces torrential rains in a normally arid region. These events known as El Niño appear to be related to large scale wind fluctuations thousands of kilometers to the west in the Central Pacific (McCreary, 1977). A better understanding of such events could alleviate many of their adverse social, political and economic effects. Also primary productivity, the base of the food chain, is strongly linked to

upwelling which brings nutrient rich water to the surface. Nowhere outside of coastal regions are there as intense large scale vertical velocities as at the equator. Knowledge of the factors that control the spatial and temporal aspects of equatorial upwelling (and other vertical transport processes e.g., mixing) is thus of paramount importance in understanding the productivity of this region. Finally in the tropics, incident solar energy exceeds outgoing radiative flux. The excess is transported poleward by atmospheric and oceanic processes that create weather and climatic variability. Recent studies (e.g. Shukla, 1975; Reiter, 1978) suggest that equatorial current and temperature structures are key elements in the generation of this variability not only in the tropics but also at temperate latitudes.

In this dissertation I examine the physics of steady state and time variable flows in linearized, stratified, equatorial beta-plane models. Chapter II begins with a discussion of observations pertinent to the steady models and a brief review of previous theories. I then develop two models for steady flow in a continuously stratified ocean to illustrate the boundary layer nature of the equatorial regime and the transition from equatorial to mid-latitude dynamics. The basic conclusions are that (a) stratification removes singularities in the equatorial extension of Ekman layers, (b) mid-latitude geostrophy is modified near the equator to include vertical diffusion of zonal momentum and (c) zonal winds near the equator enter the ocean not through the Ekman layer but through direct projection onto geostrophic currents. It is also shown that (d) stratification is crucial in setting the scales of various flow parameters and that (e) baroclinic zonal pressure gradients are essential for the maintenance of vertical structure. Moreover these results apply for different

turbulence parameterizations. Chapter III is a study of the interaction of free waves and prescribed zonal shear flows like the undercurrent and westward South Equatorial Current. Stratification in this model is approximated by a single jump in density near the surface. The important results of this section are (a) internal equatorial waves can cause mean current meanders like those observed in the Pacific and Atlantic and (b) mean flow, depending on its direction, can either enhance or retard the oceanic response time to transient wind forcing near the equator.

CHAPTER II

STEADY STATE MODELS

A. Observational Background

Figure 1 presents the structure of zonal flow and temperature on a meridional plane in the western Pacific from Hisard *et al.* (1970). The basic pattern is representative of steady conditions at other longitudes in the Pacific and Atlantic Oceans. It consists of (a) an eastward Equatorial Undercurrent (EUC) in the upper thermocline at speeds of $O(100 \text{ cm sec}^{-1})$, (b) a westward surface flow, the South Equatorial Current (SEC) at speeds typically of $O(50 \text{ cm sec}^{-1})$, (c) a weaker westward Equatorial Intermediate Current (EIC) below the EUC and (d) subsurface countercurrents (SSCC) flanking the EIC and at this longitude contiguous to the shallower EUC. The North Equatorial Countercurrent (NECC) is visible at the northern extreme of the section. All these zonal currents are in geostrophic balance with the density field which, to zeroth order, is determined by the temperature field of Figure 1b. In particular, the EUC is associated with a weakening of the thermocline near the equator and the SSCC's are in balance with the plunging 10° isotherm located symmetrically at 3°N and 3°S . A secondary eastward flow which

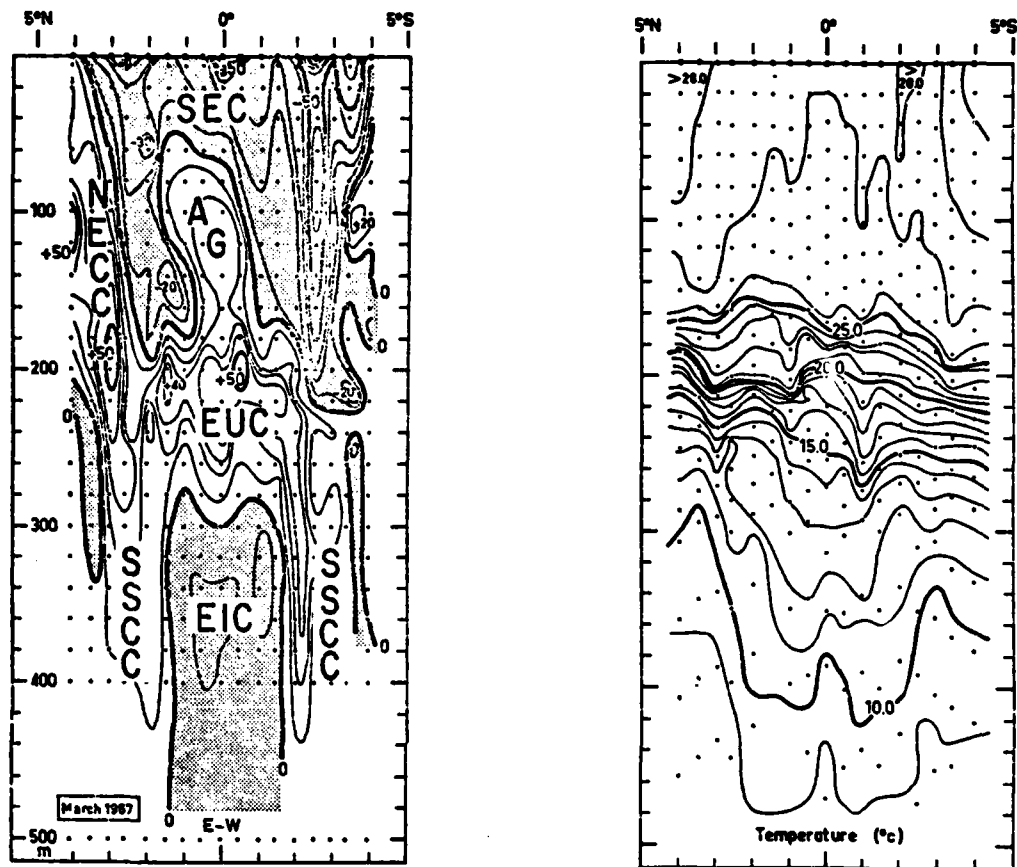


Figure 1. (a) Meridional section of zonal velocity at 170°E. Labelled currents are South Equatorial Current (SEC), Equatorial Undercurrent (EUC), Equatorial Intermediate Current (EIC), North Equatorial Counter-current (NECC) and subsurface countercurrents (SSCC). The current labelled AG is an ageostrophic flow. Regions of westward flow are stippled. (b) Corresponding meridional section of temperature. (after Hisard, *et al.*, 1970).

lies between the SEC and EUC is peculiar to those regions which have a deep mixed layer. It is neither permanent nor in geostrophic balance (Hisard *et al.*, 1970).

The source of momentum for the EUC is an eastward pressure gradient force set up by the Trade Winds. With only weak deflecting forces near the equator, water simply flows eastward down this pressure gradient below the action of the wind stress. Using hydrographic data, Knauss (1966) in the Pacific and Katz *et al.* (1977) in the Atlantic have measured this force to be about 5×10^{-5} dyne cm^{-3} at the surface falling to half that value at the depth of the EUC core. The signal is eventually swamped by noise at greater depths.

Cromwell (1953) and later Fofonoff and Montgomery (1955) suggested a meridional circulation associated with flow patterns like those of Figure 1. Upwelling, as inferred from doming isotherms and nutrient concentrations near the equator, feeds a surface meridional Ekman divergence. This upwelling and a downwelling inferred from downward trending isotherms below the core of the EUC requires meridional convergence of mass in the thermocline. The convergence is geostrophically balanced by the same pressure gradient that drives the EUC. Knauss (1966) has measured meridional velocities at 150°W of $0(1-10 \text{ cm sec}^{-1})$ and by scaling arguments deduces vertical velocities of $0(1-5 \times 10^{-3} \text{ cm sec}^{-1})$.

The Indian Ocean is dominated by seasonal monsoons and mean zonal westerly winds rather than steady easterlies. Consequently only during the Northeast Monsoon will the circulation resemble the persistent

Pacific and Atlantic patterns. More comprehensive surveys of these flow features in all equatorial oceans can be found in Knauss (1963); Philander (1973b); Leetmaa, McCreary and Moore (1980); Tsuchiya (1975); Cochrane *et al.* (1979) and Taft *et al.* (1974).

The recent observations of Luyten and Swallow (1976) in the Indian Ocean and Luyten and Eriksen (1980) in the western Pacific add a new dimension to investigations of the equatorial circulation. They measured several zonal currents trapped to the equator down to 4000 meters. The data fail to resolve the time scales of these stacked jets, but they must be at least several months. Furthermore it is not clear how or if they are related to the winds or shallower currents. It is evident though that the short vertical wavelengths of O(100's of meters) imply a much higher degree of baroclinicity than at mid-latitudes.

B. Previous Theories

In this section I will discuss the development of key dynamical concepts deduced from previous theories. I will not attempt a comprehensive review since there are several published surveys of equatorial models, notably Philander (1973b), Gill (1975), Moore and Philander (1977) and Leetmaa, McCreary and Moore (1980). I will furthermore restrict discussion to those models in the oceanic parameter range rather than those more appropriate to laboratory studies, though the latter can contribute to our understanding of oceanic processes.

The primary intent of nearly all steady state equatorial models has been to provide a dynamical description of the EUC since this was the first subsurface flow discovered and since it is typically the strongest of all equatorial currents. One feature common to all these models is

that they are formulated on the equatorial beta-plane i.e. the Coriolis parameter is everywhere equal to a constant times latitude. This implies that the equatorial zone is a singular region of the global circulation because rotational forces cannot dominate the flow there. Robinson (1960) points out that close to the equator, a number of processes can compensate for the diminished Coriolis forces. A model that includes at least some of these may give a reasonably good approximation of the flow patterns and scales. Accordingly a great many models which cover a wide range of parameter space have been proposed. It is instructive to distinguish between those that assume constant density and those that include continuous vertical density stratification.

1. Constant Density Models

Because the EUC is a near surface feature, the depth of the ocean in constant density models is taken to be the depth of a deep mixed layer like that in the western Pacific. The assumption is that a sharp thermocline at the base of the mixed layer completely inhibits communication with the deeper ocean. This is not entirely justifiable (e.g. Knox, 1976) but it typically leads to a set of mathematically tractable equations. The models of Stommel (1960) and Charney (1960) exemplify and illustrate the limitations of this type of formulation. In these, the depth integrated pressure gradient is in balance with an easterly wind stress. Via the hydrostatic relation this approximates the observed rise in sea level to the west in both the Atlantic and Pacific Oceans. Other zonal variations are assumed small compared to meridional variations so that flow can be examined solely on the meridional plane.

In Stommel's linear calculation the pressure gradient is able to

drive an eastward flow below a westward wind drift near the equator (Figure 2a). However the scales are critically dependent on the magnitude of a vertical eddy viscosity. In fact it is not possible to adjust this parameter to give realistic width and velocity scales simultaneously. Furthermore, Stommel chose a no stress rather than no slip condition at the bottom of his model ocean. Charney used the latter condition in a linear calculation and found no eastward flow near the equator in the presence of easterly winds.

The EUC in Charney's model depends on nonlinearity (Figure 2b). Westward momentum fed in through the surface by the winds is carried poleward resulting in a net gain of eastward momentum near the equator. Such a tendency is predicted by the calculation of quadratic corrections to the linear model (Robinson, 1966). This gain of eastward momentum is also consistent with the tendency to conserve absolute vorticity near the equator in the presence of an eastward pressure force (Fofonoff and Montgomery, 1955; Cane, 1979). A particle as it approaches the equator loses planetary vorticity which must be compensated for by a gain of relative vorticity. The sign of this gain is such that the current accelerates eastward. However if the friction coefficient is too small in Charney's model ($< 14 \text{ cm}^2 \text{ sec}^{-1}$), solutions become unstable.

The meridional circulation in these models is similar to that deduced from observations. In particular, for westward winds there is upwelling near the equator and surface divergence while at depth there is a convergence of mass. The distribution of temperature is not predicted since the entire layer is of a single density.

While these models shed light onto the dynamics of an equatorial fluid, they have some serious drawbacks. Already mentioned are their

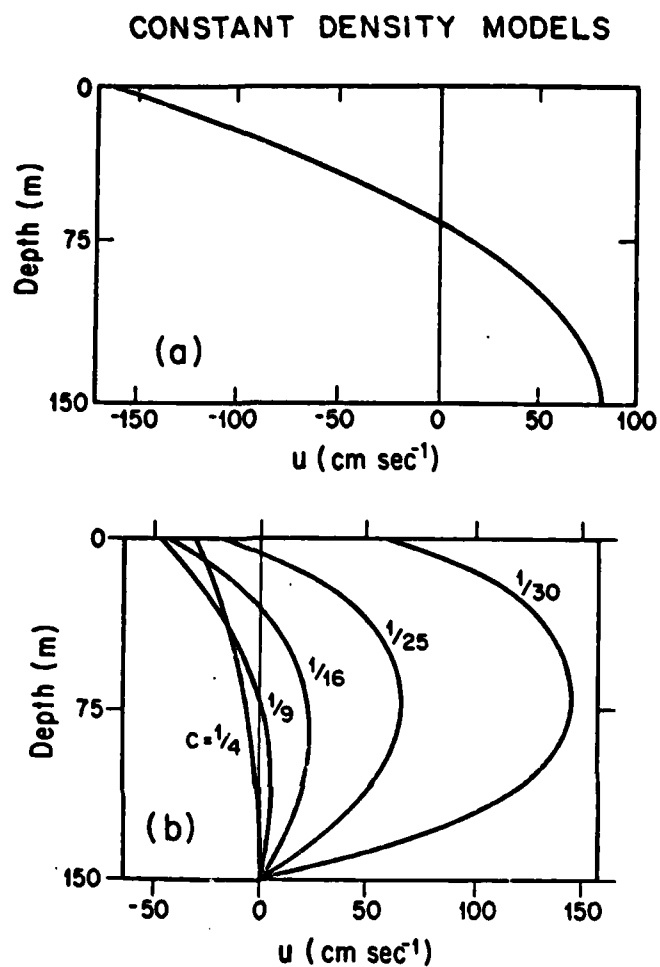


Figure 2. Profiles of zonal velocity at the equator computed from the constant density models of (a) Stommel (1960) and (b) Charney (1960). Decreasing values of c in the Charney calculation imply stronger nonlinearity. Negative velocities are to the west.

sensitivity to the size of eddy coefficients and type of bottom boundary conditions as well as an inability to predict the temperature field. The lack of longitudinal variation is not reasonable. For example, zonal variability is present in the winds (Wyrski and Meyers, 1975; Hellerman, 1967), surface temperature (Colin *et al.*, 1971), current speeds, transports and depth of the EUC (Knauss, 1960). Knauss (1966) computes significant downstream advection of zonal momentum in the EUC. Moreover these models tell us nothing of the deeper EIC and SSCC. Their crucial limitation though is that they place the EUC in the mixed layer, not in the thermocline where it is observed. Shear profiles in a constant density ocean cannot be in geostrophic balance whereas measurements show that all the permanent zonal equatorial flows are. As such these models are at best applicable to ageostrophic flow like that observed at the base of the deep mixed layer in the western Pacific (Figure 1). To understand flow in the thermocline, clearly we require a theory that includes continuous stratification.

2. Stratified Models

Even before the discovery of the EUC, Sverdrup (1947) proposed a theory of the steady circulation in a stratified equatorial ocean. He derived relationships between various depth-integrated flow quantities and surface wind stress. While such a theory can provide no details of baroclinic structure, Arthur (1960) showed that Sverdrup's calculations were consistent with the notion of an eastward subsurface flow imbedded in a westward surface wind drift. Yoshida (1959) was the first to explicitly model the EUC in the thermocline. Working with a linearized system of equations, he deduced a geostrophic balance for the zonal flows

as well as the dependence of certain scales, e.g. width and velocity, on stratification. However his results require a large number of *a priori* assumptions for computational expedience. For instance, he neglects the vertical diffusion of meridional momentum thus filtering out Ekman layers. Veronis (1960) attempted a nonlinear calculation on a zonal plane along the equator by using perturbation expansions in latitude. Though in some respects temperature and zonal velocity resembled observed fields, the system of equations could not be closed. The perturbation expansions generated more unknowns than physical constraints.

Pedlosky (1969) discussed axisymmetric flow of a linear stratified fluid between two concentric spheres in a parameter range appropriate to the ocean. For an imposed surface heat flux and velocity, geostrophic flow penetrated all the way to the bottom of the equatorial ocean whereas Ekman currents disappeared. Because the model did not include zonal dependence and specifically zonal pressure gradients, no EUC-like features developed. On the other hand he derived an expression

$$S = \frac{g\alpha_z D^2}{f^2 L^2} \quad (1)$$

which measures the relative importance of stratification versus rotation. For flow with a given length scale L and depth scale D in a thermally stratified ocean of Väisälä frequency $(g\alpha_z)^{1/2}$, rotation (f) will dominate when the S is small. Clearly in the equatorial boundary layer where $f \rightarrow 0$, stratification takes on a greater significance than elsewhere. The equatorial Rossby radius i.e. the width of the equatorial boundary layer can be defined as that point in latitude $y=L$ where S is 1.

Philander (1973a,b) solved a fully nonlinear set of momentum and heat equations for the equatorial ocean. Though there were no eastern or western boundaries, a zonal pressure gradient was generated by imposing an eastward sea surface temperature gradient like that observed in Pacific (Colin *et al.*, 1971). He removed the zonal dependence by a similarity transform, then solved for the resulting two dimensional flow by numerical integration. Results showed spreading isotherms in the vicinity of a subsurface geostrophic EUC that flowed below a westward surface wind drift and above a westward EIC. Inertial terms were important at nearly all depths on the equator and the primary dissipative mechanism was horizontal friction. McCreary's (1980) analysis showed a similar vertical current structure. In addition, flanking the deep westward flow and contiguous to the EUC were weak tongues of eastward momentum reminiscent of the SSCC. Unlike Philander's model, these calculations were performed on a strictly linear set of equations that included vertically diffusive terms as the only sinks.

Stratified models can produce geostrophic zonal currents with realistic shear as well as appropriate width, depth and velocity scales in the equatorial boundary layer. A comparison of the Pedlosky, Philander and McCreary models indicates that a baroclinic eastward pressure force is necessary to drive the EUC. By allowing zonal variations, this pressure force can be established even in an unbounded ocean: McCreary generates it with a zonally confined wind stress, Philander by imposing a longitudinal surface temperature. McCreary's model would further suggest that nonlinear forces can be neglected as a first approximation.

Through these efforts we have discovered some important physics of the equatorial flow regime, but many questions remain. We need to know more about turbulent processes and how to parameterize them in large scale circulation models. To dramatize this point, Philander's (1973a,b) similarity solutions predicted an eastward decrease in width, depth and velocity of the EUC. This may be a consequence of his choice of vertical eddy coefficients that decrease eastward since his scaling arguments indicate that width, depth and velocity decrease with decreasing vertical eddy viscosity. Because Wyrski and Bennett (1963) argue that turbulent dissipation increases west to east in the Pacific, it is not clear how robust the predicted downstream variations would be given a more realistic parameterization of diffusive processes. Likewise, to obtain easily solved equations, McCreary must assume an eddy viscosity that is inversely proportional to the Väisälä frequency. There is some physical basis for this parameterization (Turner, 1973, p. 143), but other forms must be tested to gain confidence in the persistence of key flow properties.

The transition from mid-latitude to equatorial dynamics has previously been studied using matched asymptotic expansions (Philander, 1971; Pedlosky, 1969; Philander, 1973a,b). This is a relatively complicated technique that can sometimes obscure the continuity of certain flow features from one region to the next. In contrast, Schneider and Lindzen (1976) examine thermally driven axisymmetric atmospheric circulation over a sphere using a method that is uniformly valid at all latitudes. Their approach revealed the importance of baroclinic pressure gradients in maintaining well behaved Ekman layers within the atmospheric equatorial boundary layer. A uniformly valid representation for non-axisymmetric

wind-driven flow typical of the ocean would certainly be valuable.

In the following sections I develop two analytically tractable models of the steady ocean circulation on a stratified equatorial beta-plane. Both are linear and vertically diffusive like McCreary's model, but one dissipates heat by a Newtonian cooling approximation and the other has biharmonic friction. This work can also be viewed as a generalization of the Stommel and Veronis (1957) mid-latitude theory to include the equatorial ocean. In that study, Ekman and geostrophic motions were clearly separated into distinct vertical boundary layers. The specific questions I will address are 1) how are Ekman and geostrophic dynamics transformed as the equator is approached and 2) which features of the linearized model persist for different turbulence parameterizations. In answering these questions I will give special attention to the role of stratification and baroclinic pressure gradients.

C. Newtonian Cooling Model

Section C is devoted to the study of a steady state model in which wind forced temperature fluctuations dissipate via Newtonian cooling. The model equations are developed in Section C1 (Formulation) and solved for a test case in Section C2 (Zonal Winds). Section C3 (Variation of Parameters) explores the manner in which results depend on eddy viscosity, stratification, etc. I then examine results for meridional wind forcing (Section C4) and conclude with a brief summary and discussion (Section C5).

1. Formulation

Consider a reference atmospheric state of steady, horizontally

uniform downward heat flux at the ocean surface. In an ocean with horizontally uniform thermal conductivity, this flux will generate a background vertical temperature gradient $\bar{\theta}_z$ that is a function of depth only. It is hypothesized that deviations from this atmospheric state excite perturbations (u,v,w,p,θ) around the background temperature field according to the linearized set of equations

$$-\beta y v + \frac{1}{\rho_0} p_x = (A u_z)_z \quad (2a)$$

$$\beta y u + \frac{1}{\rho_0} p_y = (A v_z)_z \quad (2b)$$

$$p_z = \rho_0 g \alpha \theta \quad (2c)$$

$$u_x + v_y + w_z = 0 \quad (2d)$$

$$w \bar{\theta}_z = (K \theta_z)_z \quad (2e)$$

The coordinate system is right-handed and subscripts (x,y,z) denote differentiation with respect to (latitude, longitude, depth). I have made the standard equatorial β -plane approximation, viz. $f=\beta y$. The ocean is hydrostatic (2c) and density has been derived from an equation of state linearized about temperature. Eddy viscosity and heat diffusivity are A and K respectively, and will be assumed constant unless otherwise stated. Other notation in (2) is defined in the list of symbols (p. vi).

Terms involving $\bar{u}, \bar{v}, \bar{w}$, do not appear in (2). If the background flow is assumed geostrophic and negligible at some great depth, then

$(\bar{u}, \bar{v}) \sim 0$. Moreover, from the resulting vertical advective-diffusive temperature balance, $\bar{w} \sim O(\frac{K}{D_T})$ where D_T is the depth scale of the background thermal field. Terms containing \bar{w} are thus small compared to those in (2e) provided that D_T is large and/or K is small. For the special case of $D_T = \infty$ (i.e. $\bar{\theta}_{zz} \equiv 0$), \bar{w} is identically zero. Thus the oceanic background state couples to the perturbation field only through the term $w\bar{\theta}_z$.

Stommel and Veronis (1957) examined (2) on the mid-latitude f and β -planes. The extension of their work to the equatorial β -plane is not straightforward because for realistic boundary conditions, the equations will not separate in y - z (Schneider and Lindzen, 1976). I thus change the form of (2e) by making a Newtonian cooling assumption in this section

$$w\bar{\theta}_z = -\frac{K}{D^2} \theta \quad (2e')$$

where diffusion of temperature anomalies is replaced by a relaxation to the equilibrium value of $\bar{\theta}$. The quantity D is a depth scale.

I consider only the case of a zonally unbounded ocean in which the perturbation fields are subject to the conditions

$$\rho_0 A u_z = \tau^{(x)}, \quad \rho_0 A v_z = \tau^{(y)}, \quad w = 0 \text{ @ } z = 0 \quad (3a)$$

$$u = v = w = 0 \quad \text{@ } z = -H \quad (3b)$$

$$u, v, w, p, \theta \rightarrow 0 \quad \text{as } |y| \rightarrow \infty \quad (3c)$$

The depth of the ocean H is taken to be 4000m. Note that there are now no temperature boundary conditions because temperature follows vertical velocity ($2e'$).

To produce a set of scaled equations in which all terms are $O(1)$, define the nondimensional (primed) variables

$$\begin{aligned} (x,y) &= (x',y')L, \quad L = \left(\frac{A^2 g \alpha \bar{\theta}_z}{\beta^3 K} \right)^{1/5} \\ z &= z'D, \quad D = \left(\frac{A}{\beta L} \right)^{1/2} = \left(\frac{A^3 K}{\beta^2 g \alpha \bar{\theta}_z} \right)^{1/10} \\ (u,v,w) &= u(u',v',\frac{D}{L} w'), \quad u = \frac{D}{\rho_0 A} \tau_0 \\ p &= p' p', \quad p' = \frac{L}{D} \tau_0 \\ \theta &= T \theta', \quad T = \frac{L}{\rho_0 g \alpha D^2} \tau_0 \\ \tau &= \tau_0 \tau' \end{aligned} \tag{4}$$

The quantity L is a baroclinic Rossby radius based on the depth scale $D = \left(\frac{A}{\beta L} \right)^{1/2}$ which is the Ekman layer depth at $y=L$. It can be derived from (1) by setting that ratio to unity and $A=K$, $f=\beta L$. Substituting (4) into (2) and dropping primes

$$-yv + p_x = u_{zz} \tag{5a}$$

$$yu + p_y = v_{zz} \tag{5b}$$

$$u_x + v_y + w_z = 0 \quad (5c)$$

$$p_z = 0 \quad (5d)$$

$$w = -\theta \quad (5e)$$

The boundary conditions are

$$u_z = \tau(x), \quad v_z = \tau(y), \quad w = 0 \quad @ \quad z = 0 \quad (6a)$$

$$u = v = w = 0 \quad @ \quad z = -H \quad (6b)$$

$$u, v, w, p, \theta \rightarrow 0 \quad \text{as } |y| \rightarrow \infty \quad (6c)$$

where H is now nondimensional ocean depth.

From (5), a single expression for v is available which is sixth order in the vertical derivative

$$v_{(6z)} + v_x - v_{xxzz} - [v_{yy} - y^2 v]_{zz} = 0 \quad (7)$$

and which has separable solutions of the form

$$v(x, y, z) = \int_{-\infty}^{\infty} \sum_{n=0}^{\infty} \hat{v}_n(\ell, y, z) e^{i\ell x} d\ell \quad (8)$$

$$\hat{v}_n = \sum_{j=1}^6 a_{n,j}(\ell) e^{m_{n,j}(\ell)z} \psi_n(y)$$

The zonal dependence is $e^{i\ell x}$ because the ocean is longitudinally unbounded. Imposition of boundary conditions in the zonal direction leads to a nonseparable partial differential equation in x - z .

The Hermite functions ψ_n are a complete orthonormal set in latitude governed by

$$(\psi_n)_{yy} - y^2 \psi_n = - (2n+1) \psi_n \quad (9a)$$

$$\psi_n = (2^n n! \pi^{1/2})^{-1/2} H_n(y) e^{-y^2/2} \quad (9b)$$

$$H_n(y) = (-1)^n e^{y^2} \frac{d^n}{dy^n} e^{-y^2}$$

They are symmetric (antisymmetric) about $y=0$ for even (odd) n and decay (oscillate) poleward (equatorward) of a turning latitude defined from (9a) as

$$y = y_t = \pm (2n+1)^{1/2} \quad (10)$$

These are the same functions that describe the meridional dependence of equatorial β -plane waves (Moore and Philander, 1977). The depth dependence $\phi = e^{mz}$ obeys

$$\phi(6z) + (2n+1+\ell^2) \phi_{zz} + i\ell\phi = 0 \quad (11)$$

provided that

$$m^6 + (2n+1+\ell^2)m^2 + i\ell = 0 \quad (12)$$

is satisfied for all $n \geq 0$. The subscripts j in (8) refers to one of the six roots of (12). This relation (12) is similar to the dispersion of equatorial waves and will therefore be referred to as a dispersion relation. Further discussion of the wave analogy follows (21).

From (5), (8) and the recursion formulae

$$(\psi_n)_y = - \left(\frac{n+1}{2}\right)^{\frac{1}{2}} \psi_{n+1} + \left(\frac{n}{2}\right)^{\frac{1}{2}} \psi_{n-1} \quad (13a)$$

$$y\psi_n = \left(\frac{n+1}{2}\right)^{\frac{1}{2}} \psi_{n+1} + \left(\frac{n}{2}\right)^{\frac{1}{2}} \psi_{n-1} \quad (13b)$$

$$\psi_{-1} \equiv 0 \quad (13c)$$

one finds

$$\begin{pmatrix} \hat{u}_n \\ \hat{w}_n \\ \hat{p}_n \\ \hat{\theta}_n \end{pmatrix} = \sum_{j=1}^6 a_{n,j} \begin{pmatrix} -1 \\ m_{n,j} \\ -1 \\ -m_{n,j} \end{pmatrix} (m_{n,j}^2 - i\ell)^{-1} \left(\frac{n+1}{2}\right)^{\frac{1}{2}} \psi_{n+1} \\ + \begin{pmatrix} -1 \\ -m_{n,j} \\ 1 \\ m_{n,j} \end{pmatrix} (m_{n,j}^2 + i\ell)^{-1} \left(\frac{n}{2}\right)^{\frac{1}{2}} \psi_{n-1} \Bigg] e^{m_{n,j}z} \quad (14)$$

For $n \geq 0$ all the fields (8) and (14) decay exponentially at high latitudes except for two growing components of \hat{u}_0 that are specified by $m^2 = -12$. For these two roots m , $a_{0,j} \equiv 0$ necessarily and the dispersion reduces to

$$m^4 - i\ell m^2 + 1 = 0 \quad (15)$$

There is a solution to (5) not contained in (7), viz. for $v \equiv 0$

$$p_x = u_{zz} \quad (16a)$$

$$yu + p_y = 0 \quad (16b)$$

$$u_x + w_z = 0 \quad (16c)$$

$$p_z = \theta \quad (16d)$$

$$w = -\theta \quad (16e)$$

Expressions analogous to (14) are

$$\begin{pmatrix} \hat{u}_{-1} \\ \hat{w}_{-1} \\ \hat{p}_{-1} \\ \hat{\theta}_{-1} \end{pmatrix} = \sum_{j=1}^2 a_{-1,j} \begin{pmatrix} 1 \\ -m_{-1,j} \\ 1 \\ m_{-1,j} \end{pmatrix} \psi_0(y) \quad (17)$$

with dispersion

$$m^2 = i\ell \quad (18)$$

This is the gravest mode in \hat{u} and is designated $n=-1$ since for that value (12) reduces to (18). It is interesting to note that (18) is the dispersion for a non-rotating ocean (i.e. for $f = \beta = 0$).

In the special case $\ell=0$, parts of (8), (14) and (17) that correspond to $m=0$ must be replaced by

$$v_n \equiv 0$$

$$\begin{pmatrix} \hat{u}_n \\ \hat{w}_n \\ \hat{p}_n \\ \hat{\theta}_n \end{pmatrix} = \sum_{n=0}^{\infty} \begin{pmatrix} a_{n,1}z + a_{n,2} \\ -c_{n,1} \\ c_{n,1}z + c_{n,2} \\ c_{n,1} \end{pmatrix} \quad (19)$$

where a_n and c_n can be related through the meridional geostrophic balance (5b).

The total solution to (5) is now

$$q = \int_{-\infty}^{\infty} [\hat{q}_{-1} + \sum_{n=0}^{\infty} q_n] e^{i\ell x} d\ell \quad (20)$$

where q is any one of u, v , etc and where $\hat{v}_{-1} \equiv 0$. Provided that $\ell \neq 0$, depth integrated quantities

$$Q = \int_{z_2}^{z_1} q \, dz \quad (21)$$

follow readily from (20) by substituting $a_{n,j} \rightarrow a_{n,j}/m_{n,j}$ and subtracting the series evaluated at z_2 from that at z_1 . Depth-integrated quantities will be discussed in Section C2c.

There is a useful analogy between the present steady state frictional model and time dependent inviscid wave theory. If w and θ are eliminated from (5) and the time derivative $\frac{\partial}{\partial t}$ replaces $-(\frac{\partial}{\partial z})^2$, the resulting equations are formally identical to those that govern baroclinic equatorial waves (e.g. Moore and Philander, 1977). This identity is also evident in Figure 3 which is a dispersion plot of $\text{Im } (m^2)$ vs. ℓ from (12). In wave theory the ordinate is frequency rather than vertical wavenumber squared. Though steady and viscous, the two families of curves ($n=1,2,3\dots$) designated Ekman and geostrophic are analogous to inertio-gravity and quasi-geostrophic Rossby waves whereas the $n=0$ is a hybrid equivalent of the mixed Rossby-gravity wave. The Ekman roots at large vertical wavenumber will be strongly surface trapped relative to the low vertical wavenumber geostrophic modes. There is also a viscous Kelvin mode ($n=-1$) corresponding to the Kelvin wave.

In addition to the wave analogy, the connection with mid-latitude steady state theories can be seen by taking the limit $\ell \rightarrow 0$ in (12):

$$m^4 = - (2n+1) \quad (22a)$$

$$m^2 = - i\ell/(2n+1) \quad (22b)$$

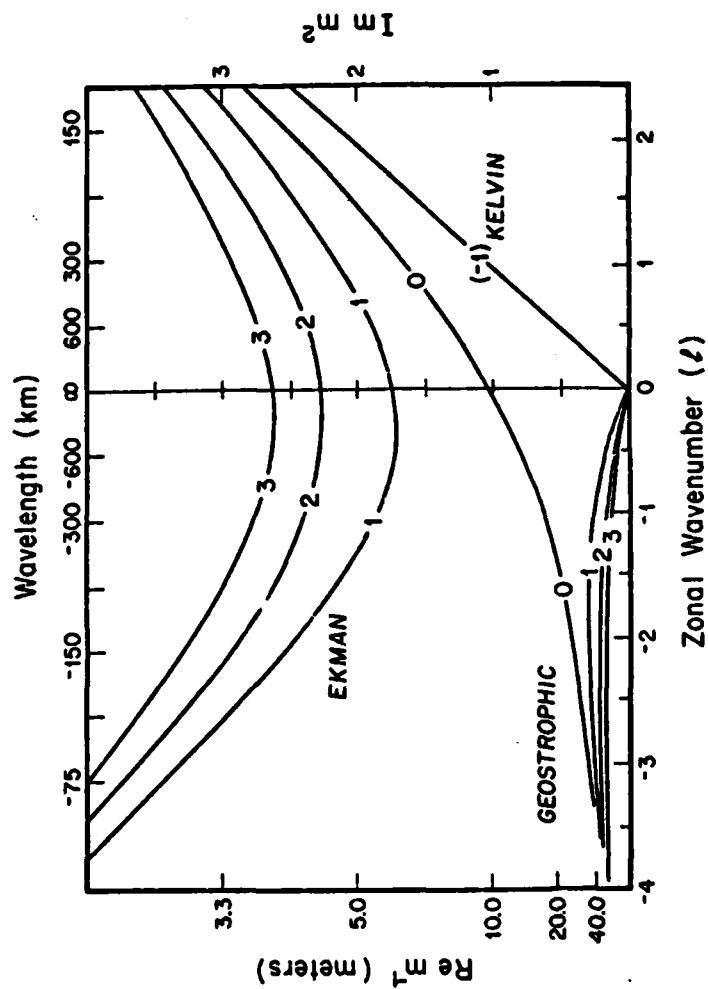


Figure 3. A plot of $\text{Im}(m^2)$ vs. l from the dispersion relation (12) for $n=-1,0,1,2,3$. Dimensional values of wavelength ($=2\pi\lambda^{-1}$) and vertical trapping scale $\text{Re } m^{-1}$ are computed for $A=K=1 \text{ cm}^2 \text{ sec}^{-1}$, $\bar{\theta}_z=10^{-4} \text{ }^\circ\text{C cm}^{-1}$.

Substituting the expression for turning latitude (10) into these results in

$$m^4 = -y_t^2 \quad (23a)$$

$$m^2 = -i\ell/y_t^2 \quad (23b)$$

which is the dispersion for Ekman (23a) and geostrophic (23b) dynamics on a mid-latitude β -plane centered at $y = y_t$ (see Section C2c). An interesting feature of the equatorial *vis a vis* mid-latitude β -plane Ekman roots is that the Ekman depth $D_e = \text{Re } m^{-1}$ calculated from the former is not singular at the equator. The Kelvin mode is unique in that it has no mid-latitude counterpart, though it may be considered an extension of the geostrophic roots to $n = -1$ in the limit $\ell \rightarrow 0$.

2. Zonal Winds

a. Method of Solution

We obtain solutions by determining the unknown amplitudes $a_{n,j}$ in (8), (14) and (17). Series expansions for the boundary conditions are truncated at some $n=N < \infty$ and values of u_z, v_z, w at $z=0$ and u, v, w at the ocean bottom are projected onto them. For zonal winds characterized by a single Fourier component

$$\tau = e^{i\ell_0 x} \hat{\tau}(y) \quad (24)$$

we obtain a matrix equation of the form

$$\begin{pmatrix} \vec{A} \\ \vec{C} \end{pmatrix} = \vec{B} \quad (25)$$

where \vec{A} is the vector $\{a_{n,j}\}$, $\vec{B} = \{b_n\}$ is the vector projection of $\hat{\tau}(y)$ onto $\psi_n(y)$ defined by

$$\hat{\tau}(y) = \sum_{n=0}^N b_n \psi_n(y) ; \quad b_n = \int_{-\infty}^{\infty} \hat{\tau}(y) \psi_n(y) dy \quad (26)$$

and \vec{C} is a banded matrix of coefficients. Provided the dimension of \vec{C} is 0(100) or less, (25) can be solved efficiently using standard matrix inversion techniques.

We will examine solutions to (5) for the depth invariant quantities $A=K=1 \text{ cm}^2 \text{ sec}^{-1}$ and $\bar{\theta}_z = 10^{-4} \text{ }^\circ\text{C cm}^{-1}$ such that scales in (4) become $D=10\text{m}$, $L=46\text{km}$, $U=97\text{cm sec}^{-1}$, $W=0.21\text{cm sec}^{-1}$, $P=4.7 \times 10^2 \text{ dyne cm}^{-2}$, $T=2.0^\circ\text{C}$. Zonal wavelengths and vertical trapping scales (Re m^{-1}) then have the dimensional values shown in Figure 3. Winds will be of the form

$$\tau = \tau^{(x)}(x,y) = \tau_0 e^{i\ell_0 x} e^{-\gamma y^2} \quad (27)$$

where $\gamma = 2 \times 10^{-3}$ corresponds to an e-folding distance of 10° latitude and $\tau_0 = 0.1 \text{ dyne cm}^{-2}$. The value $\ell_0 = 1.4 \times 10^{-2}$ corresponds to a 20000km zonal wavelength which approximates some of the largest Trade Wind scales. A plot of $\tau^{(x)}$ is shown in Figure 4. Because this wind is symmetric in latitude, u, w, p, θ will also be even and v will be odd. The vector \vec{B} readily evaluated from (26) is

$$b_0 = \left[\frac{\pi^{1/2}}{(\gamma + \ell_0^2)} \right]^{1/2} \quad (28a)$$

WIND STRESS

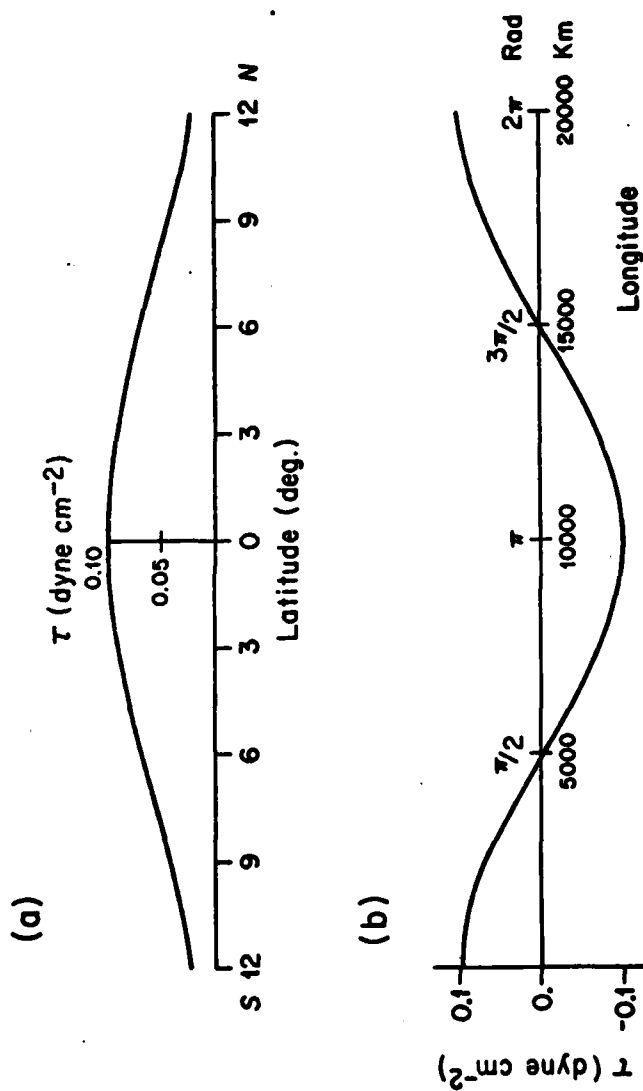


Figure 4. (a) Meridional and (b) longitudinal variations of zonal wind stress. Only one cycle in longitude is shown.

$$b_n = \left(\frac{1-2\gamma}{1+2\gamma} \right) \left(\frac{n-1}{n} \right)^{\frac{1}{2}} b_{n-2}, \quad n \text{ even} \quad (28b)$$

$$b_n = 0, \quad n \text{ odd} \quad (28c)$$

A small wind stress curl ($\gamma \neq 0$) speeds up convergence of the sequence therefore minimizing the dimension of $\frac{\pm}{C}$.

A trial calculation indicates that bottom trapped modes ($\text{Re } m < 0$) are uniformly three orders of magnitude weaker than surface trapped modes for the winds (27) and they are hereafter ignored. Series expansions for the dependent variables converge fastest near the equator and slowest for the vertical velocity. The truncation index is $N=77$ and allows determination of all fields to within $O(1\%)$. Unless otherwise specified, flow variables have been calculated at the longitude of maximum westward winds ($x=\pi$ in Figure 4).

b. Flow Description

Figure 5 shows depth profiles of various fields on the equator. Salient features include an eastward EUC ($u_{\text{max}} \sim 120 \text{ cm sec}^{-1}$) centered near 220m below a surface westward wind drift, a baroclinic zonal pressure force which is eastward at the EUC velocity core and upwelling (downwelling) above (below and in) this core correlated with anomalously cold (warm) water. A westward EIC below the EUC appears weak ($\sim 5 \text{ cm sec}^{-1}$) when plotted on the scale of the surface current. The latter is too strong because exact solution does not permit a depth variable mixing coefficient which can increase near the surface in agreement with the observations of Jones (1973) and Crawford (1976). (See however Section C3c). The pressure gradient reversal near 350m has never been observed but Arthur (1960)

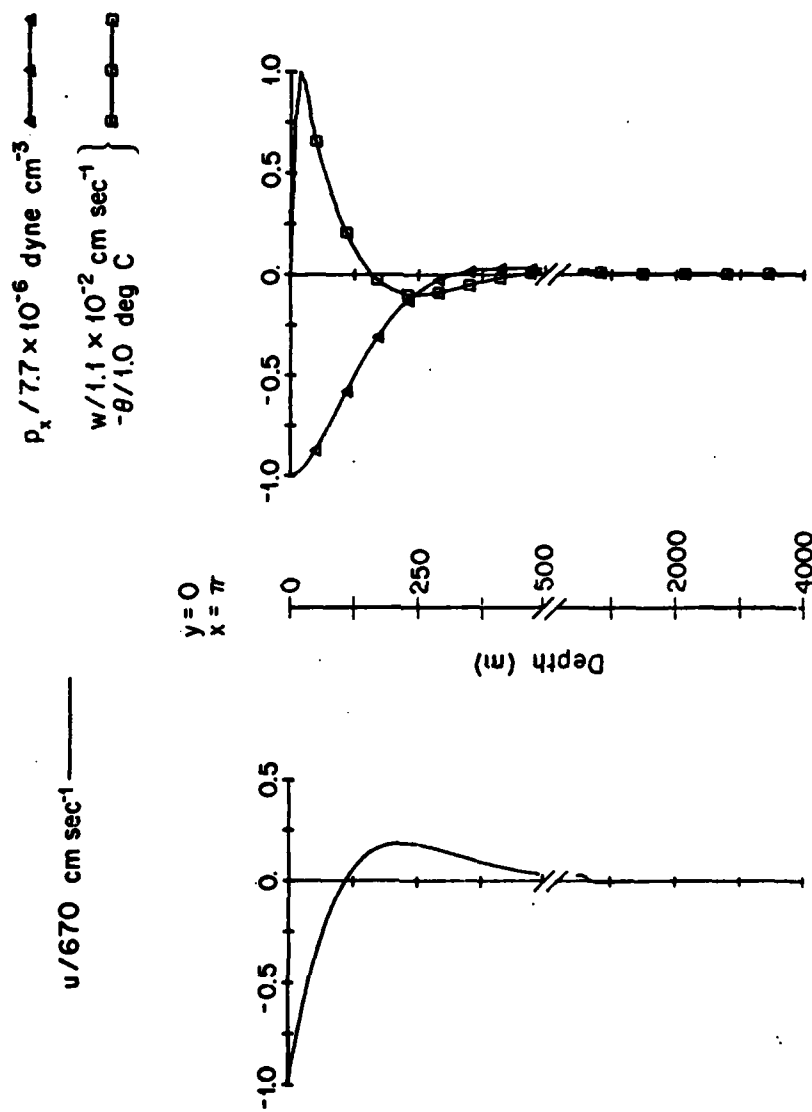


Figure 5. Depth profiles of perturbation variables on the equator. Quantities have been scaled by values to their right for plotting on the interval $(-1.0, 1.0)$.

deduced it by showing that the EUC velocity could not vanish at depth otherwise.

These profiles should be compared to the flow at $y=3.5$, poleward of the equatorial boundary layer. In Figure 6 one sees a shallow surface Ekman spiral and a net meridional transport in the upper 40m. Surface velocity is $\sim 55^\circ$ rather than 45° to the right of the wind because of the importance of a geostrophic component of zonal velocity. The deep baroclinic geostrophic flow is less strongly surface trapped than at the equator and overall velocities are weaker.

Figure 7a is a meridional section of zonal velocity down to 500m. Only flow from $0 \leq y \leq 4$ is shown since the field is symmetric about the equator. The meridional extent of the equatorial boundary layer is $O(1 \text{ Rossby radius})$ or about 75km which is narrower than the observed half width of the EUC by a factor of 2. Figure 7b shows the meridional circulation on the same plane. Upwelled water above the Undercurrent is carried poleward in a surface Ekman layer. Water downwelled from the Ekman layer drifts slowly equatorward at depth in geostrophic response to the eastward pressure force. This mass convergence near the equator contributes to both upwelling and downwelling in the vicinity of the EUC. Such a flow pattern is similar to that discussed by Cromwell (1953) and Fofonoff and Montgomery (1955), but because meridional velocities are significantly weaker than zonal velocities (especially below the Ekman layer) we might expect zonal variations to play an important role in the mass and momentum balances. Figure 8, which is a zonal section down to 500m of zonal velocity over one wavelength of the wind, supports this view. At the surface, $u \neq 0$ when $\tau^{(x)} = 0$ implying that nonlocal

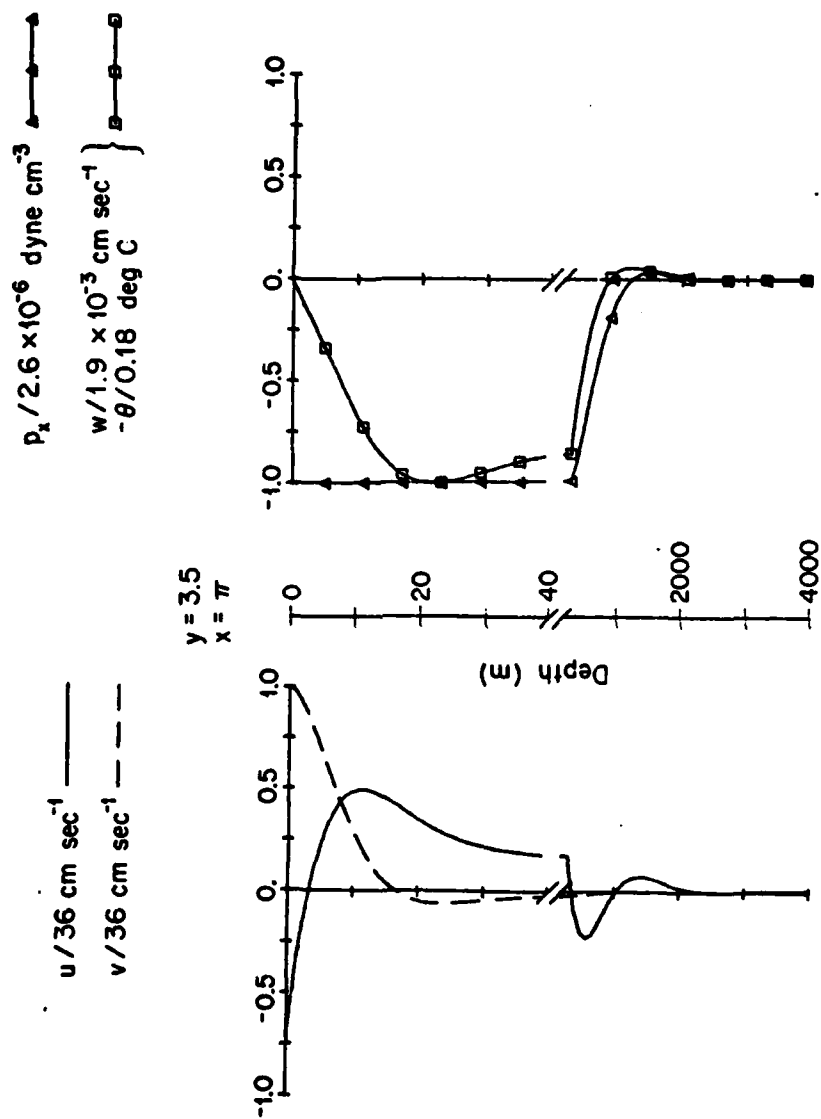


Figure 6. Depth profiles of perturbation variables outside the equatorial boundary layer.

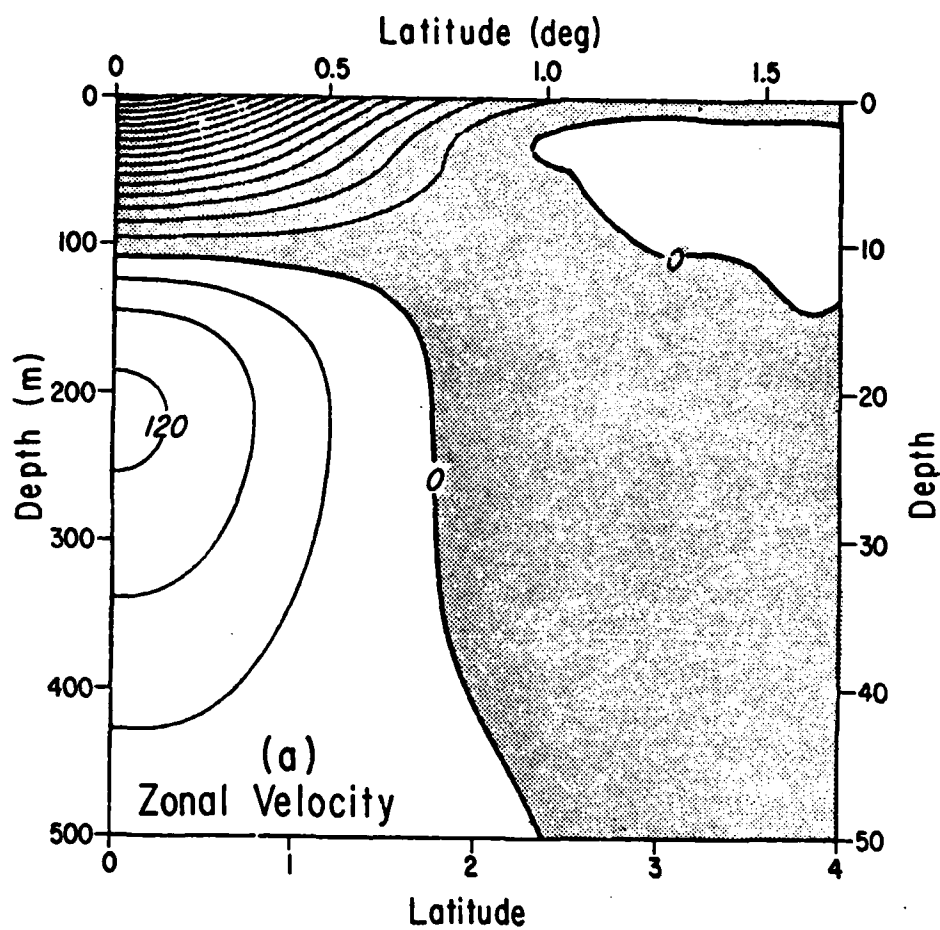


Figure 7a. Meridional section of zonal velocity. Contour interval is 40 cm sec^{-1} ; regions of westward flow are stippled.

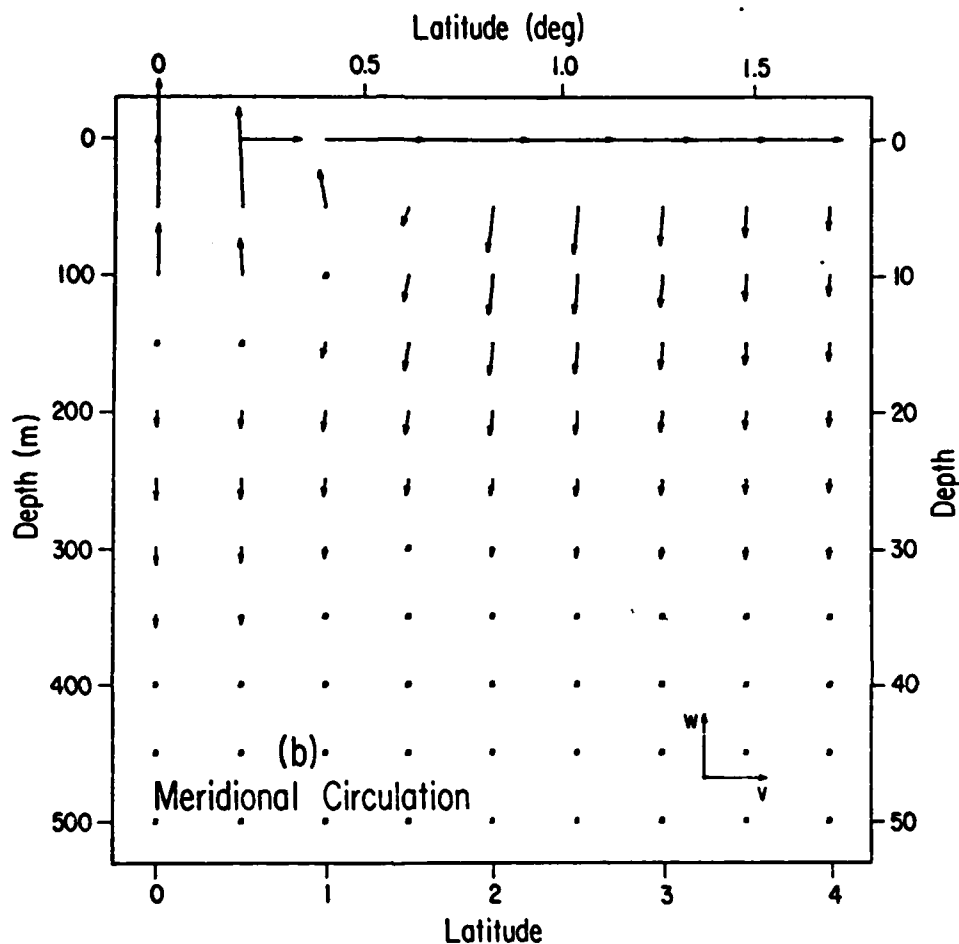


Figure 7b. Meridional circulation corresponding to the zonal velocity section shown in Figure 7a. Scales for v and w shown at lower right are 25 cm sec^{-1} and $4 \times 10^{-3} \text{ cm sec}^{-1}$ respectively.

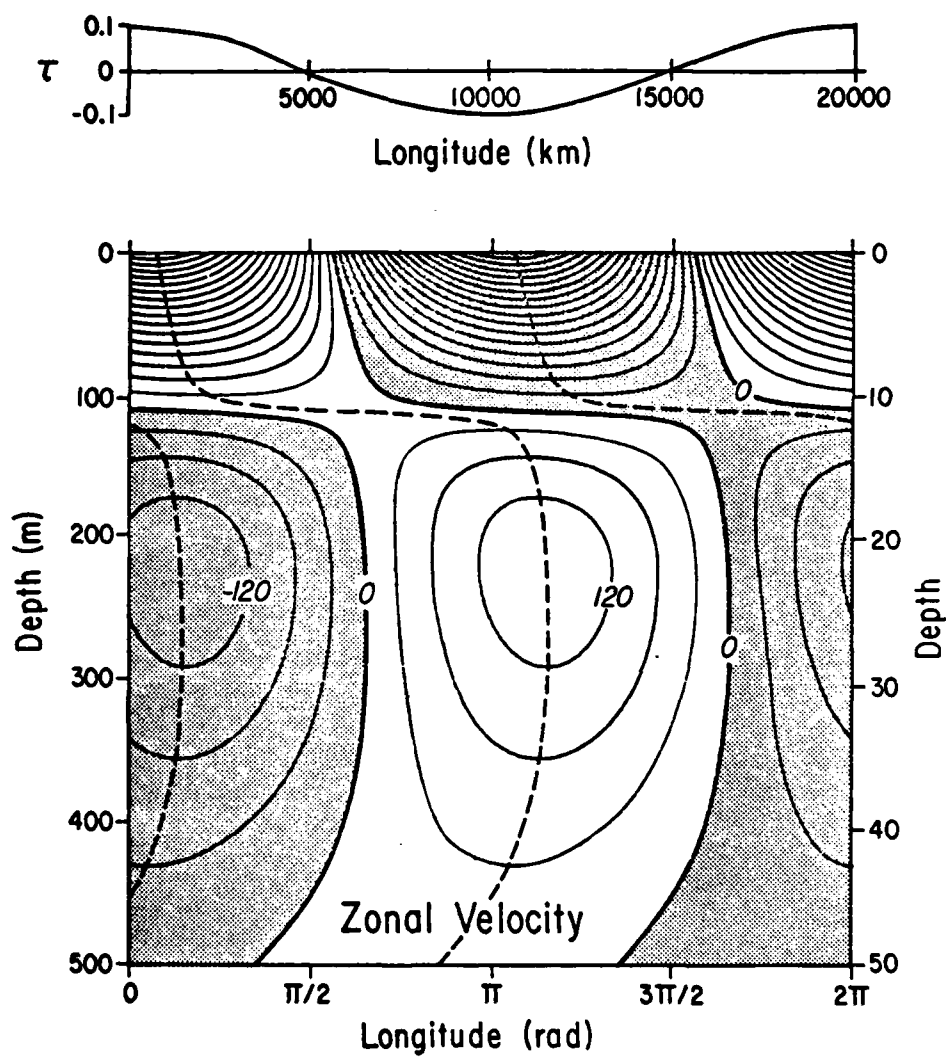


Figure 8. Zonal velocity on the equatorial plane ($y=0$) over one wavelength of the winds. Dashed lines trace velocity extrema with depth.

wind effects are important. Below, the axis of maximum velocity (dashed line) first tilts eastward with depth down to 220m such that maximum of the eastward EUC lies $.2\pi$ radians or 2000km to the east of the overlying westward wind maximum. McCreary (1980) finds a similar displacement in his results. Phase lines then reverse slope and shift westward with depth. I will elaborate on the significance of these results in the following section.

Figure 9 is a meridional section of zonal velocity over an expanded depth range of 200-1500m. The EIC appears as a narrow band of westward flow below the swifter EUC. Also evident is a deep poleward slanting geostrophic extension of the EUC suggestive of the SSCC in Figure 1. Such a feature appears in both McCreary's (1980) analytical and Philander and Pacanowski's (1980) numerical calculations.

c. Dynamics

Calculations of depth integrated quantities Q in (21) for $z_1=0$ and $z_2=-\infty$ indicate that the model ocean is everywhere in Sverdrup (1947) balance. In particular

$$V = \text{curl } \tau \quad (29a)$$

$$U = i\ell_0^{-1}(\text{curl } \tau)_y \quad (29b)$$

$$P_x = \tau^{(x)} + y(\text{curl } \tau) \quad (29c)$$

$$P_y = \tau^{(y)} - i\ell_0^{-1} y(\text{curl } \tau)_y \quad (29d)$$

This overall balance masks essential differences between the equatorial and extra-equatorial flow field though. For example, at mid-latitudes

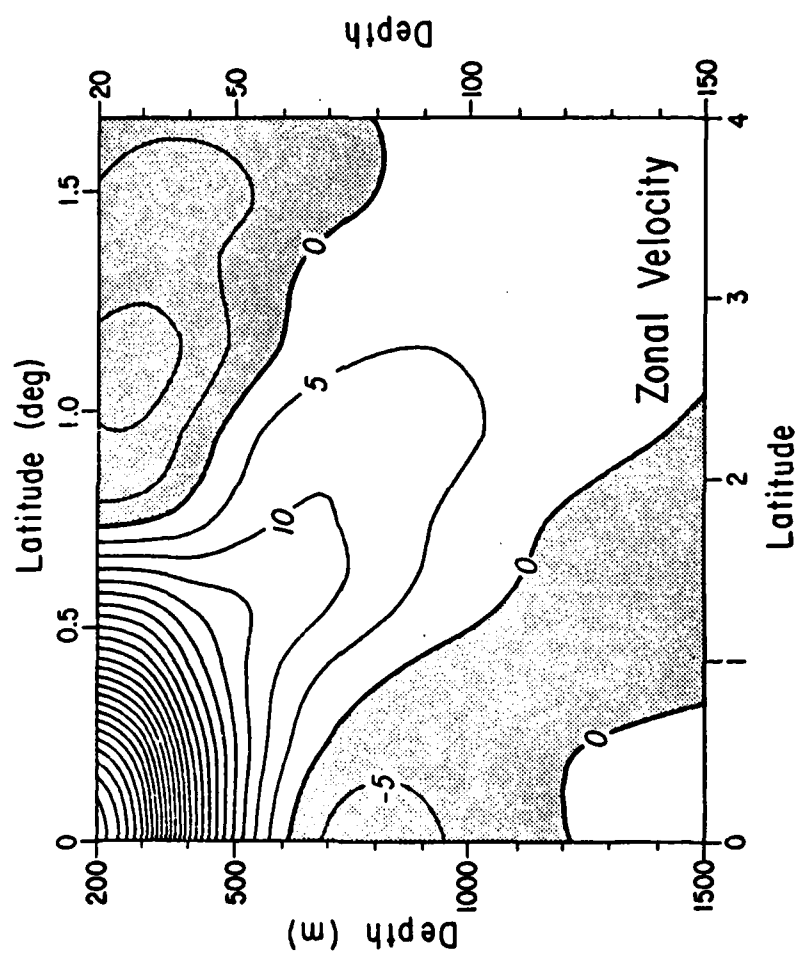


Figure 9. Meridional section of deep zonal velocity. Contour interval is 5 cm sec⁻¹; regions of westward flow are stippled.

one can decompose the Sverdrup balance into coupled Ekman and geostrophic components (Stommel, 1956). But as the equator is approached, these components develop singularities implying that the internal dynamics must be radically transformed. This transformation is the subject of the next three subsections.

i) Ekman theory

Retaining the equatorial β -plane formulation but requiring that $f = \beta y$ be locally constant, one can rederive Ekman's (1905) theory for ocean currents at mid-latitudes in the absence of horizontal pressure gradients. In nondimensional notation

$$-yu = u_{zz} \quad (30a)$$

$$yu = v_{zz} \quad (30b)$$

This balance yields surface currents 45° to the right (left) of the wind in the northern (southern) hemisphere

$$u = \frac{\tau(y) + \tau(x)}{(2y)^{1/2}}, \quad v = \frac{\tau(y) - \tau(x)}{(2y)^{1/2}} \quad (31)$$

and transports 90° to the winds

$$V = -\frac{\tau(x)}{y}, \quad U = \frac{\tau(y)}{y} \quad (32)$$

Looking for solutions to (30) of the form e^{mz} , one obtains

$$m^4 = -y^2 \quad (33)$$

which is the mid-latitude equivalent of (23a). The Ekman depth, or the depth at which horizontal velocities are down to e^{-1} of the surface

value, is defined from (34) as

$$D_e = \text{Re } m^{-1} = \left(\frac{2}{y}\right)^{\frac{1}{2}} \quad (34)$$

Finally, Ekman pumping, i.e. the vertical velocity at the base of the Ekman layer found by integrating the continuity equation is

$$w_e = U_x + V_y = \text{curl } \left(\frac{\tau}{y}\right) \quad (35a)$$

where U, V are given by (32). For the winds (27) this reduces to

$$w_e = \frac{\tau(x)}{y^2} + 2y\tau(x) \quad (35b)$$

It is evident that the mid-latitude theory (30) is valid only for $|y| \gg 0$ otherwise singularities develop in (31) - (35). This is in contrast to the Ekman part of the equatorial β -plane theory plotted as u, v contours on a meridional plane in Figure 10. Poleward of $y=2$, solutions agree with those predicted by (30): surface velocity is 45° to the right of the zonal wind, transport is all meridional (since $\tau^{(y)} = 0$) and the Ekman depth decreases with increasing latitude. However, as $y \rightarrow 0$, velocities decrease and become more meridional, transport decreases and the Ekman layer thickness does not diverge.

To understand how the equatorial Ekman layer can be well behaved, I have plotted the balance of forces at the surface in Figure 11 for just the Ekman part of the total solution. In the zonal direction, rotation balances diffusion at all latitudes since zonal pressure gradients associated with Ekman roots are uniformly small. On the other hand, as $y \rightarrow 0$, the meridional balance (30b) shifts to

$$p_y \approx v_{zz} \quad (36)$$

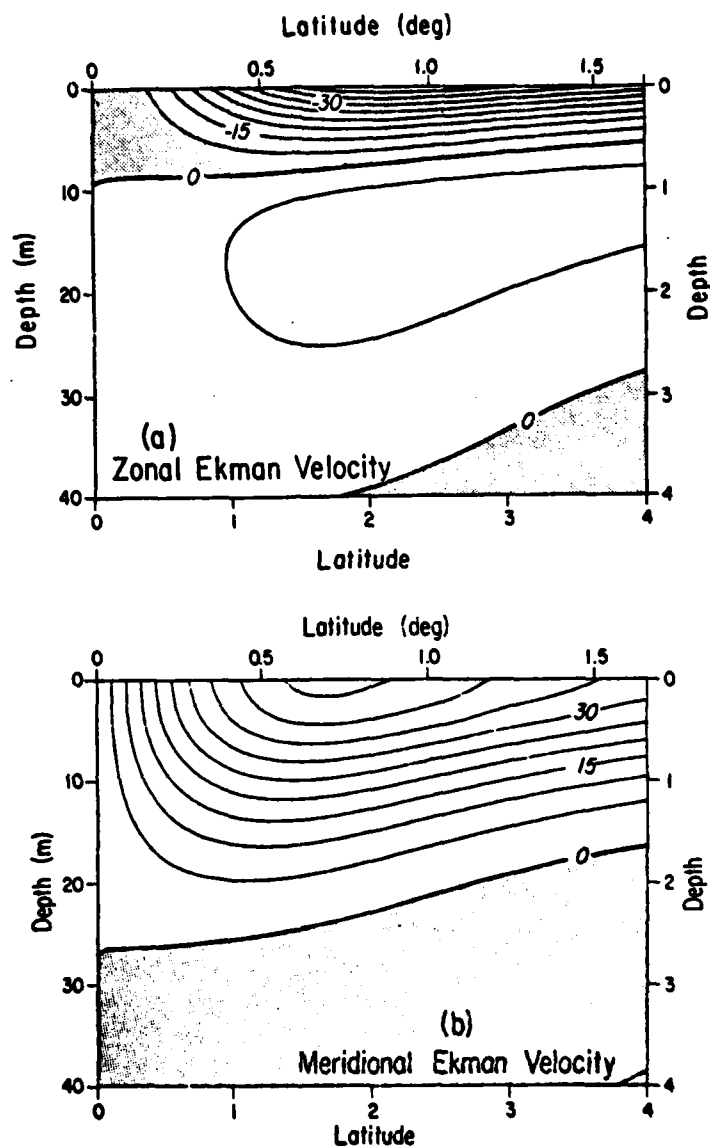


Figure 10. Meridional sections of (a) zonal and (b) meridional Ekman velocity. Contour interval is 5 cm sec⁻¹; regions of westward and southward flow are stippled.

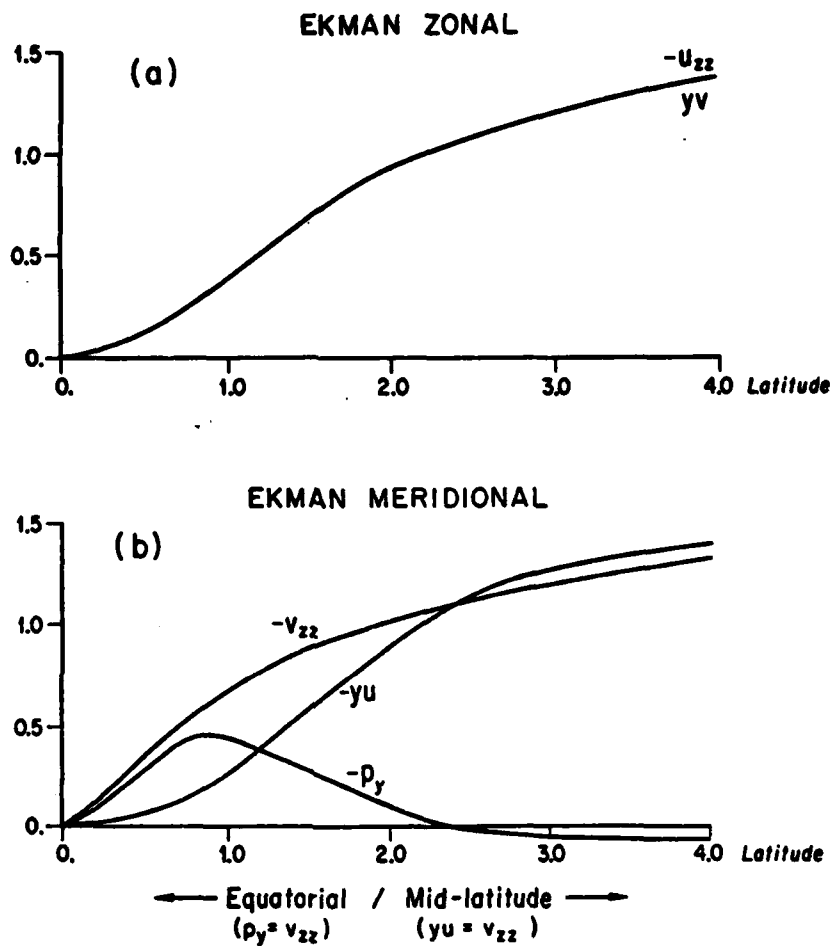


Figure 11. Balance of forces at the sea surface computed from just the Ekman modes in the (a) zonal and (b) meridional direction. Forces are in nondimensional units.

In a constant density ocean, the balance (36) is not possible and singularities develop. In the present model however, stratification removes these by allowing for baroclinic pressure gradients as in the atmospheric model of Schneider and Lindzen (1976). This result establishes more precisely the importance of stratification in the equatorial boundary layer as predicted by (1).

11) Geostrophy

Again assuming that $f = \beta y$ is locally constant, one can calculate the geostrophic flow below the mid-latitude Ekman layer from the non-dimensional set of equations

$$-yu + p_x = 0 \quad (37a)$$

$$yu + p_y = 0 \quad (37b)$$

$$u_x + v_y + w_z = 0 \quad (37c)$$

$$p_z = 0 \quad (37d)$$

$$w = -\theta \quad (37e)$$

This flow is not driven directly by the winds but indirectly via Ekman pumping (35). Dispersion for $e^{i\ell_0 x} e^{mz}$ dependence is given by

$$m^2 = -\ell_0^2 / y^2 \quad (38)$$

which is the mid-latitude equivalent of (22b).

As with mid-latitude Ekman theory, the balance (37) in the deep ocean breaks down as $y \rightarrow 0$. For example, any pressure gradient will generate infinite velocities. Also the depth scale

$$D_g = (2y^2/l_0)^{1/2} \quad (39)$$

vanishes at $y=0$. Such singularities do not appear in the deep flow calculated from the equatorial β -plane model as shown in Figure 9. There is a tendency for velocities to increase and depth scales to decrease from $y=4$ to $y=2$ in accordance with (37) and (39), but the equatorial flow is well behaved.

Figure 12 shows the balance of horizontal forces for the total solution minus the Ekman part. For $y > 2$, mid-latitude geostrophy (37) holds. As $y \rightarrow 0$, geostrophy still holds in the meridional direction (Figure 12b) but the zonal momentum balance (Figure 12a) shifts to

$$p_x \approx u_{zz} \quad (40)$$

This is essentially a Kelvin balance (16). While the sum of the geostrophic modes in (20) takes on Kelvin-like characteristics near the equator e.g. $v \sim 0$ and $u, w, p, \theta \sim \psi_0$, by far the single most important mode in the transition to (40) is the Kelvin mode itself.

iii) The Kelvin mode

Figure 13 is a plot of profiles at the equator constructed from just the Kelvin mode. Comparison with Figure 5 indicates that this mode predicts both the magnitude and vertical structure of w (away from the surface), u and p_x . Its Gaussian meridional structure $\psi_0 \sim e^{-y^2/2}$ accounts for the equatorial boundary layer width of 0 (1 Rossby radius). In addition the near surface eastward displacement of velocity extrema relative to the winds in Figure 8 is due to the Kelvin phase relationship

$$c_{xz} = \frac{dz}{dx} = - \operatorname{Im} \left(\frac{i l_0}{m} \right) = - \left(\frac{l_0}{2} \right)^{1/2} \quad (41)$$

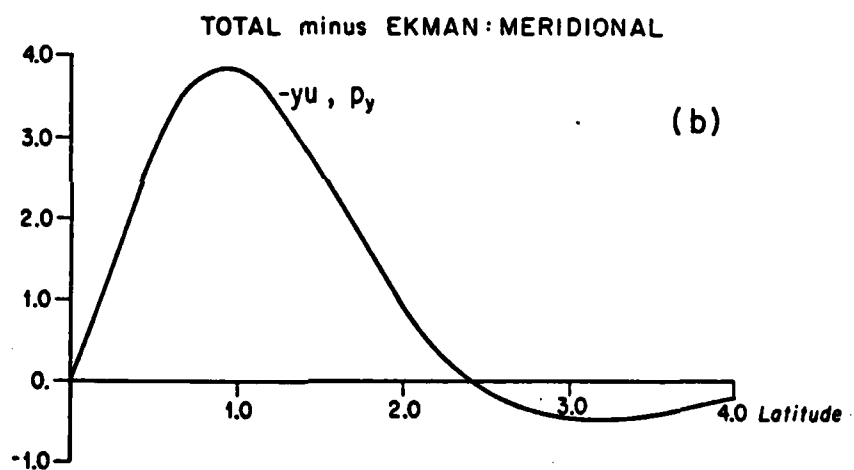
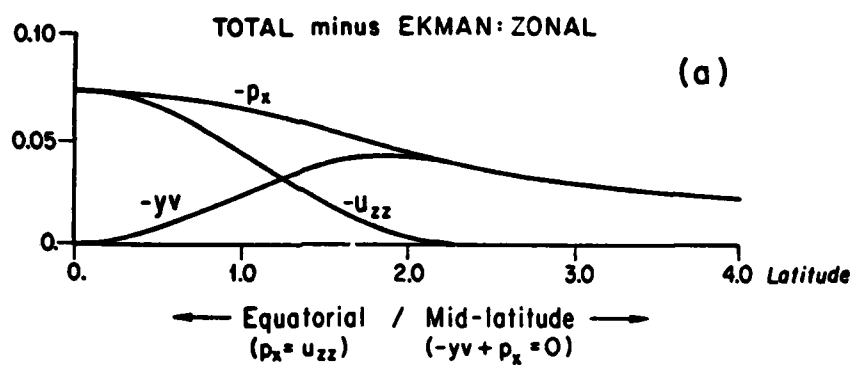


Figure 12. Balance of forces at the sea surface computed from all modes excluding the Ekman modes in the (a) meridional and (b) zonal direction. Forces are in nondimensional units.

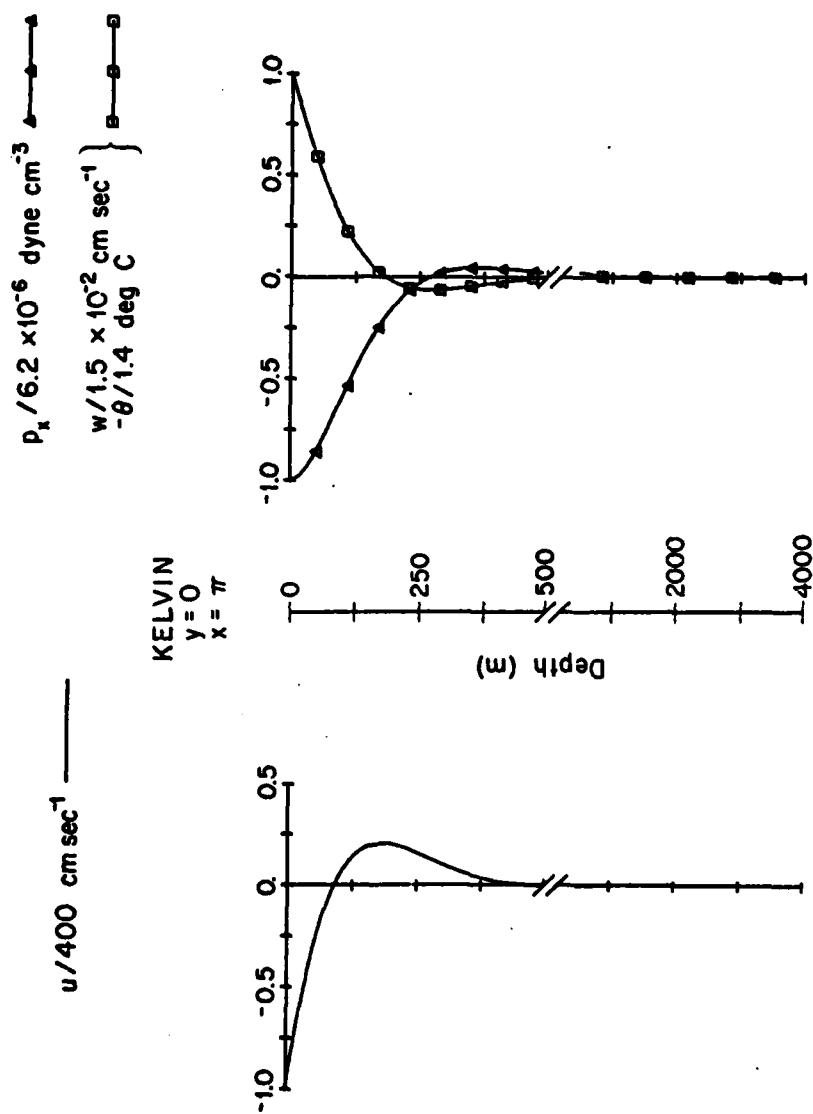


Figure 13. Depth profiles of perturbation variables on the equator computed from just the Kelvin mode.

which is found by setting $\text{Im}(mz + i\ell_0 x) = \text{constant}$ and using (18). (The westward tilt below 250m is due to geostrophic components that according to (22b) extend deeper and have $C_{xz} > 0$). In contrast to constant density models which *ab initio* set $u_x = 0$, (41) reflects the fact that u_x is important and that $v_y \equiv 0$ in the Kelvin continuity balance (16c). The physical implication of such zonal variability is that flow at a particular depth depends not only on local surface conditions but also conditions at upstream and downstream positions.

At mid-latitudes, winds project entirely onto the surface Ekman layer which in turn drives the deep ocean via Ekman pumping as described above. In contrast, zonal wind stress forces the deep equatorial ocean directly through projection onto Kelvin and geostrophic modes (Figure 14). The equatorial Ekman layer is thus of secondary importance in transferring zonal momentum from the wind field to the ocean which accounts for the weak horizontal currents near the equator in Figure 10. Its primary role is to balance a vertical velocity at the surface associated with the Kelvin (Figure 13) and weaker geostrophic modes.

The Kelvin balance (16) is not possible in a constant density ocean. Key features of the equatorial circulation related to this mode e.g. geostrophic balance of vertically sheared zonal currents, width of the boundary layer, etc. depend on stratification. These results confirm the expectation from (1) that stratification should be important not only in the equatorial Ekman layer but also in the deeper equatorial ocean as well.

3. Variation of Parameters

So far we have considered solutions only for a single zonal

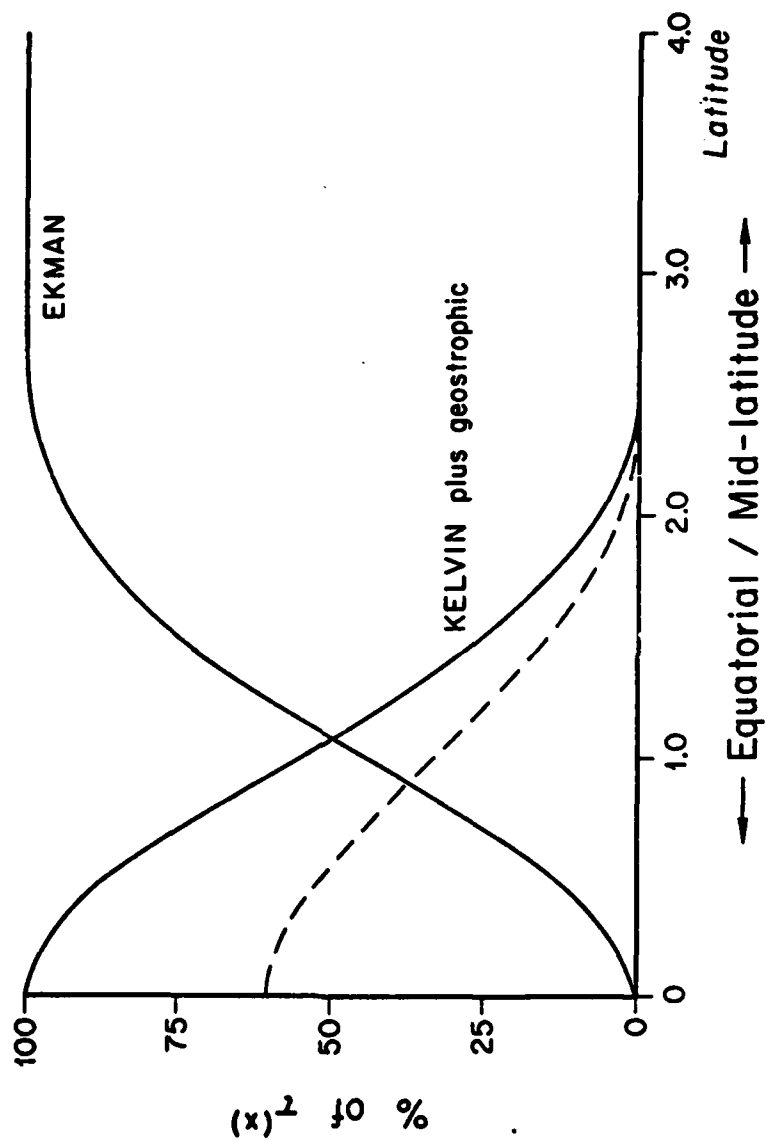


Figure 14. Percentage of zonal wind stress that projects onto the Ekman, Kelvin and geostrophic modes as a function of nondimensional latitude. The dashed line is the projection onto just the Kelvin mode.

wavenumber ℓ_0 corresponding to a wavelength of 2×10^4 km in the winds. Since observed winds consist of a spectrum of wavenumbers, it is of interest to know how sensitive the results are to ℓ_0 and what contribution other wind scales will make. Furthermore, separation of variables in the model equations requires that mean stratification and diffusivities be uniform with depth. In the ocean however, these quantities can vary over several orders of magnitude. A typical temperature profile would show a surface mixed layer ($\bar{\theta}_z \sim 0$) tens of meters thick above a sharp thermocline ($\bar{\theta}_z \sim 10^{-3} \text{ }^\circ\text{C cm}^{-1}$); deeper water is less stratified ($\bar{\theta}_z \sim 10^{-4} - 10^{-5} \text{ }^\circ\text{C cm}^{-1}$). Gregg (1976) using a Cox number model, calculated eddy heat diffusivities between $0.15 - 5.0 \text{ cm}^2 \text{ sec}^{-1}$ at 155°W on the equator. Likewise Robinson (1966), Jones (1969) and Crawford (1976) using empirical formulae, found A to range between $\sim 1 - 100 \text{ cm}^2 \text{ sec}^{-1}$. In addition, these studies indicate that the turbulent Prandtl number $\text{Pr} = K/A$ is less than unity consistent with the notion that stratification inhibits the transfer of heat more effectively than momentum (Turner, 1973).

In this section I investigate how depth, width, velocity and other properties of the equatorial circulation vary with these parameters. The control case is that of zonal wind forcing discussed in Section 2; the procedure will be to change only one of $A, \text{Pr}, \bar{\theta}_z$ or ℓ_0 holding all the rest fixed. The section concludes with a boundary layer calculation in which diffusivity and stratification vary continuously with depth on the equatorial plane.

a. Zonal Wavenumber (ℓ_0)

Because near the equator zonal winds project directly onto the Kelvin mode, one might expect from the dispersion relation (18) that increasing the zonal wavelength increases the penetration of surface

effects. One can see these developments in Figure 15 in which is a plot of zonal velocity $vs.$ depth at the equator for various λ_0 . Solid curves were calculated by the method outlined in Section C2a; the dashed curve, $u = \frac{\tau_0}{\rho_0 A} (z + H)$, is a direct calculation of the zonal momentum ($Au_{zz}=0$) for the special case $\lambda_0 = 0$. Numbers in parentheses are wavelength in thousands of kilometers.

Over two orders of magnitude, $\lambda_0 \sim 2\pi/2 \times 10^3 \text{ km} - 2\pi/2 \times 10^5 \text{ km}$, the depth of maximum eastward current increases as $\lambda_0^{-1/2}$ in accordance with (18). This trend continues until currents feel the bottom. Then further decrease to $\lambda_0 = 0$ leads to a linear shear profile over the full depth range of the ocean. Note however that the approach to this limit is slow: currents driven by winds with a zonal wavelength of $2 \times 10^5 \text{ km}$ penetrate to only about $\sim 2 \text{ km}$. Figure 15a also indicates that for currents that do not extend the bottom, the velocity decreases as $\lambda_0^{-1/2}$. The width of the equatorial boundary layer does not change with λ_0 however (Figure 15b) nor does the geostrophic balance of zonal currents below the shallow equatorial Ekman layer.

In the present model in which there are no meridional boundaries, zonal pressure gradients along the equator are generated by zonal wind convergences. Thus changing λ_0 in the wind field changes $p_x = i\lambda_0 p$ in the ocean. One can then infer from Figure 15 that baroclinic zonal pressure gradients are important a) in maintaining subsurface structure like the EUC, EIC, SCCC, etc. and b) in limiting the strength of zonal flow. McCreary (1980) arrived at similar conclusions.

b. Eddy Diffusivities (A,K) and Stratification ($\bar{\theta}_z$)

Table 1 summarizes the dependence of various scales on eddy diffusivities and stratification. One point to emerge is that increasing

ZONAL WAVENUMBER

 $u(2)/210 \text{ cm sec}^{-1}$ ———

 $u(20)/670$ " ———

 $u(200)/2100$ " ———

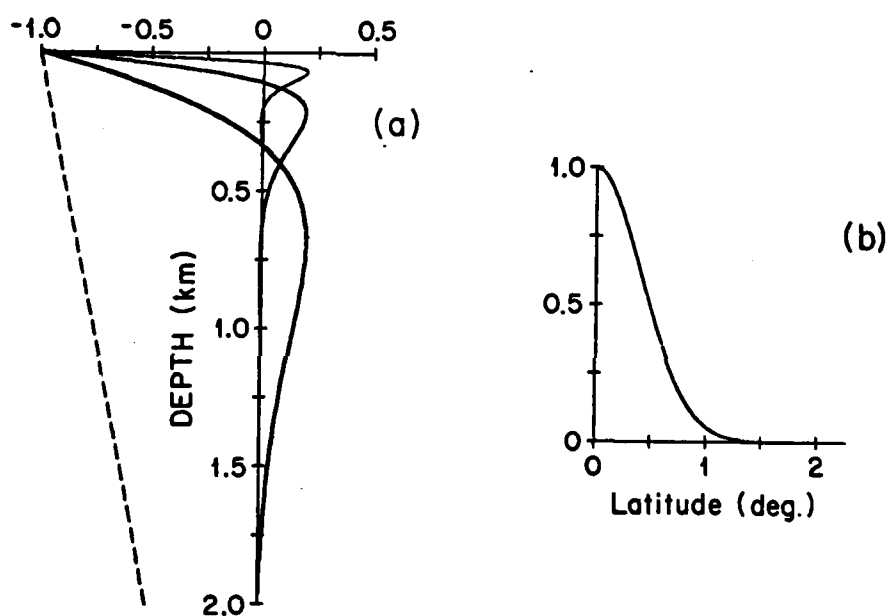
 $u(\infty)/40,000$ " - - - -


Figure 15. Effects of varying zonal wavenumber (ℓ_0) on (a) zonal velocity at the equator and (b) width of the equatorial current system plotted as ψ_0 . Numbers in parentheses are zonal wavelength ($=2\pi\ell_0^{-2}$) in thousands of kilometers. The three curves in (b) overlap.

	D	L	u	w	P	T
$A^\mu ; \mu$	3/10	2/5(1)	-7/10(-1)	-4/5(-2)	1/10(1)	-1/5
$K^\mu ; \mu$	1/10	-1/5	1/10	2/5	-3/10	-2/5
$\bar{\theta}_z^\mu ; \mu$	-1/10	1/5	-1/10	-2/5	3/10	2/5

Table 1. Power law dependence of various scales on diffusivity (A,K) and stratification ($\bar{\theta}_z$). Dependence on A when $\bar{\theta}_z = 0$ is shown in parenthesis.

stratification is indistinguishable from decreasing heat diffusivity and *vice versa* since $\bar{\theta}_z$ and K always appear in the scales (4) as a ratio $(K/\bar{\theta}_z)^\mu$. A second point is that in the limit of constant density $\bar{\theta}_z \rightarrow 0$, several scales become singular. However when the stratification is so weak i.e.

$$\bar{\theta}_z < \frac{A^3 K}{\beta^3 g \alpha H^{10}} \quad (42)$$

such that the depth scale $D > H$, the heat balance is inconsequential. The ocean is at this stage essentially constant density and the appropriate scales become

$$D = H, \quad L = \frac{A}{\beta H^2} \quad (43)$$

$$u = \frac{H}{\rho_0 A} \tau_0, \quad w = \frac{\beta H^4}{A^2} \tau_0, \quad P = \frac{A}{\beta H^3} \tau_0$$

The dependence of these scales on A is shown parenthetically in Table 1. Clearly the stratified model is less sensitive to this parameter.

Figure 16 is analogous to Figure 15 except that here we have varied A , keeping λ_0 , $\bar{\theta}_z$ and Pr fixed. Numbers in parentheses are eddy momentum (and heat) diffusivities in $\text{cm}^2 \text{sec}^{-1}$. The velocities attenuate and extend to greater depths as turbulent diffusion increases and the current system likewise expands latitudinally. As expected from Table 1 though, the solutions vary much more slowly than A . In particular the width of the equatorial flow field increases by a factor of only 2.5 when A is changed by two orders of magnitude.

Figure 17 shows the effect of varying stratification for fixed A , Pr and λ_0 . Numbers in parentheses are vertical temperature gradients

DIFFUSIVITY

 $u(1)/670 \text{ cm sec}^{-1}$ ———

 $u(10)/130$ " ———

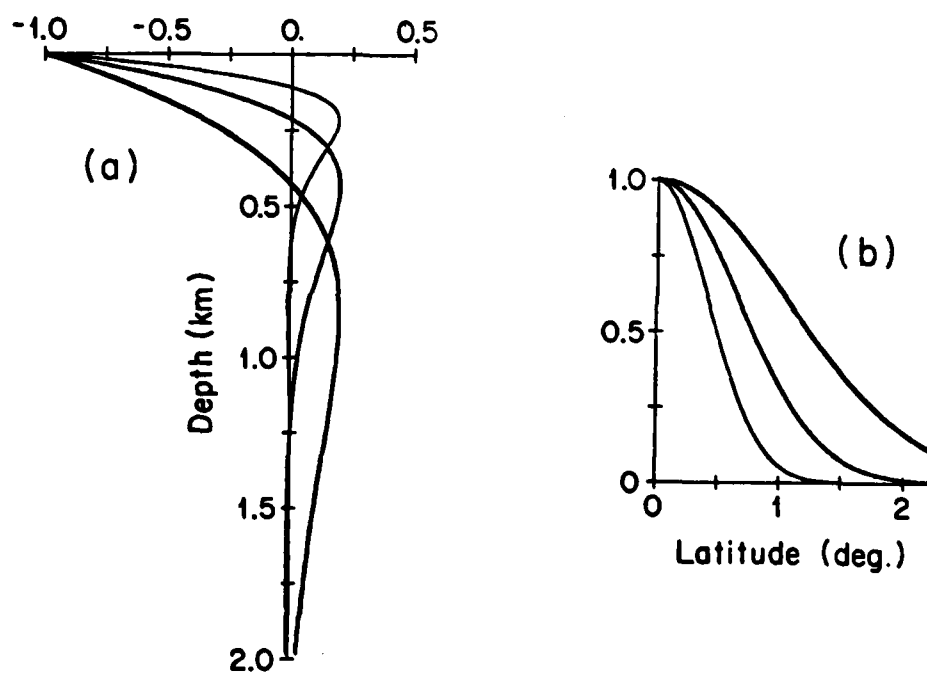
 $u(100)/27$ " ———


Figure 16. Effects of varying diffusivity (A, K) on (a) zonal velocity at the equator and (b) width of the equatorial current system plotted as ψ_0 . Numbers in parentheses are diffusivities in $\text{cm}^2 \text{ sec}^{-1}$.

STRATIFICATION; PRANDTL NUMBER

 $u(0)/20,000 \text{ cm sec}^{-1}$ - - - -

 $u(0.1)/1060$ " ———

 $u(1.0)/670$ " ———

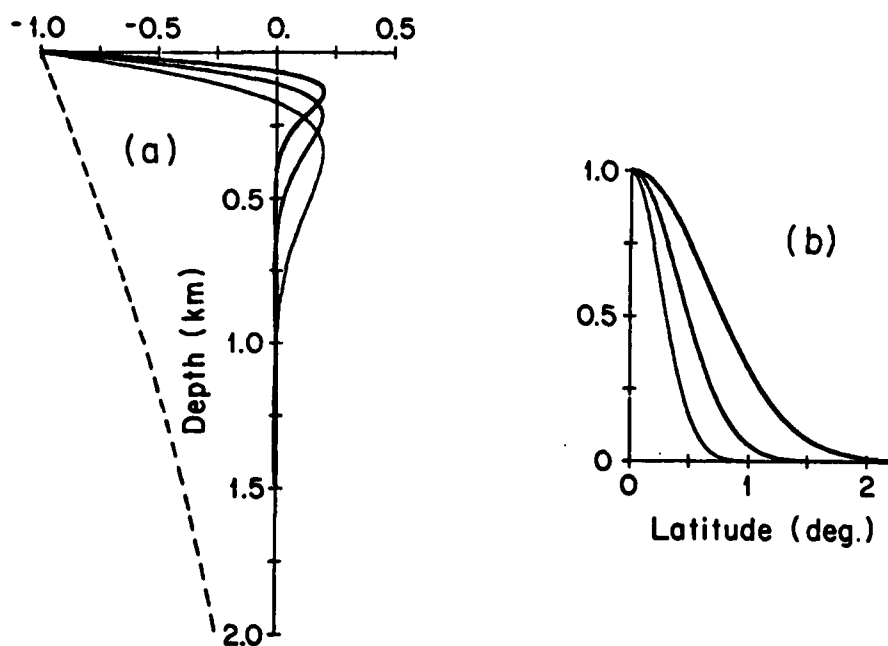
 $u(10.0)/420$ " ———


Figure 17. Effects of varying stratification ($\bar{\theta}_z$) or Prandtl number (Pr) on (a) zonal velocity at the equator and (b) width of the equatorial current system plotted as ψ_0 . Numbers in parentheses are either vertical temperature gradient in $^{\circ}\text{C}$ per 100m or Pr^{-1} .

in °C per 100 m. The dashed line, $u = \frac{\tau^{(x)}}{2\rho_0 AH} (z + H)^2$, has been calculated directly from the zonal momentum equation for the limiting case $\bar{\theta}_z = 0$ on the assumption that $\tau^{(x)}(-H) \ll \tau^{(x)}(0)$. One can see that increasing stratification limits both the depth and strength of the zonal flow, but the variation with $\bar{\theta}_z$ is weak as in the case of eddy momentum diffusivity. In fact to approach the limit case, the basic stratification must satisfy $\bar{\theta}_z < 10^{-31} \text{ °C cm}^{-1}$ for $A=K=1\text{cm}^2 \text{ sec}^{-1}$ and $H=4000\text{m}$. As seen in Figure 15b stronger stratification also leads to an increase in the width of the flow, but again the dependence is very weak. The width corresponding to $\bar{\theta}_z = 0$ is not plotted, according to (43) it is only about 25 cm! Furthermore, in this limit zonal currents at the equator are not geostrophic as discussed in the previous section.

As mentioned earlier, the effects of changing stratification are indistinguishable from changing the heat diffusivity. Thus one can alternately interpret Figure 17 in terms of varying the Prandtl number for fixed A , $\bar{\theta}_z$ and λ_0 . The numbers of parentheses are then simply Pr^{-1} .

It is interesting to note that while D , L and U all vary with A , K and $\bar{\theta}_z$, the scale for mass transport $UDL (= \tau_0 / \rho_0 \beta)$ is independent of these parameters.

c. An Approximate Analysis

I now develop a simple model that allows both stratification and eddy diffusivities to vary continuously with depth. In this way one can introduce a surface mixed layer into the problem. The analysis is based on the dominance of the Kelvin mode near the equator and is valid only on the equatorial plane (i.e. $y=0$).

Assuming $v \equiv 0$,

$$p_x = (A' u_z)_z \quad (44a)$$

$$y u + p_y = 0 \quad (44b)$$

$$u_x + w_z = 0 \quad (44c)$$

$$p_z = 0 \quad (44d)$$

$$w = - \frac{K'}{\bar{\theta}_z'} \theta \quad (44e)$$

where A' , K' , $\bar{\theta}_z'$ are nondimensional, depth variable quantities scaled by their depth averaged dimensional values A , K , $\bar{\theta}_z$:

$$A_{\text{dim}} = A A' \quad (45a)$$

$$K_{\text{dim}} = K K' \quad (45b)$$

$$(\bar{\theta}_z)_{\text{dim}} = (\bar{\theta}_z) \bar{\theta}_z' \quad (45c)$$

If the vertical velocity boundary conditions are relaxed, (44) can be solved at the equator where winds project entirely onto Kelvin-like flow (Figure 14) subject to

$$A u_z' = \tau(x) \quad @ z = 0 \quad (46a)$$

$$u = 0 \quad @ z = -H \quad (46b)$$

Combining (44c-e) leads to

$$u_x = \left(\frac{K'}{\bar{\theta}_z'} p_z \right)_z \quad (47)$$

which by comparison with (44a) yields a well posed problem if

$$u = p ; \quad A' = \frac{K'}{\bar{\theta}'_z} \quad (48)$$

For the winds in Figure 4, (44a), (47) and (48) lead to

$$u_{zz} + \frac{A'_z}{A'} u_z - i \frac{\rho_0}{A'} u = 0 \quad (49)$$

This equation is trivially solved by standard Runge-Kutta techniques for arbitrary $A'(z)$.

I analyze two cases characterized by depth averaged parameter values of $A=K=1\text{cm}^2 \text{ sec}^{-1}$ and $\bar{\theta}'_z = 10^{-4} \text{ }^\circ\text{C cm}^{-1}$ such that the same scales (4) apply to both. First, assume that A' , K' , $\bar{\theta}'_z$ are depth independent which is simply the problem considered more exactly in Section C2. The solution to (49) is plotted as a light solid line in Figure 18. One can see by comparison with Figure 5 that this curve approximates both the amplitude (to within 15%) and vertical structure of zonal velocity. Now compare this control case to one in which

$$A' = \max (0.51 , 100e^{-\delta z}) \quad (50a)$$

$$K' = 1 \quad (50b)$$

$$\bar{\theta}'_z = \min (1.96 , 0.01e^{-\delta z}) \quad (50c)$$

where min (max) implies the minimum (maximum) value in parentheses is taken and $\delta = 0.5$. In dimensional terms, this recipe (50) calls for strong mixing near the surface ($A_{\text{dim}} \sim 100 \text{ cm}^2 \text{ sec}^{-1}$) in a shallow mixed layer ($\sim 10^{-6} \text{ }^\circ\text{C cm}^{-1}$) below which viscosity and stratification are constant at $0.51 \text{ cm}^2 \text{ sec}^{-1}$ and $1.96 \times 10^{-4} \text{ }^\circ\text{C cm}^{-1}$. Plots of A_{dim} and $\bar{\theta}_{\text{dim}}$

KELVIN APPROXIMATION

$u_c / 570 \text{ cm sec}^{-1}$ —————

$u / 570$ " —————

$A / 100 \text{ cm}^2 \text{ sec}^{-1}$ ······

$\bar{\theta} / 30 \text{ deg C}$ - - - - -

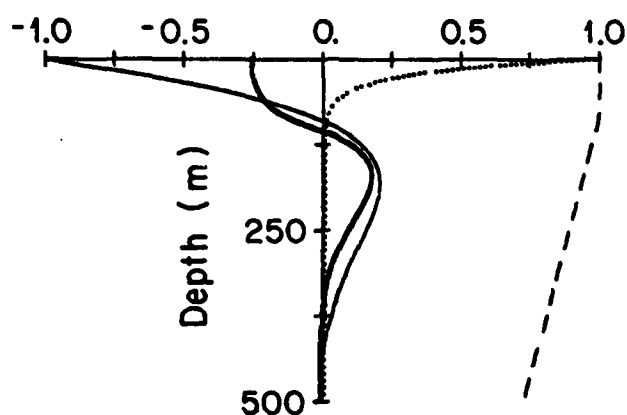


Figure 18. Approximate solution computed from just the Kelvin mode on the equator. The zonal velocity u_c has been calculated for depth invariant A , K and $\bar{\theta}$; u has been calculated for A and $\bar{\theta}$ as shown.

appear in Figure 18.

The heavy line in Figure 18 is the solution to (49) for (50). Compared to the control case, surface velocities are much reduced and more slab-like. McCreary (1980) finds similar behavior in the mixed layer of his model. Conversely at the level of the EUC where parameter values are comparable, flow is much less modified. Slower decay of current speed below the EUC in the first case can be ascribed to the slightly higher diffusivity there ($1\text{cm}^2 \text{sec}^{-1}$ vs. $0.51 \text{cm}^2 \text{sec}^{-1}$). In both cases there is a nonzero vertical velocity at the surface (not shown) that would be nullified if a shallow Ekman layer were included.

4. Meridional Winds

In this section I examine the solution to (5) for meridional winds of the form

$$\tau^{(y)}(x,y) = \tau_0 e^{i\ell_0 x} e^{-\gamma y^2} \quad (51)$$

which is identical to (27) except for the direction. Other physical parameters are the same as in the zonal wind case. The method of solution is that discussed in Section C2a but now v_z ($z=0$) is projected onto even ψ_n . Thus v has even symmetry in latitude and u, w, p, θ have odd symmetry.

a. Flow Description

Because only v is nonzero at the equator, Figure 19 displays profiles of dynamical variables in the equatorial boundary layer at $y=0.5$. Winds from the north drive a surface flow 25° to the right of the forcing (or by symmetry to the left in the southern hemisphere) and simultaneously upwelling (downwelling in the south). Below the south-

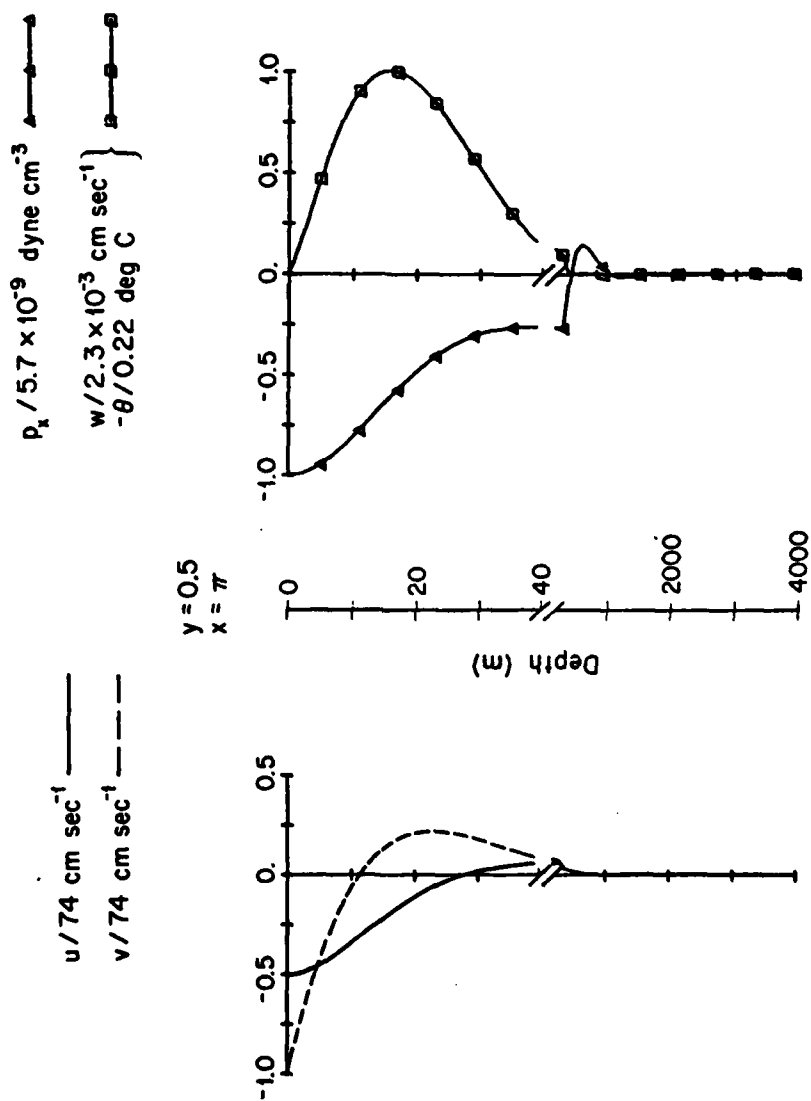


Figure 19. Depth profiles of perturbation variables in the equatorial boundary layer for southward winds.

ward surface drift is a northward return flow. Zonal pressure gradients are not important and there is no significant structure below 40m. For nondimensional latitudes $y \geq 1$, flow is similarly confined to the upper 40m in a classical Ekman layer. Figure 20 shows the circulation on a meridional plane at the longitude of maximum southward winds. North (south) of the equator, upwelling (downwelling) is forced by meridional divergence (convergence) whereas at the equator there is no vertical motion. Cromwell (1953) argued for a similar circulation pattern under the influence of meridional winds based on various tracer distributions in the equatorial Pacific.

Aside from obvious symmetry characteristics, two features distinguish the response of an equatorial ocean to meridional vs. zonal winds. First, for the same magnitude wind stress τ_0 , zonal forcing generates currents an order of magnitude stronger than meridional as seen from the relative scales in Figure 5 and Figure 19. Second, zonal wind effects penetrate deeper. One can clarify these differences by comparing the dynamics of each case.

b. Dynamics

As in the case of zonal winds, depth integrated quantities for $\tau^{(y)}$ forcing obey the Sverdrup relations (29). Moreover, the Ekman component of flow undergoes a similar transformation as $y \rightarrow 0$ viz. $-yu = u_{zz}$ everywhere but $(yu = v_{zz}) \rightarrow (p_y = v_{zz})$ in the equatorial boundary layer. However the winds (51) do not excite a significant geostrophic component. At mid-latitudes this is due to weak Ekman pumping

$$w_e = U_x = i\ell_0 \frac{\tau^{(y)}}{y} \quad (52)$$

which compared to w_e for zonal winds (35b) is $O(y\ell_0) \ll 1$. Near the

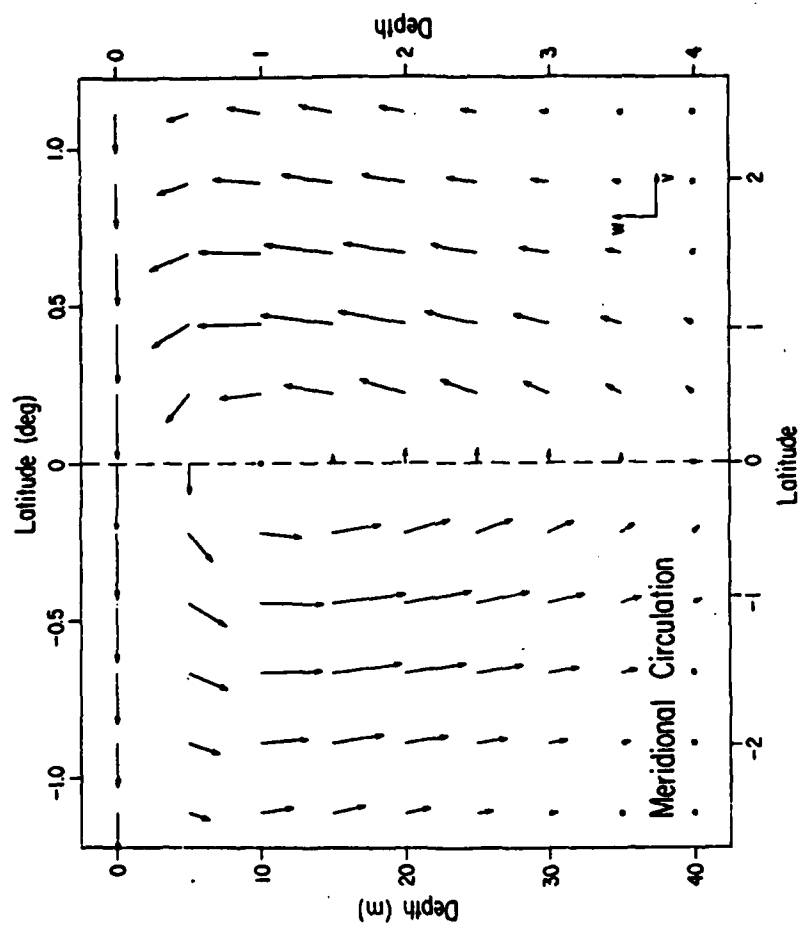


Figure 20. Meridional circulation in the equatorial boundary layer for southward winds. Scales for v and w shown at lower right are 50 cm sec^{-1} and $2.0 \times 10^{-3} \text{ cm sec}^{-1}$ respectively

equator zonal winds project directly onto Kelvin-like flow which is in cross-stream geostrophic balance and which extends to several hundred meters depth. Conversely, meridional winds project almost entirely onto the gravest mode in v , i.e. $n=0$ in Figure 3. As $\ell_0 \rightarrow 0$, the dispersion (15) for this mode does not yield a geostrophic root so that the dynamics are predominantly frictional and strongly surface trapped. The frictional nature of the response also accounts for its weakness: even modest deformations of the thermal field near the equator if geostrophically balanced would lead to much larger velocities.

A more subtle distinction between zonal and meridional wind forcing is that in the latter case, flow at any given longitude is influenced by local winds only and not by winds at neighboring longitudes. Plots of variables on the x - z plane exhibit no change of phase with depth i.e. $C_{xz} = 0$ (cf. Figure 8). This is due to the fact that for the Ekman roots, not only is p_x negligible in (5a) but also u_x is negligible in the continuity equation (5d).

5. Discussion

The essential ingredients of the present steady state theory are variable rotation and continuous density stratification. The linearized mathematical formulation precludes meridional boundaries and allows only for highly idealized types of winds. In spite of its simplicity though, results show much in common with oceanic observations. For a range of parameters, realistic width, depth and velocity scales are predicted that do not depend too strongly on the eddy coefficients. Geostrophic zonal flows reminiscent of the SEC, EUC, EIC and SSCC can be generated along with convincing meridional circulation patterns. Baroclinic

zonal pressure gradients provide the source of momentum for deep zonal flows near the equator.

In Section C2c it was shown that meridional baroclinic pressure gradients maintain a well behaved equatorial Ekman layer contrary to the qualitative notion stemming from constant density models that singularities should develop there. In the case of zonal winds, the Ekman layer is characterized by weak horizontal currents because most or all of the wind stress at a particular latitude projects directly onto Kelvin and Kelvin-like geostrophic flow. This geostrophic flow diffuses vertically (unlike at mid-latitudes) and is associated with a surface vertical velocity which the Ekman layer nullifies. The response to large scale meridional winds on the other hand is entirely confined to a shallow surface frictional layer.

Baroclinic meridional pressure gradients that develop in the equatorial Ekman layer imply a temperature distribution that is not in geostrophic balance. Thus, shallow temperature anomalies due to frictional effects represent a source of error in the geostrophic calculation of near surface equatorial flows. This error can be severe in the presence of winds with a strong southerly or northerly component since frictionally induced meridional temperature gradients are nonzero even at the equator in this case. For strictly zonal winds, the relative size of Ekman and geostrophic pressure gradients (p_y) shown in Figures 11 and 12 indicates an error of $\sim 10\%$ at $y=1$.

The model suggests deep baroclinicity like that observed by Luyten and Swallow (1976) and Luyten and Eriksen (1980). From (22b) and (38), the vertical wavenumber at high latitudes is very small implying a strongly barotropic interior flow. As the equator is approached, the

wavenumber progressively increases and asymptotes to the Kelvin wavenumber given by (18) for which the vertical wavelength is only a few hundred meters. The model differs from the observations though in that (18) predicts a much more rapid decay from the surface.

Meridional winds or zonal winds with a meridional shear produce zonal currents antisymmetric around the equator. In a constant density ocean, either of these in combination with easterlies leads to an EUC structure centered off the equator. In a stratified ocean, the response to antisymmetric zonal winds (which has been calculated but not presented) and meridional winds (Section C4) is confined to a shallow surface Ekman layer. Conversely, geostrophic flow driven by zonal wind stress extends much deeper (Section C2). Thus in the present model, meridional or antisymmetric zonal winds do not result in an asymmetric EUC structure. Such structure in a linear calculation is then only possible if time dependence is introduced (q.v. Chapter III). On the other hand, Philander (1973b) suggested that in a stratified ocean nonlinear effects may produce a steady displacement of the EUC off the equator in response to meridional winds.

Observations suggest that the maximum speed of the EUC lies to the east of the maximum westward wind stress as predicted by the model (Figure 8). Current measurements between 140°W and 90°W (Knauss, 1960) indicate a broad EUC velocity maximum centered near 115°W. Long term averages of the Pacific Trade Wind field along the equator (Knauss, 1963; Meyers, 1979) show maximum easterlies located near 140°W. This agreement with the model may be fortuitous however since the current measurements were made only in Spring, 1958. If wave processes have contaminated the

record, the pattern of zonal velocity so described may not be representative of the long term average. No suitable combination of velocity and wind data are available in the Atlantic to compare with the theory.

Even though observations indicate that nonlinearity is important in the EUC, this and McCreary's (1980) strictly linear calculation produce remarkably realistic flow patterns. Hence as with constant density models, inertial terms derived from a linear theory may predict the effects of nonlinearity. For the case of zonal winds (27), I computed uu_x , vu_y , wu_z (zonal momentum), uv_x , vv_y , wv_z (meridional momentum) and $u\theta_x$, $v\theta_y$, $w\theta_z$ (heat balance) as a function of latitude and depth at the longitude of maximum easterlies. Results show that quadratic terms in the heat and meridional momentum balances are small relative to the linear terms. In the zonal direction, plots of nonlinear terms relative to the dominant linear term (u_{zz} near the surface, p_x below) reveal that nonlinearity is important in the equatorial boundary layer but not at mid-latitudes. For example Figure 21 shows that at the core of the EUC below the westward wind maximum there is both equatorward advection of eastward momentum ($vu_y > 0$) which tends to narrow the flow and downstream advection ($uu_x > 0$) which tends to reduce its strength. Above and below the core, there is a gain in eastward momentum ($wu_z < 0$) which tends to increase the vertical extent of the EUC. A comparison of linear and nonlinear numerical calculations in Philander and Pacanowski (1980, Figure 12) reveals similar tendencies.

The model shows spreading isotherms near the equator, but it also develops temperature inversions (Figure 22). The near surface ones are due to the restriction that $\theta = w = 0$ at $z = 0$. Downwelling immediately below the surface can then carry warmer water to

NONLINEAR TENDENCIES

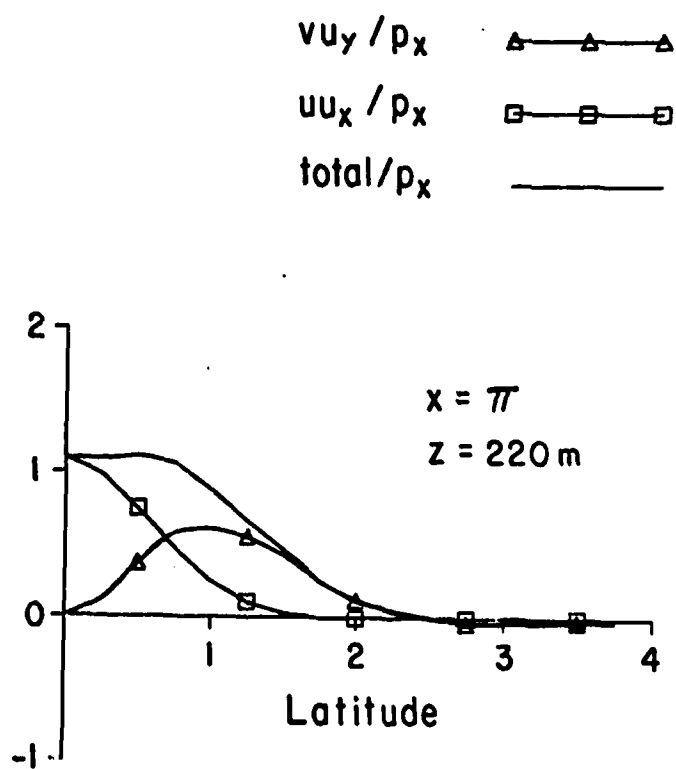


Figure 21. Nonlinear tendencies as a function of non-dimensional latitude at the depth of the EUC core.

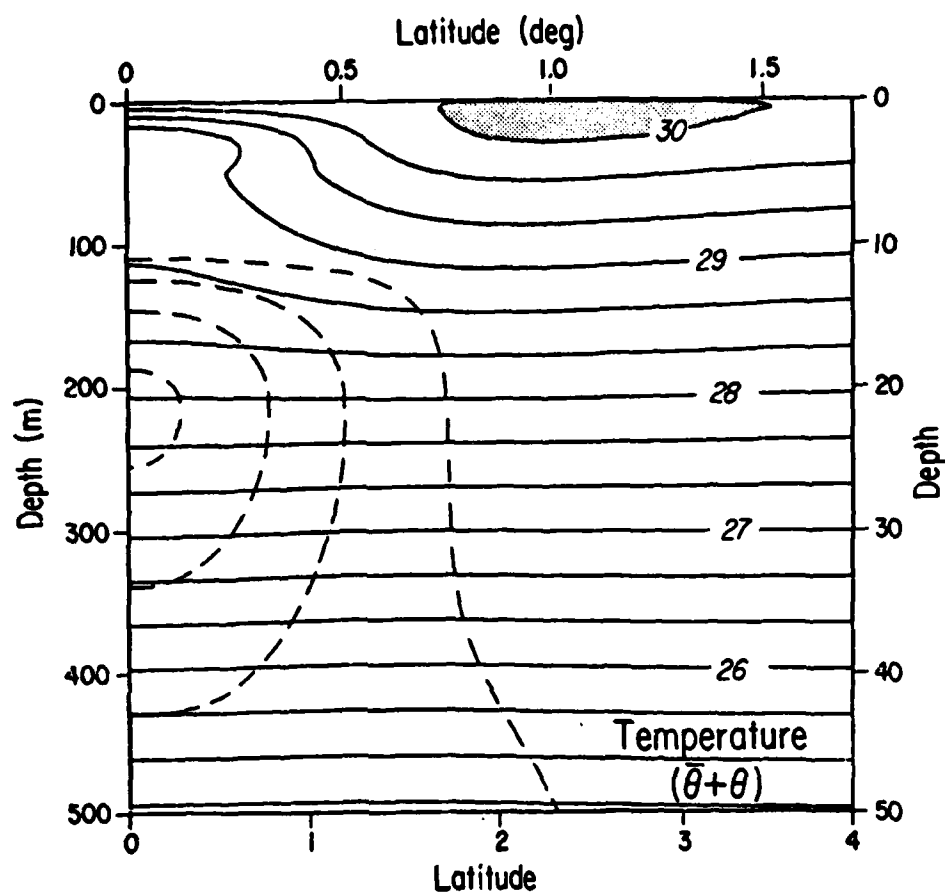


Figure 22. Meridional section of total temperature. Contour interval is 0.33 °C; the stippled area represents water warmer than the surface temperature. Superimposed are isotachs of eastward velocity in the EUC (dashed lines).

depth raising ambient temperature above the surface value which cannot change. Above the EUC the inversions are due to stronger vertical advection of the background temperature field near the surface than below. Colder water is thus carried from greater depth to rest over warmer water. McCreary's (1980) linearized heat balance leads to similar inversions. These static instabilities imply strong mixing through a convective adjustment process and suggest that the parameterization of turbulent conduction in this study is inadequate. The next section explores an alternate parameterization scheme.

D. Biharmonic Friction Model

Under this heading I develop a model which incorporates the conventional Laplacian turbulent heat diffusion (proportional to a second derivative) as well as a less common biharmonic vertical friction (proportional to a fourth derivative). Though solutions will be compared with the Newtonian cooling case, the purpose is not to demonstrate the superiority of one type of parameterization over another. It is rather to show that important dynamical balances are insensitive to details of these schemes. The particular formulation discussed in Section D1 leads to separable solutions on the y - z plane as in the Newtonian cooling case. Section D2 is an examination of the response to zonal winds like those of (27) and Section D3 discusses thermally forced solutions. Section D4 is a brief recapitulation and commentary.

1. Formulation

Using the same notation as in Section 6, governing equations are

$$-\beta y v + \frac{1}{\rho_0} p_x = - (A D^2 u_{zzz})_z \quad (53a)$$

$$\beta y u + \frac{1}{\rho_0} p_y = - (A D^2 v_{zzz})_z \quad (53b)$$

$$p_z = \rho_0 g \alpha \theta \quad (53c)$$

$$u_x + v_y + w_z = 0 \quad (53d)$$

$$w \bar{\theta}_z = (K \theta_z)_z \quad (53e)$$

subject to

$$\begin{aligned} -\rho_0 A u_{zzz} &= \tau(x), \quad -\rho_0 A v_{zzz} = \tau(y), \quad \theta_z = 0 \\ u_{zz} &= v_{zz} = w = 0 \quad \text{at } z=0 \end{aligned} \quad (54a)$$

$$u = v = w = \theta_z = u_{zz} = v_{zz} = 0 \quad \text{at } z = -H \quad (54b)$$

$$u, v, w, p, \theta \rightarrow 0 \quad \text{as } |y| \rightarrow \infty \quad (54c)$$

Biharmonic friction distinguishes this model from nearly all other ocean general circulation models which typically use Laplacian vertical momentum diffusion. The biharmonic formulation is less unusual in parameterizing horizontal turbulence in numerical eddy resolving models (e.g. Holland, 1978) where it strongly damps grid scale fluctuations but not mesoscale eddies. The logic for its introduction into (53) is that the equations now separate in all three directions.

The form of the stress boundary conditions in (54a) guarantees that the ocean will be in Sverdrup balance. However, the additional derivatives in (53a,b) require another boundary condition on u and v at the top and bottom. I have assumed the null hypothesis for velocity curvature, i.e. $u_{zz} = v_{zz} = 0$. Temporarily the perturbation heat flux (proportional to θ_z) is set to zero at both upper and lower boundaries, though the upper condition can be relaxed or replaced by a surface temperature condition (Section D3). Hereafter A and K will be assumed constant.

From (53) and (54) one can produce a set of equations in which all terms are $O(1)$ by invoking the scaling arguments (4). A single 12th order equation in v follows

$$v_{(12z)} - v_x - v_{xx}(4z) - [v_{yy} - y^2 v]_{(4z)} = 0 \quad (55)$$

which has separable solutions of the form

$$v(x,y,z) = \int_{-\infty}^{\infty} \sum_{n=0}^{\infty} \hat{v}_n(\ell,y,z) e^{i\ell x} d\ell \quad (56)$$

$$\hat{v}_n = \sum_{j=1}^{12} a_{n,j}(\ell) e^{m_{n,j}(\ell)z} \psi_n(y)$$

The Hermite functions ψ_n are again governed by (9) but the vertical dependence $\phi = e^{mz}$ obeys

$$\phi_{(12z)} + (2n+1+\ell^2) \phi_{(4z)} - i\ell\phi = 0 \quad (57)$$

provided that

$$m^{12} + (2n+1+\ell^2)m^4 - i\ell = 0 \quad (58)$$

holds for $n > 0$. The quantities u, w, p, θ follow from (56) and the non-dimensional version of (53).

As with the Newtonian cooling model (Section C), there are roots of (58) for $n = 0$, i.e. $m^4 = i\ell$ that results in ill behaved \hat{u}_0 at high latitude. Eliminating these leads to an analogue of (15)

$$m^8 + i\ell m^4 + 1 = 0 \quad (59)$$

In addition there is an $n=-1$ Kelvin mode with $v \equiv 0$ and

$$m^4 = -i\ell \quad (60)$$

We could have obtained (55) and (57)-(60) from their equivalents in Section C1 by the transformation $\frac{\partial}{\partial z} \rightarrow i(\frac{\partial}{\partial z})^2$, $m \rightarrow im^2$. Thus the analogy with equatorial waves as well as with mid-latitude Ekman and geostrophic theory is preserved. Specifically as $\ell \rightarrow 0$, (58) reduces to

$$m^0 = -(2n+1) = -y_t^2 \quad (61a)$$

$$m^1 = i\ell/(2n+1) = i\ell/y_t^2 \quad (61b)$$

The roots (61a) imply a different vertical structure than traditional Ekman theory (23a) but they are still surface trapped, steady state, frictional analogues of inertia-gravity waves. Likewise (61b) corresponds to the steady state Rossby wave analogues (22a) and (22b).

2. Zonal Winds

a. Method of Solution

Equations (53) and (54) are solved according to the method outlined in Section C2a for winds of the form (27) shown in Figure 4 and for parameter values $A=K=40\text{cm}^2 \text{ sec}^{-1}$, $\bar{\theta}_z=10^{-4} \text{ }^\circ\text{C cm}^{-1}$. The values of A, K were chosen such that the core of EUC-like flow appeared at the same level ($\sim 220\text{m}$) as in the Newtonian cooling case. (Values of $A=K=1\text{cm}^2 \text{ sec}^{-1}$ resulted in high wavenumber vertical structure near the surface that bore no resemblance to observed flow features). Appropriate scales are $D=43\text{m}$, $L=97\text{km}$, $U=11\text{cm sec}^{-1}$, $W=4.7 \times 10^{-3}\text{cm sec}^{-1}$, $P=2.3 \times 10^2 \text{ dyne cm}^{-2}$ and $T=0.22 \text{ }^\circ\text{C}$; nondimensional zonal wavenumber (ℓ_0) and meridional decay scale (γ) are 3.0×10^{-2} and 9.3×10^{-3} respectively.

For the above winds and parameter values, bottom trapped solutions are much less important than surface trapped and are therefore neglected. In addition, $u_{zz}=v_{zz}=\theta_z=0$ at $z=0$ can be satisfied by setting $a_{n,j}=a_{n,j+3}$, $j=1,2,3$. Thus with \vec{B} given by (28), \vec{A} is trivially solved for the reduced set of boundary conditions $-u_{zzz}=\tau^{(x)}$, $v_{zzz}=w=0$ at $z=0$. The series expansions for q were truncated at $n=N=57$.

b. Flow Description

Figure 23 shows depth profiles on the equator at the maximum in westward winds. As in the Newtonian cooling case, one finds an SEC, EUC and an EIC which is stronger relative to the shallow currents. Above the EUC core and at the surface, upwelled water is cooler while downwelling in and below the core is associated with warmer water. An eastward baroclinic zonal pressure force drives the EUC and reverses at depth to drive the EIC. Even though the diffusivities are stronger in this model, the vertical wavelengths in Figure 23 are decidedly smaller than in Figure 5. This is consistent with the generally smaller depth scales predicted by (60) and (61b) relative to their counterparts (18) and (22b). On the other hand, stronger diffusivity leads to weaker velocity and temperature scales.

Figure 24 is a meridional section of zonal velocity on the northern half plane ($0 \leq y \leq 4$) down to 1500m. The width of the current system is twice that shown in Figure 8 being closer now to the observed width of 150km. A tongue of geostrophic eastward momentum sloping downward toward the poles emanates from the EUC much like the SSCC in Figure 1. A similar tongue of westward momentum emanates from the EIC.

Meridional circulation in the upper 500m resembles that shown in Figure 7b though somewhat reduced in amplitude. A meridional section of temperature on the same plane (Figure 25) shows cooler water at the surface in the equatorial boundary layer and doming (troughing) above (below) the EUC core. These effects are in qualitative agreement with the observations though of weaker intensity. Moreover, the temperature field is statically stable everywhere in contrast to that in Figure 22.

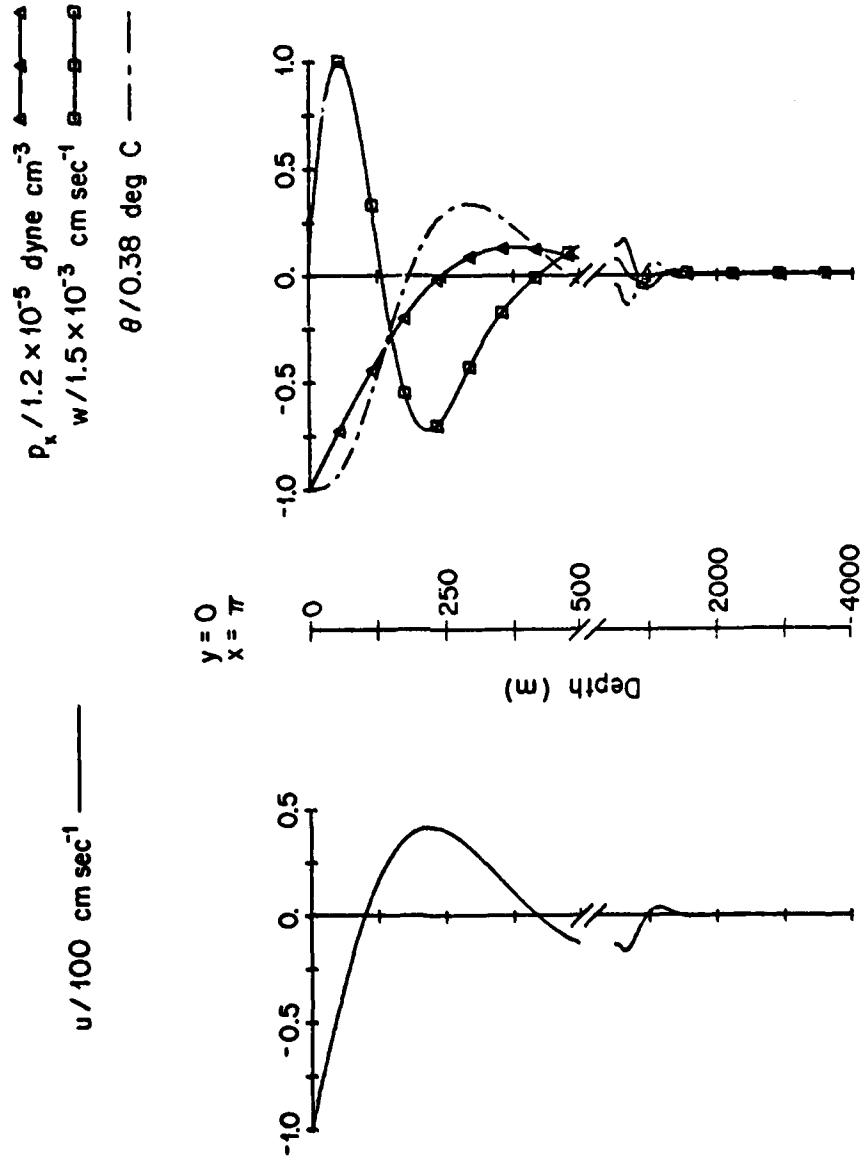


Figure 23. Depth profiles of perturbation variables on the equator for the biharmonic friction model.

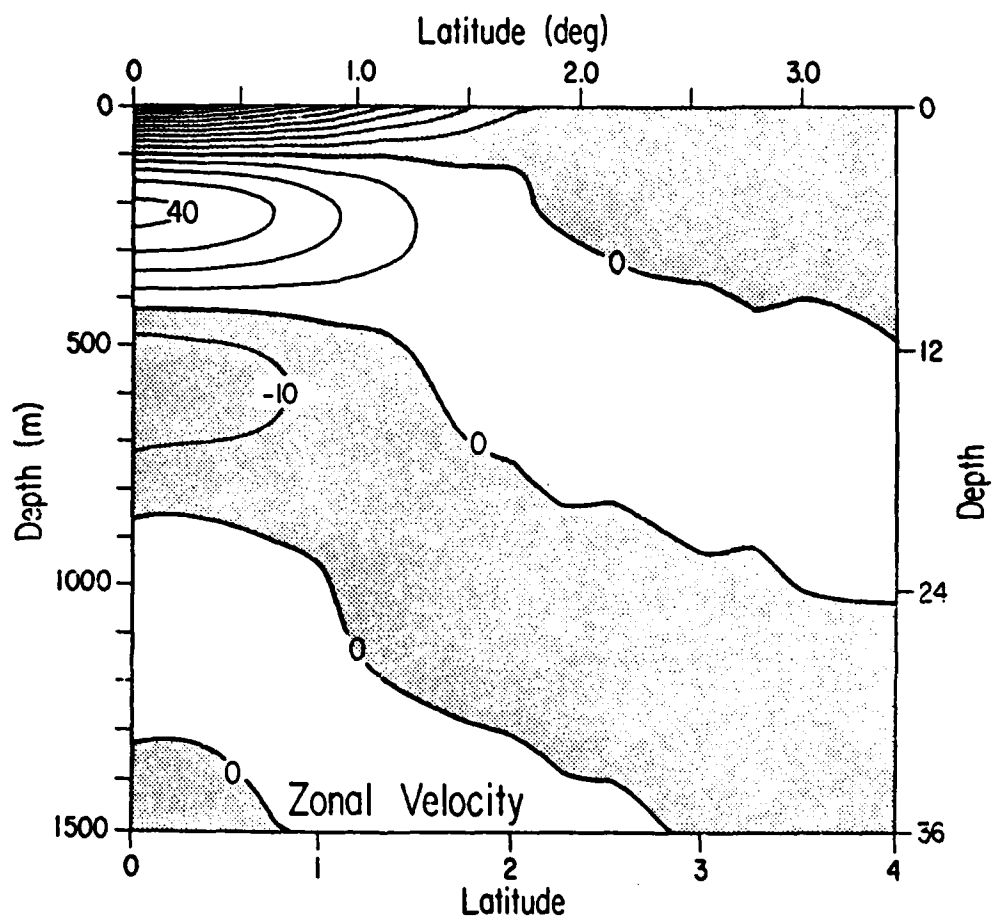


Figure 24. Meridional section of zonal velocity for the bi-harmonic friction model. Contour interval is 10 cm sec⁻¹; regions of westward flow are stippled.

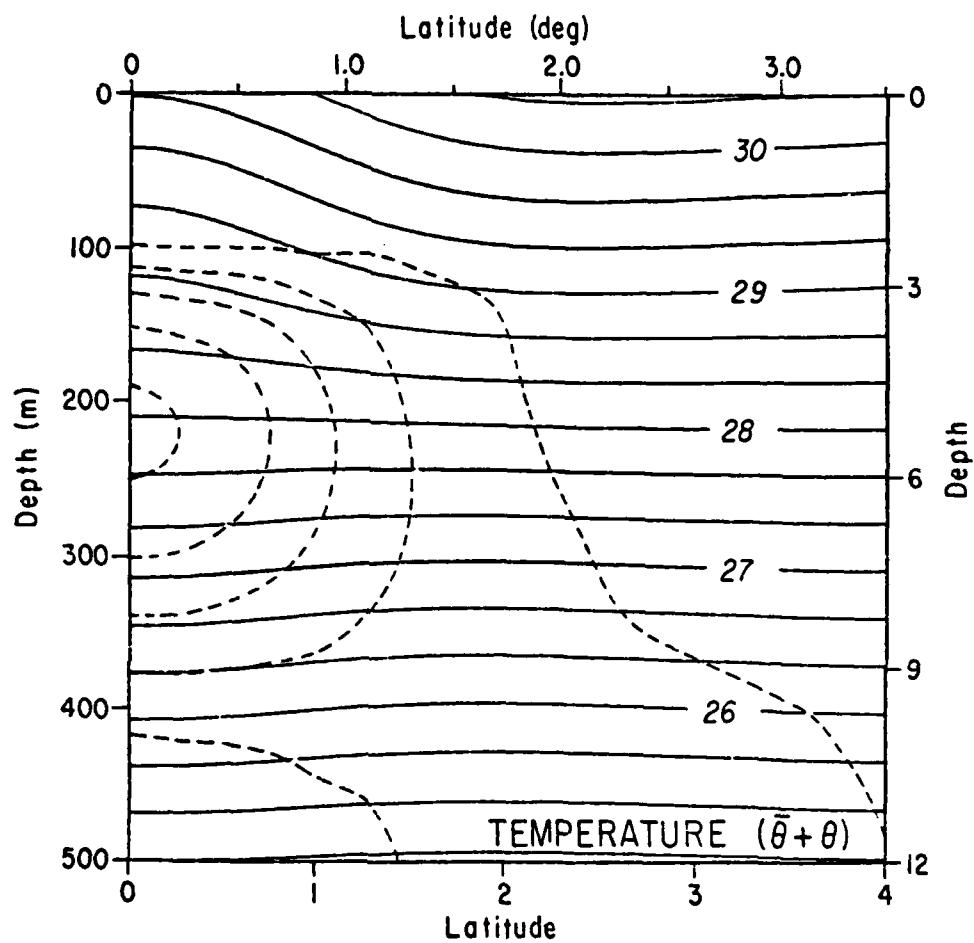


Figure 25. Meridional section of total temperature for the biharmonic friction model. Contour interval is 0.33 °C. Superimposed are isotachs of eastward velocity in the EUC (dashed lines).

AD-A083 780

SCRIPPS INSTITUTION OF OCEANOGRAPHY LA JOLLA CA
MODELS OF THE EQUATORIAL OCEAN CIRCULATION.(U)
1980 M J MCPHADEN

F/G 8/3

UNCLASSIFIED

N00014-75-C-0152

NL

2-2

1.000000

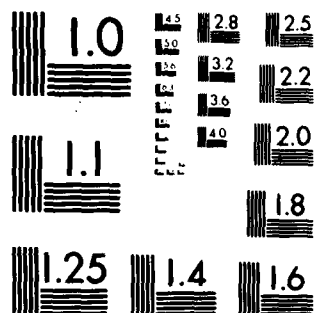
END

DATE

FILED

6 80

DTIC



MICROCOPY RESOLUTION TEST CHART
NATIONAL BUREAU OF STANDARDS 1963-A

c. Dynamics

As stated earlier, the choice of boundary conditions (54) guarantees that the model ocean is in Sverdrup balance at all latitudes. The flow can then be examined in terms of a shallow Ekman component and a deep geostrophic component. The balance of forces in the Ekman layer is identical to that shown in Figure 11 except the diffusive terms are now biharmonic. Similarly, the balance for deeper motion is given by Figure 12 indicating that the Kelvin mode is of central importance in the equatorial boundary layer. As in Figure 14, winds project onto the Ekman layer at mid-latitudes and directly onto geostrophic zonal flow at low latitudes. The essential purpose of the equatorial Ekman layer is again to eliminate surface vertical velocities associated with the deeper flow.

The similarity between the dynamics of this and the Newtonian cooling model is not surprising since I have simply invoked a different parameterization for turbulent dissipation. This has not altered the substance of the force balance, but merely changed certain details of the flow patterns. For example in the northern hemisphere, surface velocity is 68° to the right of the wind in the mid-latitude Ekman layer as opposed to 45° . The Ekman layer is also deeper: $D_e \sim O(\frac{1}{y})^{\frac{1}{2}}$ as opposed to $D_e \sim O(\frac{1}{y})^{\frac{1}{2}}$. On the other hand, Ekman transports are still 90° to the right of the wind since they are not sensitive to the form of the diffusion operators.

3. Thermal Forcing

The present model allows for either perturbation heat flux forcing or specification of surface temperature. I will briefly discuss so-

lutions for the latter in the absence of wind stress. The scales D and L in (4) are unchanged but

$$u = \frac{g\alpha D}{\beta L^2} T, \quad w = \frac{g\alpha D^2}{\beta L^2} T \quad (62)$$

$$P = g\alpha\rho_0 DT$$

where T is the temperature scale. The form of the temperature boundary condition is identical to stress condition (27) and parameter values are $A=K=40\text{cm}^2 \text{sec}^{-1}$, $\bar{\theta}_z=10^{-4} \text{ }^\circ\text{C cm}^{-1}$. Thus for $T=1.0 \text{ }^\circ\text{C}$, $u=49\text{cm sec}^{-1}$, $w=2.2\times 10^{-2} \text{ cm sec}^{-1}$ and $P=4.3\times 10^3 \text{ dyne cm}^{-2}$. Series expansions for q were truncated at $n=N=17$ and solved by the method described in Section C2a.

Figure 26 shows profiles at the equator and at the longitude of maximum zonal surface temperature gradient ($x=3\pi/4$). Colder water lies to the west, warmer to the east. This temperature gradient sets up baroclinic pressure forces that drive zonal currents much like those in the wind driven cases. Furthermore temperature and vertical velocity bear the same relationship to these currents e.g. upwelling (downwelling) above (below) the eastward velocity maximum correlated colder (warmer) water. The width of the current system is again $O(L)$.

The ocean is in Sverdrup balance, though all depth integrated quantities in (29) are zero because $\tau = 0$. The Kelvin mode dominates the equatorial ocean as in the case of zonal winds. Ekman layers (Figure 27) are needed because the deep flow cannot satisfy all the surface boundary conditions alone. In the absence of winds, the strength of Ekman layer is proportional to the strength of the deep

$p_x / 4.5 \times 10^{-6} \text{ dyne cm}^{-3}$ —●—
 $w / 1.7 \times 10^{-3} \text{ cm sec}^{-1}$ —■—
 $\theta / 1.3 \text{ deg C}$ ---

$u / 110 \text{ cm sec}^{-1}$ —

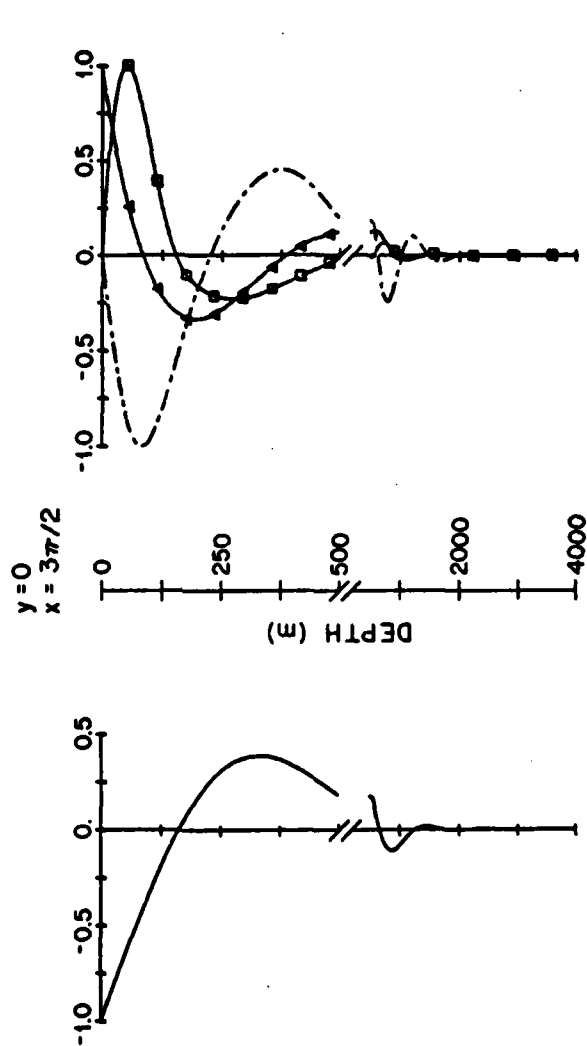


Figure 26. Depth profiles of perturbation variables on the equator for surface temperature forcing.

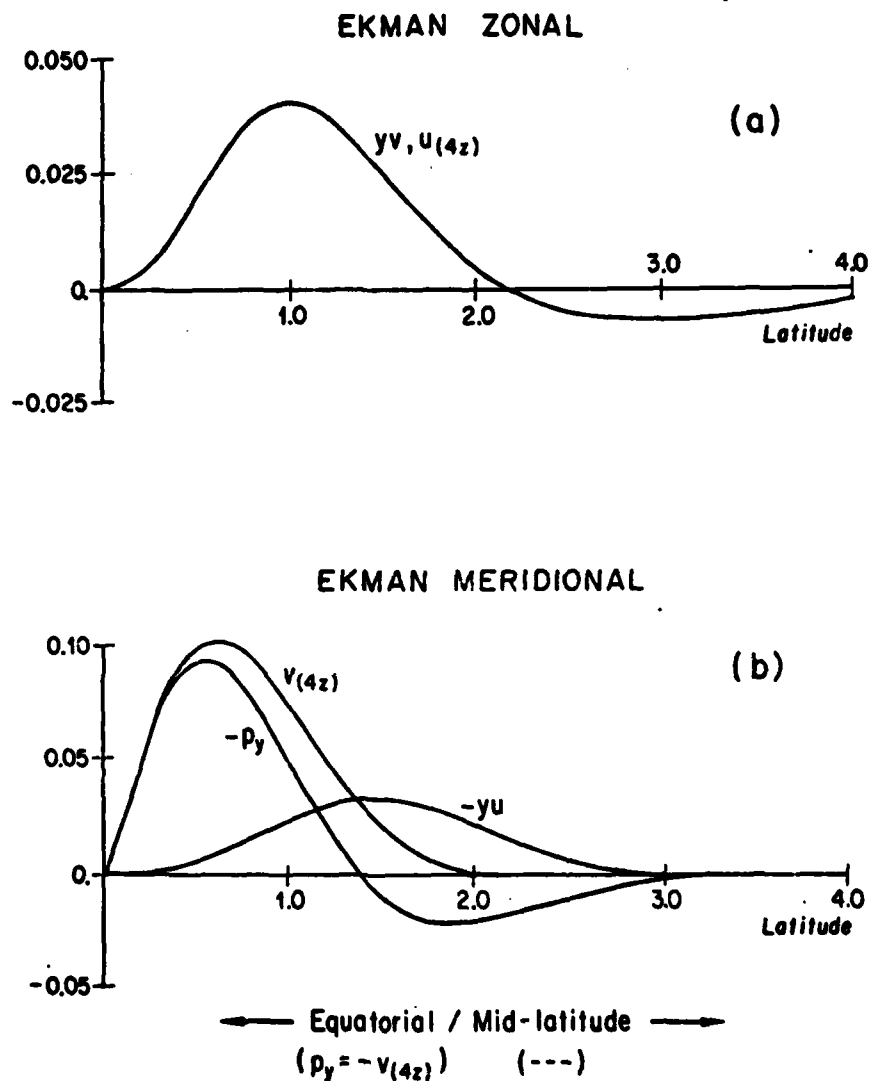


Figure 27. Balance of forces at the sea surface for surface temperature forcing computed from just the Ekman modes in the (a) zonal and (b) meridional direction. Forces are in nondimensional units.

flow. This leads to stronger equatorial rather than mid-latitude Ekman layers in contrast to the wind driven cases (cf. Figure 11).

These results together with Philander's (1973a) more complicated equatorial thermocline calculations indicate that zonal surface temperature gradients can have a significant effect on subsurface flow structure. Models that attempt to accurately describe the equatorial current system must therefore account for observed surface temperature variations. This will require a better understanding of equatorial mixed layer dynamics and thermodynamics than we have at present.

4. Discussion

I have examined the physics of a linearized, stratified equatorial ocean in both Newtonian cooling and biharmonic friction models. In either case, easterly winds excite flows that resemble the SEC, EUC, EIC and SSCC. The models also predict equatorial upwelling and thermocline weakening in qualitative agreement with observations. The biharmonic friction model gives more realistic length, depth and velocity scales for a range of parameters; it also provides a better representation of the temperature field and allows surface thermal forcing. The dynamics of both models are identical. In particular, well behaved Ekman layers are present at all latitudes and the equatorial boundary layer is characterized by a vertically diffusive, geostrophic Kelvin balance.

These models are distinguished from McCreary's (1980) linearized, stratified, vertically diffusive model by their ability to separate and follow the development of Ekman and geostrophic layers as they approach the equator. McCreary employs diffusion operators which, unlike the

Newtonian cooling and biharmonic friction formulations, lead to a Sturm-Liouville eigenvalue problem for the vertical dependence. The eigenmodes either individually or in groups cannot be identified with Ekman or geostrophic dynamics as was done with the exponential modes ϕ in Section C1. Moreover, the biharmonic friction model allows surface thermal forcing which was not allowed in McCreary's model. However these differences, resulting from different turbulence parameterizations do not obscure basic similarities between the two models which have been commented on throughout the text. Thus, this and McCreary's (1980) work should be viewed as complementary approaches to understanding steady equatorial dynamics.

To stimulate discussion, extensive comparison has been made between model results and observations. However the purpose of this study has not been to simulate ocean flows. Rather it is hoped that the results of this work will clarify important processes in more complicated numerical models and also motivate further modeling of the equatorial ocean.

CHAPTER III

EQUATORIAL KELVIN AND INERTIO-GRAVITY WAVES IN ZONAL SHEAR FLOW

Theories of the equatorial ocean circulation have evolved along two separate and distinct lines. In Chapter II I discussed the older of these, viz. frictional models of the mean flow which date from the mid 1950's. While they contribute to our understanding of steady equatorial dynamics, an obvious limitation of such models is their inability to account for the wide variety of temporal fluctuations found in modern oceanic measurements. To overcome this limitation, linear, time dependent, inviscid equatorial wave theory was developed in the early 1960's. Wave theory has since provided satisfying descriptions of heretofore puzzling oceanic phenomena such as the initiation of an El Niño (McCreary, 1977), Somali Current dynamics (Lighthill, 1969; Anderson and Rowlands, 1976) and sea level variability (Wunsch and Gill, 1976). However the basic theory is formulated for small amplitude perturbations in an ocean with no mean currents. Considering the observed strength ($\sim 100 \text{ cm sec}^{-1}$) of the EUC and SEC, it is likely that waves and steady currents interact in manner that neither wave nor current theory alone can predict. This chapter is one of the first attempts to

include in an equatorial wave model mean flows like those observed in the tropical ocean.

Reprinted from JOURNAL OF PHYSICAL OCEANOGRAPHY, Vol. 9, No. 2, March 1979
 American Meteorological Society
 Printed in U. S. A.

Equatorial Kelvin and Inertio-Gravity Waves in Zonal Shear Flow

M. J. MCPHADEN AND R. A. KNOX

Scripps Institution of Oceanography, University of California, San Diego, La Jolla 92093

(Manuscript received 30 June 1978, in final form 15 September 1978)

ABSTRACT

The interaction of geostrophic zonal mean currents in an equatorial ocean with free, neutrally stable, internal Kelvin and inertio-gravity waves is investigated using a two-layer, reduced-gravity model. Solutions in the inertio-gravity range are obtained by a simple numerical integration scheme that allows several different background flows to be tested. It is found that, due to the interaction, the amplitudes and latitudinal distributions of wave zonal velocity are substantially altered from those which would occur in the absence of mean flow. Meanders of currents similar to those observed during GATE may be interpreted as advectons of mean currents by wave meridional velocity. On the other hand, wave pressure (sea level) and meridional velocities are not greatly affected by the mean flow. These results may be of importance in attempting to fit equatorial wave theories to observations of zonal current, on the one hand, and of sea level fluctuations on the other.

Kelvin waves are treated using a perturbation expansion based on the small ratio of mean current speed to wave phase speed. The shear flow alters low-frequency Kelvin waves only slightly, introducing a small meridional velocity and a Doppler shift which could affect the speed of baroclinic adjustments in the tropics. At higher frequencies, the Kelvin wave becomes more like an inertio-gravity wave and may appear in velocity records as varicose meanders of the background current.

1. Introduction

The theory of time-dependent motion in the tropics is distinguished from midlatitude theories by the fact that the Coriolis parameter changes sign at the equator, creating a waveguide in which there can be no net meridional propagation of energy. Within the waveguide, two types of motion unique to the tropics are found (Fig. 1). First, internal eastward-traveling Kelvin waves can exist in the absence of physical boundaries. Because their group velocity is the fastest of any open ocean internal wave, they afford a most efficient mechanism for the zonal transfer of energy and momentum, substantially reducing baroclinic adjustment times at low latitudes. For example, both McCreary (1976) and Hurlburt *et al.* (1976) found in simulations of El Niño that when the easterlies relax in the tropics, internal Kelvin waves excited at the western boundary can cross a basin several thousand kilometers wide in 1–2 months. Various authors have shown that wind-generated Kelvin waves in the western Atlantic are capable of producing the seasonal upwelling signals observed along the coast of Guinea, at the opposite side of the ocean (Moore *et al.*, 1978; Adamec and O'Brien, 1978). These and other studies suggest that Kelvin waves should be a prominent feature of the equatorial circulation, although none have been detected in the ocean (Wunsch, 1977a).

The second class of motions shown in Fig. 1 con-

sists of long inertio-gravity waves which for low-order vertical modes typically have periods between ~2 days and ~2 weeks and wavelengths >2500 km. This group of intermediate frequency disturbances is of geophysical interest because it includes waves which by virtue of their small zonal group velocity are preferentially excited by random local forcing. It also includes the mixed Rossby-gravity or Yanai wave. Matsuno (1966) argued that because of the existence of such free modes, one should in principle expect more energy at periods between a few days and a few weeks in the open equatorial ocean than at midlatitudes. Many investigators have found this energy (Wunsch, 1977a), but to identify it with particular waves is difficult because most studies have lacked the necessary spatial and/or temporal resolution. One notable exception is the Wunsch and Gill (1976) study of Pacific sea level variability. Using a data base consisting of long sea level and weather records from widely scattered island stations, they concluded that first baroclinic mode equatorial inertio-gravity waves excited by local winds were responsible for the significant energy found in the 4-day and 5-day bands. Their calculations necessarily emphasized spectral resolution, leaving considerable amplitude uncertainty in their results.

Aside from the lack of data, a fundamental problem in interpreting oceanic phenomena in terms of equatorial waves lies in the limitations of the linear theory itself. Specifically, little is known about how

these waves interact with highly sheared mean currents such as those encountered in the tropical oceans since most of the basic theory of time-dependent equatorial motion (e.g., Blandford, 1966; Matsuno, 1966; Moore, 1968; Moore and Philander, 1977) considers perturbations linearized about a state of rest. Existing theories of wave-mean shear interaction in the atmosphere (Boyd, 1978) cannot be applied directly to the ocean since they depend on perturbation analyses in which the small parameter is the ratio of vertical or meridional wave scales to corresponding mean shear scales; in the ocean, this ratio is $O(1)$ or larger.

The purpose of this paper is to investigate the Kelvin wave and the long, intermediate-frequency inertio-gravity waves in the presence of strong, meridionally sheared geostrophic jets appropriate to the equatorial ocean. We treat these disturbances in a two-layer model in which zonal background flows are confined to the upper layer in which the wave scales are comparable to those of the first baroclinic mode in a realistically stratified ocean. The analysis for this system is especially simple because the phase speeds are much greater than typical mean current speeds so that there are no critical layers and no growing instabilities. Slower waves, i.e., those associated with higher vertical modes, could be unstable, but we do not consider these. Furthermore, because we are not attempting to simulate a particular set of observations but rather to isolate the structural and dispersion modifications due to mean currents in a few of the gravest horizontal modes, no forcing is imposed on the system.

In related work Philander (1976; 1978a) adapted the discrete layer model to a discussion of critical layers in highly sheared zonal flows along the equator. He found that baroclinic instabilities are suppressed in the tropics and that westward flows are more barotropically unstable than eastward. For typical values of oceanic parameters, the fastest growing disturbances propagated westward with periods in excess of three weeks and wavelengths shorter than 2000 km. He also found solutions corresponding to longer, neutrally stable waves, but these were not discussed in detail.

Hallock (1977) used a similar three-layer numerical model with $O(40 \text{ cm s}^{-1})$ mean currents in the upper two layers to simulate meanders of the undercurrent and South Equatorial Current observed during Phase II of the GARP Atlantic Tropical Experiment (GATE) (Düing *et al.*, 1975). He impulsively stressed the surface of the ocean at a fixed (2400 km) wavelength with a northerly wind stress anomaly, thereby exciting a neutrally stable, Yanai-like disturbance that advected the mean currents back and forth across the equator with the observed 16-day period and zonal phase propagation. Higher frequency gravity waves appeared as noise at the

same wavelength; Kelvin waves were not excited due to the symmetry of the forcing.

Most recently, Philander (1979) has considered neutrally stable Kelvin and inertio-gravity waves in a two-layer numerical model with eastward shear flow in the upper layer. For typical values of oceanic parameters, he finds that Kelvin waves are Doppler-shifted to higher frequency and have meridional velocities which increase with increasing frequency. This meridional velocity does not affect the geostrophic balance of the zonal currents except at periods < 8 days, beyond which the waves become more like inertio-gravity oscillations. He also found that the dispersion of inertio-gravity waves is little changed by the presence of eastward currents, but details of the wave structures were not discussed.

There is overlap between the Philander (1979) study and the one presented here. Both consider inertio-gravity waves using numerical techniques, but Philander's analysis covers a wider range of wavenumbers. On the other hand, by restricting our attention to a limited region near zero wavenumber, we have simplified the numerical integration and are able to treat in more detail the behavior of these waves in several different flow regimes. Regarding the Kelvin wave, we exploit the fact that typical mean flow speeds are much less than the phase speeds of low-order vertical modes in realistically stratified oceans. Using the small ratio of these speeds in a perturbation expansion, we obtain results similar to Philander's (1979) numerical results but in which both eastward and westward mean flows are considered. Philander in the same paper also considered the low-frequency Rossby waves in eastward flow, a subject not treated here.

In Section 2, we develop the model equations for a two-layer ocean with geostrophic mean currents in the upper layer. Section 3 describes the numerical solution of these for intermediate frequency inertio-gravity waves at and near zero wavenumber. The most striking result of this section is the enhanced variability of zonal velocity fluctuations in mean shear zones. In Section 4, we describe the perturbation expansion for the Kelvin wave which yields Doppler-shifted frequencies and nonzero meridional velocities proportional to a variety of flow parameters. Section 5 presents a discussion of the results of Sections 3 and 4.

2. Model ocean

We consider a two-layer, inviscid, Boussinesq ocean on an equatorial β -plane with no lateral boundaries. We use a caret (omitted) to denote the dimensional (nondimensional) form of a variable. In the upper layer of constant density flows a steady zonal current \bar{U} varying in latitude only and geostrophically balanced by \bar{D} , the thickness of the

MARCH 1979

M. J. McPHADEN AND R. A. KNOX

layer. The lower layer of density $\rho_1 > \rho_0$ is infinitely deep and therefore motionless. Using nondimensionalizations explained in (3)-(4) and linearizing about this background flow, the vertically integrated equations governing perturbations of the form $e^{ikx - \sigma t}$ are

$$-i\sigma u + R(ikUu + vU_y) - yv + ikp = 0, \quad (1a)$$

$$-i\sigma v + ikRUv + yu + p_y = 0, \quad (1b)$$

$$\frac{\lambda^2}{g'\bar{D}}(ikRU - i\sigma)p + ikDu + (Dn)_y = 0, \quad (1c)$$

where x is positive eastward, y positive northward and the reduced gravity $g' = g(1 - \rho_0/\rho_1)$. The set (u, v, p) gives the meridional dependence of zonal velocity, meridional velocity and pressure fluctuation, respectively. The background current \bar{U} and layer thickness \bar{D} are given by

$$\bar{D} = \bar{D}(y) = \bar{D}[D_0 + RD_1(y)], \quad D_1(-\infty) = 0, \quad (2a)$$

$$\left(\frac{\lambda^2}{g'\bar{D}}\right)yU(y) = -D_{1y}(y), \quad (2b)$$

where \bar{D} is the scale of upper layer thickness and D_0 is an $O(1)$ constant and accounts for small differences in average layer thickness between the several background flows to be studied. The nondimensionalizations and parameter definitions used to obtain (1)-(2) are

$$\left. \begin{aligned} (\hat{x}, \hat{y}) &= L(x, y), \quad \hat{k} = k/L, \quad L = (\beta/\lambda)^{-1/2} \\ \hat{t} &= tT, \quad \hat{\sigma} = \sigma T, \quad T = (\beta\lambda)^{-1/2} \\ \hat{U} &= U\bar{U}, \quad \hat{U} = \max|\hat{U}| \\ (\hat{u}, \hat{v}, (\rho_0\lambda)^{-1}\hat{p}) &= \mathcal{U}(u, v, p) \end{aligned} \right\} \quad (3)$$

The parameter λ appears in (1)-(3) as an artifact of the nondimensionalization, ensuring an inverse relation between length and time scales. In fact, it is the parameter which would have arisen as the separation constant or eigenvalue of the vertical problem had we not proceeded *ab initio* to the two-layer limit but retained a continuous system in the vertical. It becomes important to recognize the eigenvalue nature of λ in Section 4. There we treat the Kelvin wave by perturbation expansions, and as is usual in such problems it will be found necessary to allow perturbations to λ in order to avoid spurious resonances at first order driven by zeroth-order solutions. In this section and Section 3, where direct numerical calculations are used, we simply set $\lambda^2 = g'\bar{D}$ throughout.

The parameter \mathcal{U} is a scale for the perturbations and is essentially arbitrary, provided $\mathcal{U} \ll \bar{U}$, so that the basic linearization is valid. The remaining parameter in (1)-(3) is the Rossby number

$$R = \frac{\bar{U}}{\beta L^2} = \frac{\bar{U}}{\lambda} = \frac{\bar{U}}{(g'\bar{D})^{1/2}}, \quad (4)$$

which measures the ratio of background flow speed to the phase speed of internal gravity waves.

By setting $R = 0$, $D_0 = 1$ and $\lambda^2 = g'\bar{D}$, we obtain the well-known equations for perturbations about a state of rest:

$$v_{yy} + (\sigma^2 - k^2 - k/\sigma - y^2)v = 0, \quad (5a)$$

$$u = i(\sigma^2 - k^2)^{-1}(\sigma yv - kv_y), \quad (5b)$$

$$p = i(\sigma^2 - k^2)^{-1}(kyv - \sigma v_y). \quad (5c)$$

Solutions to (5), decaying as $|y| \rightarrow \infty$, exist for

$$\sigma^2 - k^2 - k/\sigma = 2n + 1, \quad n = 1, 2, \dots, \quad (6a)$$

with

$$v = \psi_n(y) = (\pi^{1/2} 2^n n!)^{-1/2} H_n(y) e^{-y^2/2}, \quad (7)$$

where $H_n(y)$ are Hermite polynomials. The high-frequency limit of (6a) yields inertio-gravity waves, whereas the low-frequency limit yields Rossby waves. Turning latitudes, where the solutions change from oscillatory to exponential behavior, are located at $y = \pm(2n + 1)^{1/2}$.

For $n = 0$ the only root of (6a) which gives a solution with bounded u and p fields at $y = \pm\infty$ is

$$k = \sigma - \frac{1}{\sigma}. \quad (6b)$$

This is the mixed Rossby-gravity or Yanai wave of Fig. 1 which for $\sigma \gg 1$ is gravity-like and $\sigma \ll 1$ is Rossby-like.

One more solution to (1) when $R = 0$ which is not contained in (5) is the Kelvin wave (designated $n = -1$ in Fig. 1), given by

$$v = 0, \quad (8a)$$

$$u = p = \psi_0, \quad (8b)$$

$$\sigma = k. \quad (8c)$$

The remainder of this paper deals with solutions to (1) when $R \neq 0$. We fix the parameters $\epsilon = 4 \times 10^{-3}$ and $\bar{D} = 200$ m so that the Rossby radius ($L = 360$ km), time scale ($T = 1.46$ days) and eigenvalue ($\lambda = 280$ cm s⁻¹) correspond closely to those of the first baroclinic mode in a realistically stratified ocean (Moore and Philander, 1977). We note that the choice of \bar{D} is a compromise. A 200 m upper layer coincides approximately with the depth range of the strongest mean currents. It also corresponds to the layer of greatest horizontal velocity amplitudes in the first baroclinic mode computed for a realistically stratified resting ocean (Wunsch, 1975; Philander, 1978b). However, the node of the first baroclinic mode thus computed lies at about 1200 m

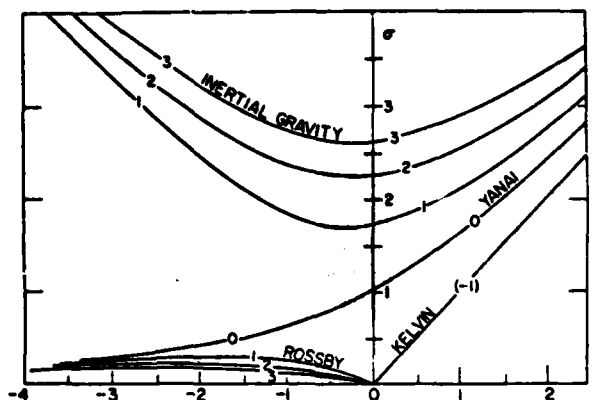


FIG. 1. Nondimensionalized dispersion diagram for equatorial β -plane waves. Stippled region is discussed in text. (After Wunsch and Gill, 1976.)

not 200 m and to this extent the two-layer model differs from the true vertical structure.

For the inertio-gravity waves treated numerically in the following section, the above choice of parameters requires that each of the different background states examined satisfies

$$\bar{D} = (1/2\hat{y}_0) \int_{-\hat{y}_0}^{\hat{y}_0} \bar{D} d\hat{y} = 200 \text{ m}, \quad (9)$$

with \bar{D}_0 in (2) determined from the integration constant. The range $(-\hat{y}_0, \hat{y}_0)$ is the range of significant wave amplitude, taken as $\pm 13^\circ$ of latitude. Since the Kelvin wave discussed in Section 4 is solved using perturbation expansions, we can standardize those results to the specified (ϵ, \bar{D}) by defining a convenient zeroth-order mean mixed layer depth.

3. Inertio-gravity waves

a. Method of solution

We set $\lambda^2 = g'\bar{D}$ and combine (1) to get expressions for v, u, p :

$$\begin{aligned} Dv_{yy} - 2yRUv_y - [k^2D - \hat{\sigma}^2 + y^2 + RU \\ + kD\hat{\sigma}^{-1}(1 - RU_{yy})]v + \hat{\sigma}^{-1}(k^2D - \hat{\sigma}^2)^{-1} \\ \times (2\hat{\sigma}kRU_y - k^2yRU)[kDv(y - RU_y) \\ - \hat{\sigma}(Dv_y - yvRU)] = 0, \quad (10a) \end{aligned}$$

$$\begin{aligned} u = i(k^2D - \hat{\sigma}^2)^{-1}[k(Dv_y - yvRU) \\ - \hat{\sigma}v(y - RU_y)], \quad (10b) \end{aligned}$$

$$\begin{aligned} p = i(k^2D - \hat{\sigma}^2)^{-1}[\hat{\sigma}(Dv_y - yvRU) \\ - kDv(y - RU_y)], \quad (10c) \\ \hat{\sigma} = \sigma - kRU(y). \end{aligned}$$

We restrict our attention to solutions of (10a) for the stippled region in Fig. 1 bounded by $|k| < 1.0$ and $0.7 < \sigma < 3.0$ (which dimensionally corresponds to wavelengths > 2500 km and periods between 3 and 13 days) in order to avoid singularities (i.e., critical layers) at $\sigma - kRU = 0$ and apparent singularities at $Dk^2 - (\sigma - kRU)^2 = 0$. This not only reduces the amount of computation needed to obtain v but guarantees all the wave solutions will be neutrally stable.

Eq. (10a) was integrated using a simple fourth-order Runge-Kutta routine by shooting for the eigenvalue σ given a choice of k . We used boundary conditions on v similar to those used by Philander (1976, 1978a, 1978b) and Hallock (1977), viz., $v = 0$ at $y = \pm\infty$, v, v_y continuous at $y = 0$. For symmetric U, D there is the added condition at $y = 0$ that v or v_y be zero depending on the mode under consideration. Integration proceeded from the poleward boundary to eliminate solutions to (10a) that grow as $|y| \rightarrow \infty$. To test the accuracy of this procedure, numerical solutions to (10) for $R = 0$ and step size $\Delta = 0.02$ were compared to the known analytic solutions of (5) given by (7). Table 1 shows that except near the boundaries $y = \pm 6$, one can expect four decimal place accuracy in both eigenvalues and eigenfunctions. This accuracy is assumed when (10) is integrated for $R \neq 0$.

b. Results

Eq. (1) was integrated for four geostrophic background states, three of which are given by

$$\begin{aligned} RU = 0.5e^{-2y^2}, \\ D = 0.99 + 0.083e^{-2y^2}, \quad R = 0.5, \quad (11a) \end{aligned}$$

MARCH 1979

M. J. MCPHADEN AND R. A. KNOX

TABLE 1. Accuracy of numerical solutions (subscript Δ) compared to analytic solutions for $k = 0$, step size $\Delta = 0.02$.

y	v_A	v	u_A	u	p_A	p
0.	-0.87259	-0.87258	0.	0.	0.93298×10^{-4}	0.
1.0	0.52922	0.52925	0.23668	0.23667	-0.70993	-0.71006
2.0	0.82665	0.82664	0.73940	0.73938	0.31675	0.31687
3.0	0.16479	0.16479	0.22110	0.22108	0.16909	0.16906
4.0	0.90750×10^{-2}	0.90743×10^{-2}	0.16234×10^{-1}	0.16232×10^{-1}	0.14147×10^{-1}	0.14138×10^{-1}
5.0	0.15934×10^{-2}	0.15933×10^{-2}	0.35631×10^{-2}	0.35627×10^{-2}	0.32765×10^{-2}	0.32720×10^{-2}
5.9	0.96765×10^{-4}	0.16533×10^{-3}	0.25532×10^{-3}	0.43624×10^{-3}	0.57629×10^{-3}	0.41081×10^{-3}
			$\sigma_A^2 = 4.9997$	$\sigma^2 = 5.0000$		

$$RU = -0.5e^{-3y^2},$$

$$D = 1.01 - 0.083e^{-3y^2}, \quad R = 0.5, \quad (11b)$$

$$RU = -ye^{-y^2},$$

$$D = 0.56 - 0.5 \left[ye^{-y^2} - \int_{-\infty}^y e^{-t^2} dt \right],$$

$$R = 0.43. \quad (11c)$$

The flows of (11a) and (11b) are symmetric eastward and westward jets, respectively, with maximum speeds of 140 cm s^{-1} on the equator and half-width of approximately 1.5° . The flow in (11c) is an antisymmetric jet with maximum speed of 120 cm s^{-1} at $\pm 2.3^\circ$. In each case the mixed-layer depth is specified by (2) and (9) with $y_0 = 4$ (dimensional latitude $= 13^\circ$). These three background states are illustrated in Fig. 2. Note in particular the very deep mixed layer to the north associated with the antisymmetric jet (11c).

Also, we integrated (10) for a fourth, less-idealized background state, derived from a temperature section typical of average conditions in the upper layers of the central Pacific [Fig. 3 (after Wyrtki *et al.*, 1977)]. We chose the interface between the constant density layers of the model to be the 20°C isotherm which is centrally located in the equatorial pycnocline; a constant of 40 m was added to the mean depth as determined by the isotherm so as to satisfy $\bar{D} = 200 \text{ m}$. Assuming that geostrophy holds to within $\pm 0.5^\circ$ of the equator, we calculated a current system in balance with this interface by cubic spline interpolation of $(-D_{1y}/y)$. The latitudinal distribution (Fig. 3, dashed line) and mass transport of the interpolated zonal currents are in agreement with observations. For example, the model undercurrent transport of $\sim 30 \times 10^6 \text{ m}^3 \text{ s}^{-1}$ compares favorably with Knauss' (1966) values. The Rossby number for this case is ~ 0.25 . Choosing other isotherms in the thermocline to define the model interface does not significantly change this Pacific profile.

In Section 3b1 we consider solutions to (10) when $k = 0$ for the background states (11) and for the Pacific profile of Fig. 3. Next we discuss solutions to (10) for small but nonzero wavenumbers in Sec-

tion 3b2. The dispersion of inertio-gravity waves in all four mean fields is analyzed in Section 3b3.

1) MERIDIONAL STRUCTURE: $k = 0$

When $k = 0$, Eq. (10) becomes

$$Dv_{yy} - 2yRUv_y + (\sigma^2 - y^2 - RU)v = 0, \quad (12a)$$

$$u = i\sigma^{-1}(y - RU_y)v, \quad (12b)$$

$$p = -i\sigma^{-1}(Dv)_y. \quad (12c)$$

Figs. 4–6 show solutions to (12) in selected background flows superimposed on solutions corresponding to $R = 0$ (dashed lines); the background currents themselves are plotted for reference (dotted lines). All solutions have been arbitrarily scaled so that the maximum meridional velocity is 1.

Fig. 4 is a plot of solutions to (12) for the eastward jet (11a). The effects of this mean current on v and p are minimal because terms involving R are relatively small in (12a) and (12c). On the other hand, the zonal perturbation velocity exhibits large anomalies in the region of strong mean shear, which from (12b) is clearly due to meridional advection of the mean current. The net result is a sinuous (v even) or varicose (v odd) meander of the background flow. Similar meanders associated with the mixed Rossby-

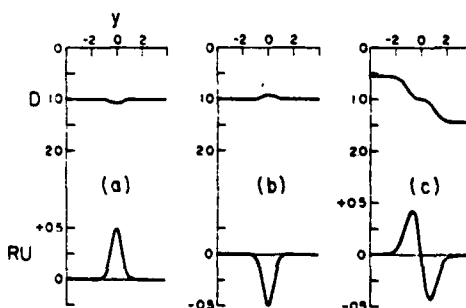


FIG. 2. Profiles of upper layer thickness and associated zonal current for three of the background flow regimes studied: (a) is the symmetric eastward jet, (b) the symmetric westward jet and (c) the antisymmetric jet.

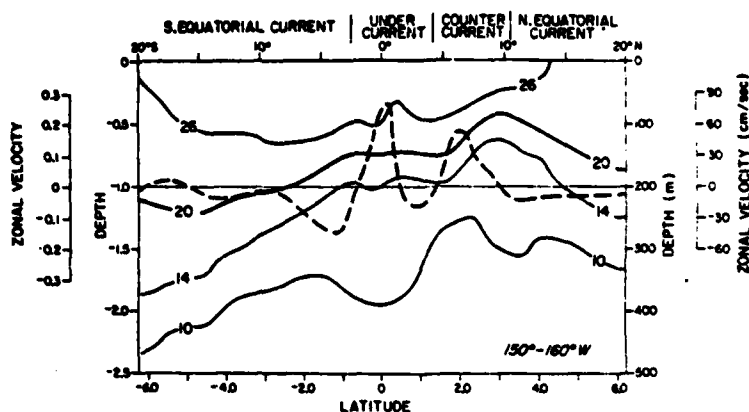


FIG. 3. Temperature section from the Central Pacific. The 20° isotherm (heavy solid line) defines the interface topography and current structure (dashed line) of the Pacific profile discussed in text.

gravity wave were the dominant motions in Hallock's (1977) wind-driven model, but at slightly higher wavenumber and lower frequency. Note that the eigenvalues σ^2 of (12a) are no longer simple in-

teger constants $(2n + 1)$ predicted by (6), but are fractionally larger (Table 2). Nonetheless, solutions to (10) and (12) will still be designated by $n = 0, 1, 2$. Not shown are solutions to (12) for the westward

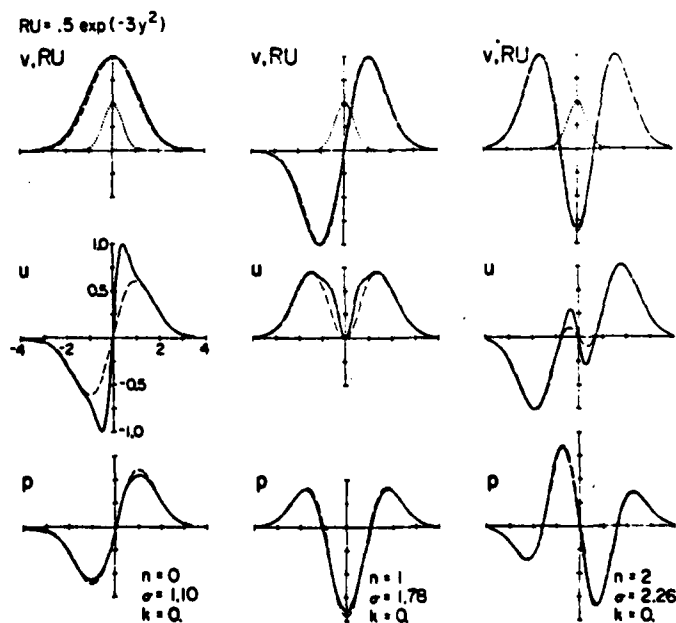


FIG. 4. Comparisons of wave fields with and without background flow (in this instance the eastward jet), for $k = 0$. Meridional modes, 0, 1, 2 are illustrated. Dashed (solid) line shows the wave amplitude without (with) background flow. The background current itself is indicated by the additional dotted curve.

MARCH 1979

M. J. McPHADEN AND R. A. KNOX

TABLE 2. The effects of mean zonal flow on frequency at zero wavenumber. The percent of change in frequency is defined as $100[(\sigma/\sigma_{n=0}) - 1]$.

Mean flow	Mode n	Eigenvalue σ^2	Frequency σ	Period (days)	Percent change in frequency
No current	0	1.00	1.00	9.17	—
	1	3.00	1.73	5.30	—
	2	5.00	2.23	4.11	—
Eastward jet	0	1.22	1.10	8.34	10
	1	3.16	1.78	5.15	3
	2	5.10	2.26	4.06	1
Westward jet	0	0.77	0.88	10.42	-12
	1	2.82	1.68	5.46	-3
	2	4.88	2.21	4.15	-1
Antisymmetric jet	0	1.00	1.00	9.17	0
	1	3.02	1.74	5.27	1
	2	4.93	2.22	4.13	0
Pacific profile	0	1.14	1.07	8.57	7
	1	3.17	1.78	5.15	3
	2	5.29	2.30	3.99	3

jet (11b) since changing the sign of RU essentially changes the sign of the structural and frequency anomalies observed in Fig. 4.

The antisymmetric jet (11c) produces more dra-

matic alteration of the eigensolutions to (12), as shown in Fig. 5. With increasing n , perturbation velocities weaken in the hemisphere of deepest mixed layer, especially near the turning latitude

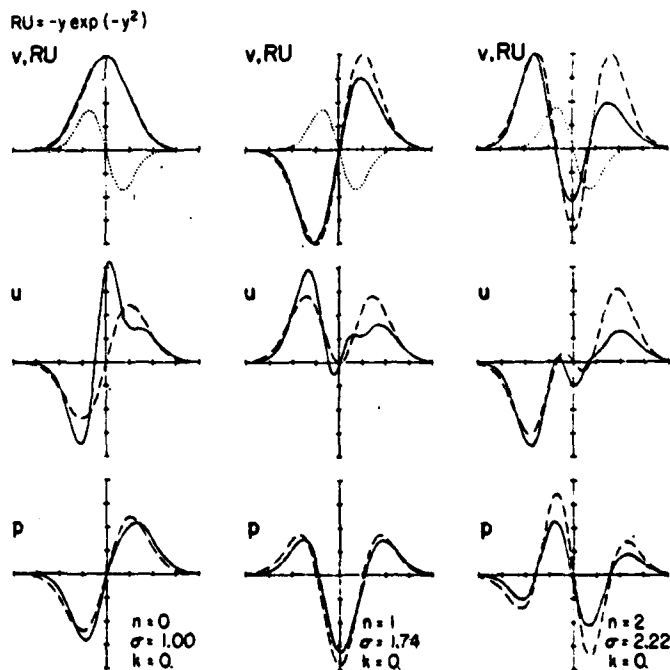


FIG. 5. As in Fig. 4 except with antisymmetric jet as background flow.

(equal to the inertial latitude when $k = 0$) located at $y \sim (2n + 1)^{1/2}$. Meridional advection of the mean flow distorts the zonal perturbation velocities even more, particularly that of the mixed Rossby-gravity wave which at the equator shows a near maximum instead of a node. Boyd (1978) reports a similar feature associated with long, atmospheric mixed mode waves in weakly sheared mean winds having an antisymmetric component. Pressure fluctuations are weaker relative to their strength when no mean currents are present, but their meridional structures are otherwise little changed.

Results for the Pacific profile are shown in Fig. 6. As in the case of the antisymmetric jet, strong mean shear right on the equator results in large zonal velocity fluctuations in the $n = 0$ mode. However, since the background flow between the turning latitudes is largely symmetric, there is little trend toward consistently higher velocities in one hemisphere relative to the other; it is expected that such trends would appear in higher meridional modes whose turning latitudes are farther from the equator. Other effects due to the presence of mean flow include the small-scale variability introduced into the latitudinal structure of u , which corresponds to similar small-scale variability in the mean shear pro-

file. Pressures are again relatively insensitive to the background state.

Since there are no critical layers in the flow fields described above, perturbation energy density averaged over one wave period must be independent of time, i.e.,

$$E = E(y) = K(y) + V(y), \quad (13a)$$

$$K(y) = \frac{1}{2} D(\bar{u}^2 + \bar{v}^2), \quad (13b)$$

$$V(y) = \frac{1}{2} \bar{p}^2, \quad (13c)$$

where E is the total energy density, K the kinetic energy density and V the potential energy density. The overbar denotes time average. Furthermore, when the background state is a symmetric function of latitude, so must E , K and V be symmetric. This does not hold in the case of the antisymmetric jet (11c) or the Pacific profile. For example, plots of K and V versus latitude for the modes $n = 0, 1, 2$ when the mean state is defined by (11c) show, as expected, that kinetic energy density is amplified in the hemisphere of shallow mixed layer (Fig. 7). The most significant asymmetry appears near the turning latitudes except in the $n = 0$ mode which is complicated by large zonal perturbation velocities near the equator. The dashed curves in Fig. 7 that

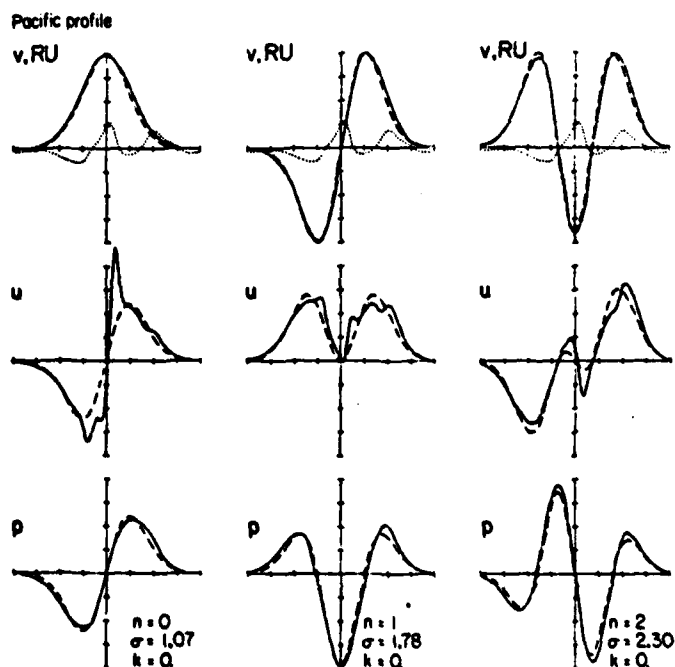


FIG. 6. As in Fig. 4 except with Pacific profile as background flow.

MARCH 1979

M. J. MCPHADEN AND R. A. KNOX

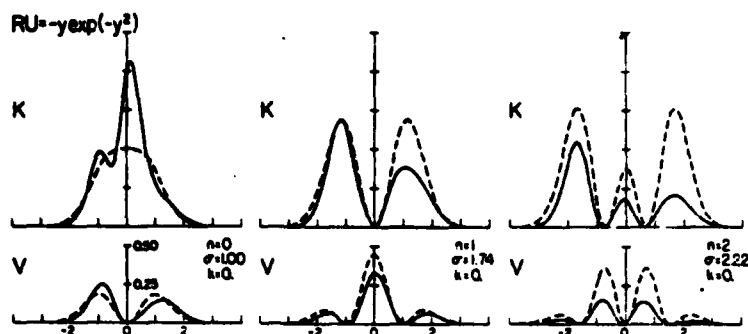


FIG. 7. Kinetic (K) and potential (V) energy densities as functions of latitude, both with (solid line) and without (dashed line) background flow, for the same modes as Fig. 5. The background flow is the antisymmetric jet.

correspond to K for a mean state of rest display none of these features. Conversely, potential energy density is similar to that in the absence of mean currents. (The large discrepancy in total energy levels which appears in Fig. 7c is not significant because we have arbitrarily scaled the amplitude of the solutions according to $v_{max} = 1$ for each individual wave.)

2) MERIDIONAL STRUCTURE: $|k| < 1$

Solutions to (10) at small but non-zero wavenumbers show the same basic wave-mean flow interactions discussed above. Specifically, in regions where mean shear is large, zonal perturbation velocities are stronger; where the background fields are not symmetric between turning latitudes, kinetic energy density favors the hemisphere of shallow mixed layer; perturbation pressures and meridional velocities are typically less affected except for an amplitude factor. Because of the similarity of these results with zero wavenumber solutions, we do not present them graphically.

3) DISPERSION

Fig. 8 compares the dispersion curves for selected modes with and without background flow. In Fig. 8a there is an increase in eastward and decrease in westward group velocity due to the eastward jet (11a); the opposite is true for the westward jet (11b) as shown in Fig. 8b. These Doppler shifts are similar to those calculated for meridionally uniform flows of the same intensity (dashed curves) but are much less pronounced because of the narrowness of (11a) and (11b). In addition to these Doppler shifts there is also a small frequency offset which is toward higher values in the eastward and lower values in the westward flows (Table 2). Frequency shifts

caused by the antisymmetric jet (11c) are not evident (Fig. 8c) because the net transport across any meridian is identically zero.

In the Pacific profile which has both symmetric (Equatorial Undercurrent) and antisymmetric (South Equatorial Current-North Equatorial Countercurrent) components of the mean flow, Doppler shifts are virtually absent. This is because the symmetric component is weaker than the eastward jet of (11a) by a factor of 2 and because the antisymmetric component is inefficient at producing net advection of the wave fields as was seen for the jet (11c). There is however a small frequency offset in Fig. 8d similar to that observed for the eastward jet. Note that the point of zero group velocity for $n = 1$ and 2 modes in the Pacific flow field, as well as in the more idealized fields of Fig. 2, is always near zero wavenumber.

4. The Kelvin wave

a. Method of solution

A perturbation scheme is developed that exploits the smallness of R and the simple expressions for the Kelvin wave in an ocean at rest given in (8). We first expand

$$u = u_0 + Ru_1 + R^2u_2 + \dots, \quad (14a)$$

$$v = v_0 + Rv_1 + R^2v_2 + \dots, \quad (14b)$$

$$p = p_0 + Rp_1 + R^2p_2 + \dots, \quad (14c)$$

$$\sigma = \sigma_0 + R\sigma_1 + R^2\sigma_2 + \dots, \quad (14d)$$

In addition we expand λ^2 for reasons noted in Section 2,

$$\lambda^2 = \lambda_0^2 + R\lambda_1^2 + R^2\lambda_2^2 + \dots; \quad \lambda_0^2 = g'DD_0. \quad (14e)$$

When substituted into (1), one finds to zeroth order in the Rossby number the Kelvin wave of (8),

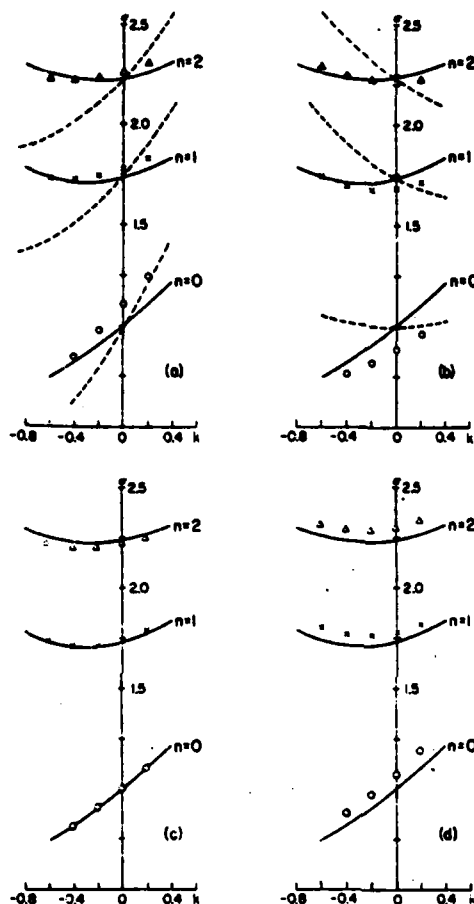


FIG. 8. Dispersion curves for the modes $n = 0, 1, 2$, at small wavenumber and in the presence of the eastward jet (a) the westward jet (b) the antisymmetric jet (c) and the Pacific profile (d). Solid lines give dispersion curves for no background flow, plotted symbols define curves with background flow. In (a) and (b) additional dashed curves show dispersion relation which would result from longitudinally uniform background flow with velocity equal to jet maximum velocity.

viz., $u_0 = p_0 = \psi_0$, $\sigma_0 = k$. Since $v_0 = 0$ the first-order equations are

$$-i\sigma_0 u_1 - y v_1 + i k p_1 = -i k U u_0 + i \sigma_1 u_0, \quad (15a)$$

$$-i\sigma_0 v_1 + y u_1 + p_{1y} = 0, \quad (15b)$$

$$-i\sigma_0 p_1 + i k u_1 + v_{1y} = i \left(\sigma_1 + \frac{\sigma_0 \lambda_1^2}{g' D_0} - k U \right) p_0 - i k \left(\frac{D_1}{D_0} \right) u_0. \quad (15c)$$

The right side of (15) can be written in terms of Hermite functions by projecting $U u_0 = U p_0 = U \psi_0$ and $D_1 u_0 = D_1 \psi_0$ onto the set $\{\psi_n\}$:

$$D_1 \psi_0 = D_0 \sum_{n=0}^{\infty} d_n \psi_n,$$

$$d_n = D_0^{-1} \int_{-\infty}^{\infty} D_1 \psi_0 \psi_n dy, \quad (16a)$$

$$U \psi_0 = \sum_{n=0}^{\infty} f_n \psi_n, \quad f_n = \int_{-\infty}^{\infty} U \psi_0 \psi_n dy. \quad (16b)$$

Since each ψ_n on the right side of (15) will excite a different response, it is convenient to further decompose the O(R) problem into the series

$$u_1 = u_{10} + \sum_{n=1}^{\infty} u_{1n}, \quad (17a)$$

$$v_1 = v_{10} + \sum_{n=1}^{\infty} v_{1n}, \quad (17b)$$

$$p_1 = p_{10} + \sum_{n=1}^{\infty} p_{1n}. \quad (17c)$$

The first term in these expressions deserves special attention because ψ_0 forcing will drive a resonant first-order Kelvin wave with $v_{10} = 0$, $u_{10} = p_{10} = \psi_0$. In order to remove this spurious resonance, one must insist that no ψ_0 terms appear in the forcing. This is accomplished by imposing the constraints

$$\sigma_1 = f_0 k, \quad (18a)$$

$$\lambda_1^2 = d_0 g' D_0. \quad (18b)$$

The first of these results is a Doppler shift proportional to the wavenumber k , the Rossby number R , and the width and direction of the background flow through f_0 . The second adjusts λ , the eigenvalue of the vertical problem underlying our two-layer limiting case. The part of the first-order solution proportional to ψ_0 (zeroth order Kelvin wave) is now of arbitrary amplitude which can be set to zero without loss of generality. For other $n \geq 1$, the equations

$$-i\sigma_0 u_{1n} - y v_{1n} + i k p_{1n} = -i k f_n \psi_n, \quad (19a)$$

$$-i\sigma_0 v_{1n} + y u_{1n} + p_{1ny} = 0, \quad (19b)$$

$$-i\sigma_0 p_{1n} + i k u_{1n} + v_{1ny} = -i k (f_n + d_n) \psi_n, \quad (19c)$$

can be solved by eliminating u_{1n} and p_{1n} in favor of v_{1n} to get

$$v_{1nyy} + (\sigma_0^2 - k^2 - k/\sigma_0 - y^2) v_{1n} = -2ik(f_n + \frac{1}{2} d_n) \psi_n + y \psi_n. \quad (20)$$

Making use of the identities $\sigma_0 = k$ and

$$\psi_{-1} = 0, \quad (21a)$$

$$\psi_{ny} = -\left(\frac{n+1}{2}\right)^{1/2} \psi_{n+1} + \left(\frac{n}{2}\right)^{1/2} \psi_{n-1}, \quad (21b)$$

MARCH 1979

M. J. MCPHADEN AND R. A. KNOX

$$\psi_n = \left(\frac{n+1}{2}\right)^{1/2} \psi_{n+1} + \left(\frac{n}{2}\right)^{1/2} \psi_{n-1}, \quad (21c)$$

it is readily determined that, for $n \geq 1$,

$$v_{1n} = ikc_n \psi_{n-1}, \quad c_n = (2/n)^{1/2} (f_n + \frac{1}{2} d_n). \quad (22a)$$

The usual method of obtaining expressions for u and p from v by combining continuity with the zonal momentum equation fails here because $\sigma_n = k$. But from (19b) and (19c) one finds

$$u_{1n} = q_n \psi_{n+2} + r_n \psi_n + s_n \psi_{n-2}, \quad (22b)$$

$$p_{1n} = q_n \psi_{n+2} + (r_n + \frac{1}{2} d_n) \psi_n - s_n \psi_{n-2}, \quad (22c)$$

where

$$q_n = \frac{1}{4} d_n \left(\frac{n+1}{n+2}\right)^{1/2}, \quad (23a)$$

$$r_n = (f_n + \frac{1}{2} d_n) \left(\frac{n-1-2\sigma_n^2}{2n}\right) - \frac{1}{4} d_n, \quad (23b)$$

$$s_n = -\frac{1}{2} (f_n + \frac{1}{2} d_n) \left(\frac{n-1}{n}\right)^{1/2}. \quad (23c)$$

Thus to $O(R^2)$ we have

$$u = e^{ikx - \sigma t} \left\{ \psi_0 + R \sum_{n=1}^{\infty} [q_{n-2} + r_n + s_{n+2}] \psi_n \right\}, \quad (24a)$$

$$v = iRk e^{ikx - \sigma t} \sum_{n=1}^{\infty} c_n \psi_{n-1}, \quad (24b)$$

$$p = e^{ikx - \sigma t} \left\{ \psi_0 + R \sum_{n=1}^{\infty} [q_{n-2} + r_n + \frac{1}{2} d_n - s_{n+2}] \psi_n \right\}, \quad (24c)$$

$$\sigma = \sigma_0 (1 + R f_0), \quad (24d)$$

$$\lambda^2 = g' D_0 (D_0 + R d_0), \quad (24e)$$

with $q_{-1} = q_0 = 0$. In order to standardize results for various cases we will fix λ^2 for a given ϵ as discussed in Section 2. This requires simply that the zeroth-order mixed-layer depth be defined by

$$D_0 = 1 - R d_0$$

which is a function of U through d_0 .

b. Results

Solutions to (24) were computed in the presence of mean jets of the form

$$RU = \pm R e^{-\alpha y}, \quad \alpha > 0, \quad (25a)$$

for which the coefficients (f_n, d_n) readily can be calculated as shown in the Appendix. The upper layer thickness associated with this flow is

$$D = 1 \pm (R/2\alpha) e^{-\alpha y}. \quad (25b)$$

Solutions to (24) for one sign of (25) determine solu-

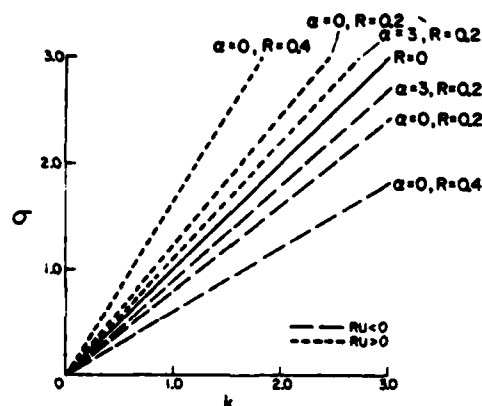


FIG. 9. Dispersion curves for the Kelvin wave in the presence of various mean flows specified by (R, α) . Solid line ($R = 0$) corresponds to the Kelvin wave in the absence of mean currents.

tions for the opposite sign since reversing the direction of the mean flow simply changes the sign of all the first-order fields. Thus, only one set of calculations needs to be done for eastward and westward flows of the same width and intensity.

1) DISPERSION

From (16b), (24b) and (25a), the frequency shift is

$$R\sigma_1 = Rf_0 k = \pm Rk(\alpha + 1)^{-1/2}. \quad (26)$$

The magnitude of this Doppler shift is greatest in broad (small α) mean flows and as expected, higher (lower) frequencies result from eastward (westward) flows. In the inertio-gravity range (Fig. 8) similar tendencies exist but are more subdued because the phase speeds of those waves are much larger relative to the mean currents.

The limit $\alpha = 0$ (uniform flow) is instructive, if we relax the geostrophic constraint (2b) and simply set $D_0 = 1$. In this case we obtain

$$\sigma_1 = \pm k,$$

so that the total solution is just the zeroth-order Kelvin wave (8) with frequency $\sigma_0(1 \pm R)$. All terms with summations over n in (24a)–(24c) vanish in this (somewhat artificial) limit, as can be seen from definitions (16a) and (16b).

The dispersion of free Kelvin waves in a variety of mean flows is shown in Fig. 9. To the approximation (24) all the waves remain nondispersive with frequency depending on the width and intensity of the mean flow as well as the Kelvin wavenumber. Moreover, as is clear from (26), to each of these curves there corresponds a family of overlapping

curves, e.g., the curve ($\alpha = 3, R = 0.2$) corresponds to curves for ($\alpha = 8, R = 0.3$), ($\alpha = 0, R = 0.1$), etc. It is noteworthy that the dispersion plot for any antisymmetric jet coincides with the line $R = 0$ since $f_0 = 0$ by (16b); as in the case of inertio-gravity waves discussed above, antisymmetric flows do not Doppler shift the wave fields. Observe also that this figure for $RU > 0$ is similar to Fig. 1 of Philander (1979) which shows the numerically determined dispersion of Kelvin waves in similar eastward flows.

2) MERIDIONAL STRUCTURES

We truncated the summations (24) at $n = 40$ (20 nonvanishing terms, due to symmetry); this is a very accurate representation except for exceedingly narrow ($\alpha \gg 5$) jets. Figs. 10–12 show the resultant modifications to Kelvin waves of various frequencies in eastward and westward jets of various widths. In Fig. 10, a long wave interacts with a narrow jet. The first-order fields u_1 , v_1 , and p_1 take the form of low-frequency Rossby waves, i.e., u_1 and p_1 are nearly in geostrophic balance. The total fields in Figs. 10b and 10c are nearly the same as their $R = 0$ counterparts except for the zonal velocity component near the equator. The frequency is 10% higher (lower) than $\sigma_0 = k$ in the eastward (westward) jet.

Broader mean flow will have even less effect on

the meridional structures of the Kelvin wave in this region of dispersion space. As shown in Fig. 11 for jets nine times wider than those of Fig. 10, the first-order fields are much weaker and the total fields are virtually indistinguishable from the zeroth-order curves. On the other hand, the frequencies are shifted more for this mean flow in accordance with (24d).

For frequencies that fall within the inertio-gravity range $\sigma > 1$, the first-order corrections change character dramatically. First, from (22a) the meridional velocity is a linear function of wavenumber and hence frequency so that this component is much larger than at lower frequency. Second, the corrections forced by the zeroth-order solutions are distinctly gravity-like because of the nearness of those waves to the Kelvin dispersion curve at higher frequency (Fig. 1). Both these effects are seen in Fig. 12: v_1 is about 10 times larger than that in Fig. 10 for a low-frequency wave and the components of the first-order field look very much like those associated with an $n = 1$ gravity mode. When combined with the zeroth-order solution, these forced corrections produce a much different picture of the Kelvin wave in both eastward and westward shear flow. We note that Philander's (1979, Fig. 1) numerical result for an 800 km, 3.3-day wave in narrow eastward shear flow ($R \sim 0.28$) is very similar to that

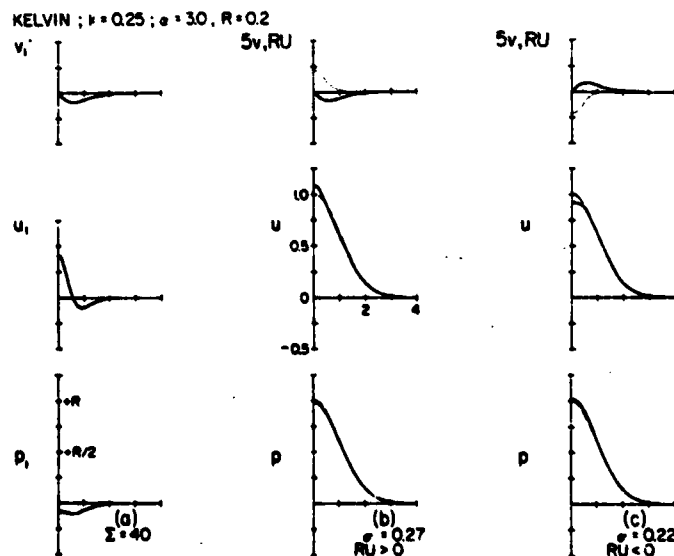


FIG. 10. Meridional structure of a low-frequency, long wavelength Kelvin wave in narrow shear flow [dotted curves in (b) and (c)]. First-order corrections are shown in (a). Solid curves in (b) and (c) are the total fields in the presence of the indicated mean flow; dashed curves are the Kelvin wave in the absence of mean flow.

MARCH 1979

M. J. McPHADEN AND R. A. KNOX

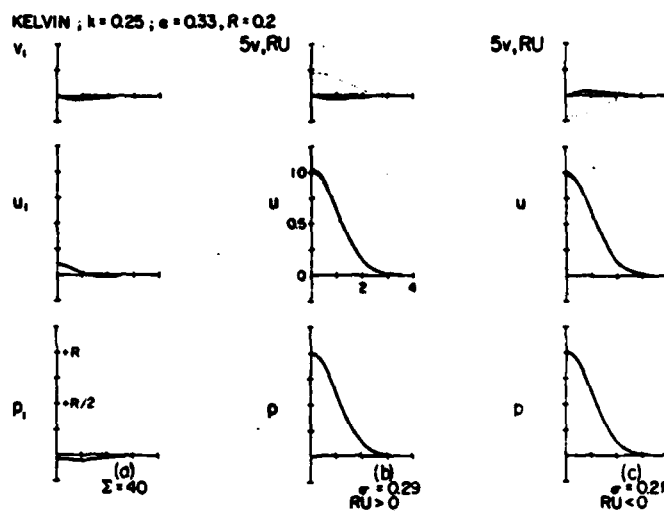


FIG. 11. As in Fig. 10 but for the broad mean flows shown in (b) and (c).

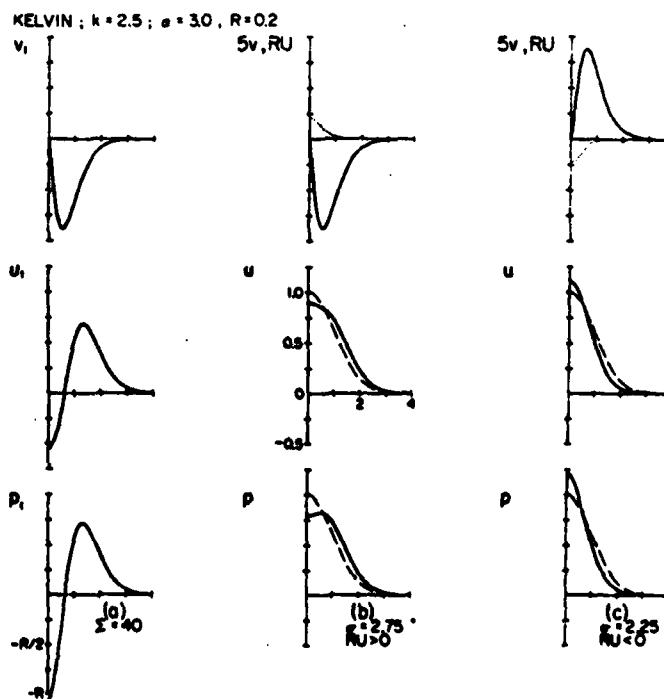


FIG. 12. As in Fig. 10 but for a high-frequency short-wavelength Kelvin wave.

observed in Fig. 12b which is for a 900 km, 3.3-day wave.

5. Discussion

The foregoing analysis has shown that meridional velocity fluctuations associated with neutrally stable inertio-gravity waves advect the mean currents so as to produce intermediate-frequency meanders. The strongest of these, associated with the mixed Rossby-gravity wave, are similar to those observed during Phase II of GATE. Likewise, Titov (1977) reports on meanders of the Cromwell Current between 2.5°N and 2.5°S along 166.5°E in the Pacific. Over a two-week period in March 1972, the maximum speed of the mean current migrated about the equator with a period of O(10 days), lagging (leading) the meridional velocity by about a quarter cycle north (south) of the equator. These phase relationships and symmetry characteristics suggest a mixed Rossby-gravity wave interpretation like that used to describe the GATE meanders. It is noteworthy that these two sets of current measurements (the most comprehensive to date at low latitudes) display the same type of meandering behavior, for it suggests that such meanders are commonplace. However, the coincidence may be fortuitous. Indeed, the mixed Rossby-gravity wave is the gravest antisymmetric equatorial mode and should be strongly excited by large-scale meridional or antisymmetric zonal winds. Unlike the higher order inertio-gravity waves, though, there is no preferred response to wide band forcing at intermediate frequencies, implying that winds with highly structured spectra must have generated the observed meanders. Since such spectra are atypical, one might alternately conclude that these data were collected during periods of anomalous wind forcing.

Peaks in velocity spectra associated with inertio-gravity waves other than the mixed Rossby-gravity wave will be sharper in the hemisphere of the shallowest mixed layer when the depth increases significantly between the turning latitudes. Conversely, irrespective of the pycnocline topography, sea level spectra will be little different from those predicted by theories without background flow. This may have facilitated the work of Wunsch and Gill (1976) in modeling 4-day and 5-day sea level variability as the surface manifestation of baroclinic inertio-gravity waves; their theory included no mean currents, yet the fit of observed to predicted sea level amplitude distributions was good.

Because the time scale T of (3) is proportional to the fourth root of the stratification parameters (σ, D), a moderately accurate determination of the mean density field fixes T and hence the frequency rather precisely for vertically standing modes at a

given zonal wavenumber. It should then be possible to ascribe significance to relatively small departures of observed frequencies from $R = 0$ values and to interpret such shifts in terms of mean currents. For example, Wunsch and Gill (1976) found in their Pacific sea level study that inertio-gravity wave frequencies predicted using an equatorial β -plane model without background flow led to frequencies that were uniformly too low by about 10% compared to the observations. Although there is a large uncertainty in their calculations (time scales were computed using a single density profile), the observed discrepancy is consistent with the 3–7% higher frequencies expected for inertio-gravity waves in the Pacific profile (Fig. 8d).

The low-frequency Kelvin wave solutions of Section 4 are very similar structurally to Kelvin waves in an ocean at rest except for their higher or lower phase/group velocities. This change in propagation speed can be large in strong unidirectional currents and thus may affect significantly the baroclinic adjustment times in the tropics. With increasing frequency, the meridional velocity of the Kelvin waves increases in the presence of mean flow and they become more gravity-like. If not directly wind forced, these waves could be excited by gravity modes in western boundary regions and propagate into the open ocean as varicose meanders of the mean currents. Their energy contribution to sea level and velocity fluctuations may be comparable to that of gravity waves in the same frequency band, but separating these two types of motion requires wavenumber spectra as well as frequency spectra; at present such data are lacking.

The basic simplification of the foregoing analysis is the two-layer model with its single baroclinic mode. Unfortunately, there are large regions of dispersion space where a single vertical mode poorly describes the field of motion (Philander, 1978b). For realistic stratification, this occurs when the forcing is confined to a thin surface layer and when its frequency and wavenumber are such that a large number of vertical modes are excited nonresonantly. Under these conditions, the ocean's response is better described as a sum of vertically propagating horizontal modes as demonstrated in Wunsch (1977b) for periodic monsoon forcing. It is important to know how these vertically propagating modes interact with mean currents near the surface, a problem that is the natural complement to the one considered in this paper.

Acknowledgment. We are grateful for the support of the Office of Naval Research under Contract N00014-75-C-0152/Knox to the University of California, Scripps Institution of Oceanography.

MARCH 1979

M. J. McPHADEN AND R. A. KNOX

APPENDIX

Calculation of the Coefficients (f_n, d_n)

We wish to evaluate the expression

$$f_n = \int_{-\infty}^{\infty} U \psi_n dy, \quad U = e^{-\alpha y^2}. \quad (A1)$$

Now since

$$H_n(y) = \sum_{j=0}^n (-1)^j \frac{n!(2y)^{n-2j}}{(n-2j)!j!},$$

$$N = \begin{cases} n/2, & n \text{ even} \\ (n-1)/2, & n \text{ odd}, \end{cases} \quad (A2)$$

the integral (A1) becomes

$$f_n = (\pi n! 2^n)^{-1/2} \sum_{j=0}^N (-1)^j \times \int_{-\infty}^{\infty} e^{-\alpha y^2} \left[\frac{n!(2y)^{n-2j}}{(n-2j)!j!} \right] dy. \quad (A3)$$

The j th term in (A3) can be expressed as

$$(-1)^j \frac{n! 2^{n-2j}}{(n-2j)!j!} \int_0^{\infty} y^{n-2j} e^{-(\alpha+1)y^2} dy$$

$$= (-1)^j \left[\frac{n! 2^{n-2j}}{(n-2j)!j!} \right] \frac{\Gamma[(n-2j+1)/2]}{(\alpha+1)^{n-2j+1/2}},$$

where

$$\Gamma(m + 1/2) = \begin{cases} \pi^{1/2}, & m = 0 \\ \frac{(2m-1)!!}{2^m} \pi^{1/2}, & m > 0. \end{cases}$$

Thus,

$$f_n = (\pi n! 2^n)^{-1/2} \sum_{j=0}^N (-1)^j \times \left[\frac{n! 2^{n-2j}}{(n-2j)!j!} \right] \frac{\Gamma[(n-2j+1)/2]}{(\alpha+1)^{n-2j+1/2}}. \quad (A4)$$

When $D_1 = (1/2\alpha)U$, as in (25),

$$d_n = (1/2\alpha)f_n. \quad (A5)$$

REFERENCES

- Adamec, D. and J. J. O'Brien, 1978: The seasonal upwelling in the Gulf of Guinea due to remote forcing. *J. Phys. Oceanogr.*, 8, 1050-1060.
- Blandford, R., 1966: Mixed gravity-Rossby waves in the ocean. *Deep-Sea Res.*, 13, 941-961.
- Boyd, J. P., 1978: The effects of latitudinal shear on equatorial waves. Part 1: Theory and methods. *J. Atmos. Sci.*, 35, 2236-2258.
- Ding, W., P. Hisard, E. Katz, J. Krauss, J. Meincke, L. Miller, K. Moroshkin, G. Philander, A. Rybnikov, K. Voigt and R. Weisberg, 1975: Meanders and long waves in the equatorial Atlantic. *Nature*, 257, 280-284.
- Hallock, Z., 1977: Wind forced equatorial waves in the Atlantic Ocean. Ph.D. thesis, University of Miami, 152 pp.
- Hurlburt, H. E., J. C. Kindle and J. J. O'Brien, 1976: A numerical simulation of the onset of El Nino. *J. Phys. Oceanogr.*, 6, 621-631.
- Krauss, J. A., 1966: Further measurements and observations of the Cromwell Current. *J. Mar. Res.*, 24, 205-240.
- Matsumo, T., 1966: Quasi-geostrophic motions in the equatorial area. *J. Meteor. Soc. Japan*, 44, 25-43.
- McCreary, J., 1976: Eastern tropical response to changing wind systems: with application to El Nino. *J. Phys. Oceanogr.*, 6, 623-645.
- Moore, D., 1968: Planetary-gravity waves in an equatorial ocean. Ph.D. thesis, Harvard University, 201 pp.
- , and S. G. H. Philander, 1977: Modelling the tropical ocean circulation. *The Sea*, Vol. 6, Interscience, 319-361.
- , P. Hisard, J. McCreary, J. Merle, J. J. O'Brien, J. Picaut, J. Verstraete and C. Wunsch, 1978: Equatorial adjustment in the Eastern Atlantic. *Geophys. Res. Lett.*, 5, 637-640.
- Philander, S. G. H., 1975: Instabilities of zonal equatorial currents. *J. Geophys. Res.*, 81, 3725-3735.
- , 1978a: Instabilities of zonal equatorial currents. 2. *J. Geophys. Res.*, 83, 3679-3682.
- , 1978b: Forced oceanic waves. *Rev. Geophys. Space Phys.*, 16, 15-46.
- , 1979: Equatorial waves in the presence of the Equatorial Undercurrent. *J. Phys. Oceanogr.*, 9, 254-262.
- Titov, V. B., 1977: Meandering of the Cromwell Current. *Oceanology*, 17, 271-273.
- Wunsch, C., 1975: Notes for equatorial array work. (Unpublished manuscript).
- , 1977a: Observations of equatorially trapped waves in the ocean. (Unpublished manuscript).
- , 1977b: Response of an equatorial ocean to a periodic monsoon. *J. Phys. Oceanogr.*, 7, 497-511.
- , and A. Gill, 1976: Observations of equatorially trapped waves in sea level variations. *Deep-Sea Res.*, 23, 371-391.
- Wyrtki, K., G. Meyers and W. Patzert, 1977: Variability of the thermal structure in the central equatorial Pacific Ocean. Tech. Rep. HIG-77-1, Hawaii Inst. Geophys., 75 pp.

REFERENCES

- Anderson, D.L.T. and P.B. Rowlands, 1976: The Somali Current response to the Southwest Monsoon: the relative importance of local and remote forcing. *J. Mar. Res.*, 34, 395-417.
- Arthur, R.S., 1960: A review of the calculation of ocean currents at the equator. *Deep-Sea Res.*, 6, 287-297.
- Cane, M., 1979: On the dynamics of equatorial currents, with application to the Indian Ocean. (Unpublished manuscript.)
- Charney, J., 1960: Non-linear theory of a wind driven homogeneous layer near the equator. *Deep-Sea Res.*, 6, 303-310.
- Cochrane, J.D., F.J. Kelly and C.R. Olling, 1979: Subthermocline countercurrents in the western equatorial Atlantic Ocean. *J. Phys. Oceanogr.*, 9, 724-738.
- Colin, C., C. Henin, P. Hisard and C. Oudot, 1971: Le Courant de Cromwell dans le Pacifique central en février. *Cah. Orstom, Ser. Oceanogr.*, 9, 167-186.
- Crawford, W.R., 1976: Turbulent energy dissipation in the Atlantic Equatorial Undercurrent. Ph.D. dissertation, University of British Columbia, 150 pp.
- Cromwell, T., 1953: Circulation in a meridional plane in the central equatorial Pacific. *J. Mar. Res.*, 12, 196-213.
- Düing, W., P. Hisard, E. Katz, J. Knauss, J. Miencke, L. Miller, K. Moroshkin, G. Philander, A. Ribnikov, K. Voigt and R. Weisberg, 1975: Meanders and long waves in the equatorial Atlantic. *Nature*, 257, 280-284.
- Ekman, V.W., 1905: On the influence of the earth's rotation on ocean currents. *Ark. f. Mat. Astron. och Fysik*, 2, 1-53.
- Fofonoff, N.P. and R.B. Montgomery, 1955: The Equatorial Undercurrent in light of the vorticity equation. *Tellus*, 7, 518-521.
- Gill, A.E., 1975: Models of equatorial currents. In *Numerical Models of Ocean Circulation*, National Academy of Science, Wash. D.C., 181-203.
- Hellerman, S., 1967: An updated estimate of the wind stress on the world ocean. *Mon. Wea. Rev.*, 95, 607-614.
- Hisard, P., J. Merle and B. Voituriez, 1970: The Equatorial Undercurrent at 170°E in March and April 1967. *J. Mar. Res.*, 28, 281-303.

- Holland, W.R., 1978: The role of mesoscale eddies in the general circulation of the ocean — numerical experiments using a wind-driven quasi-geostrophic model. *J. Phys. Oceanogr.*, 8, 363-392.
- Jones, J.H., 1973: Vertical mixing in the Equatorial Undercurrent. *J. Phys. Oceanogr.*, 3, 286-296.
- Katz, E.J. and collaborators, 1977: Zonal pressure gradient along the equatorial Atlantic. *J. Mar. Res.*, 35, 293-307.
- Knauss, J.A., 1960: Measurements of the Cromwell Current. *Deep-Sea Res.*, 6, 265-286.
- Knauss, J.A., 1963: The equatorial current system. In *The Sea*, Vol. 2, Interscience, New York, 235-252.
- Knauss, J.A., 1966: Further measurements and observations on the Cromwell Current. *J. Mar. Res.*, 24, 205-240.
- Knox, R.A., 1976: On a long series of measurements of Indian Ocean equatorial currents near Addu Atoll. *Deep-Sea Res.*, 23, 211-221.
- Leetmaa, A., J.P. McCreary Jr. and D.W. Moore, 1980: Equatorial currents: observations and theory. To appear in *The Ocean Environment*, MIT Press.
- Lighthill, M.J., 1969: Dynamic response of the Indian Ocean to the onset of the Southwest Monsoon. *Phil. Trans. Roy. Soc.*, A265, 45-92.
- Luyten, J.R. and C.C. Eriksen, 1980: Deep equatorial jets in the Indian and Pacific Oceans. (Unpublished manuscript.)
- Luyten, J.R. and J.C. Swallow, 1976: Equatorial undercurrents. *Deep-Sea Res.*, 23, 1005-1007.
- McCreary, J.P. Jr., 1977: Eastern ocean response to changing wind systems. Ph.D. dissertation, Scripps Institution of Oceanography, University of California, 156 pp.
- McCreary, J.P. Jr., 1980: A linear stratified ocean model of the Equatorial Undercurrent. Submitted to *Phil. Trans. Roy. Soc.*
- Melville, H., 1978: *Moby Dick*. Bobbs-Merrill Educational Publishing, Indianapolis, 730 pp.
- Meyers, G., 1979: Annual variation in the slope of the 14°C isotherm along the equator in the Pacific Ocean. *J. Phys. Oceanogr.*, 9, 885-891.
- Montgomery, R.B. and E.D. Stroup, 1962: Equatorial waters and currents at 150°W in July-August 1952. *Johns Hopkins Oceanographic Studies*, 2, 68 pp.

- Moore, D.W. and S.G.H. Philander, 1977: Modelling the tropical ocean circulation. *The Sea*, Vol. 6, Interscience, New York, 319-361.
- Neumann, G., 1960: Evidence of an Equatorial Undercurrent in the Atlantic Ocean. *Deep-Sea Res.*, 6, 328-334.
- Pedlosky, J., 1969: Axially symmetric motion of a stratified, rotating fluid in a spherical annulus of narrow gap. *J. Fluid Mech.*, 36, 401-416.
- Philander, S.G.H., 1971: The equatorial dynamics of a shallow homogeneous ocean. *Geophys. Fluid Dyn.*, 2, 219-245.
- Philander, S.G.H., 1973a: The equatorial thermocline. *Deep-Sea Res.*, 20, 69-86.
- Philander, S.G.H., 1973b: Equatorial Undercurrent: measurements and theories. *Rev. Geophys. and Space Phys.*, 11, 513-570.
- Philander, S.G.H. and R.C. Pacanowski, 1980: The generation of equatorial currents. Submitted to *J. Geophys. Res.*
- Reiter, E.R., 1978: The interannual variability of the ocean-atmosphere system. *J. Atm. Sci.*, 35, 349-370.
- Robinson, A.R., 1960: The general circulation in equatorial regions. *Deep-Sea Res.*, 6, 311-317.
- Robinson, A.R., 1966: An investigation into the wind as the cause of the Equatorial Undercurrent. *J. Mar. Res.*, 24, 179-204.
- Schneider, E.K. and R.S. Lindzen, 1976: The influence of stable stratification on the thermally driven tropical boundary layer. *J. Atmos. Sci.*, 33, 1301-1307.
- Shukla, J., 1973: Effect of Arabian Sea surface temperature on Indian Ocean summer monsoon: a numerical experiment with the GFDL model. *J. Atm. Sci.*, 32, 503-511.
- Stommel, H., 1955: *The Gulf Stream, A Physical and Dynamical Description*. University of California Press, Berkeley, 248 pp.
- Stommel, H., 1960: Wind drift near the equator. *Deep-Sea Res.*, 6, 298-302.
- Stommel, H. and G. Veronis, 1957: Steady convective motion in a horizontal layer of fluid heated uniformly from above and cooled non-uniformly from below, *Tellus*, 9, 401-407.
- Sverdrup, H.U., 1947: Wind-driven currents in a baroclinic ocean; with application to the equatorial currents of the eastern Pacific. *Proc. Nat. Acad. Sci.*, 33, 318-326.

- Taft, B.A., B.M. Hickey, C. Wunsch and D.J. Baker, 1974: Equatorial Undercurrent and deeper flows in the central Pacific. *Deep-Sea Res.*, 21, 403-430.
- Taft, B.A. and J.A. Knauss, 1967: The Equatorial Undercurrent in the Indian Ocean as observed by the Lusiad Expedition. *Bull. Scripps Inst. Oceanogr.*, 9, 163 pp.
- Titov, V.B., 1977: Meandering of the Cromwell Current. *Oceanology*, 17, 271-273.
- Tsuchiya, M., 1975: Subsurface countercurrents in the eastern equatorial Pacific Ocean. *J. Mar. Res.*, 33, 145-175.
- Turner, J.S., 1973: *Buoyancy Effects in Fluids*. Cambridge University Press, London, 367 pp.
- Veronis, G., 1960: An approximate theoretical analysis of the Equatorial Undercurrent. *Deep-Sea Res.*, 6, 318-327.
- Wunsch, C. and A.E. Gill, 1976: Observations of equatorially trapped waves in sea level observations. *Deep-Sea Res.*, 23, 371-391.
- Wyrtki, K. and E. Bennett, 1963: Vertical eddy viscosity in the Pacific Equatorial Undercurrent. *Deep-Sea Res.*, 10, 449-455.
- Wyrtki, K. and G. Meyers, 1975: The Trade Wind Field over the Pacific Ocean, Part I. The mean field and mean annual variation. *Tech. Rep.*, Hawaii Inst. of Geophys.
- Yoshida, K., 1959: A theory of the Cromwell Current (the Equatorial Undercurrent) and of equatorial upwelling — an interpretation in a similarity to a coastal circulation. *J. Oceanogr. Soc. Jap.*, 15, 159-170.

MANADATORY DISTRIBUTION LIST
FOR UNCLASSIFIED TECHNICAL REPORTS, REPRINTS & FINAL REPORTS
PUBLISHED BY OCEANOGRAPHIC CONTRACTORS
OF THE OCEAN SCIENCE AND TECHNOLOGY DIVISION
OF THE OFFICE OF NAVAL RESEARCH
(Revised July 1978)

Department of Defense

Office of the Secretary of Defense (3)
Assistant Director of Defense Research
& Engineering
Washington, D.C. 20301

Naval Research Laboratory (6)
Library, Code 2620
Washington, D.C. 20375

U.S. Naval Oceanographic Office
Library, Code 8170
NSTL Station
Bay St. Louis, MS 39529

Navy

Office of Naval Research (3)
Code 460
Arlington, VA 22217

Office of Naval Research
Code 480
Arlington, VA 22217

Office of Naval Research
Code 102 B
Arlington, VA 22217

Office of Naval Research (6)
Code 102 DI
Arlington, VA 22217

Office of Naval Research
Commanding Officer
1030 East Green Street
Pasadena, CA 91101

Naval Ocean Research & Development
Activity
NORDA, Code 300
NSTL Station
Bay St. Louis, MS 39529

Other Government Agencies

Defense Documentation Center (12)
Cameron Station
Alexandria, VA 22314

National Oceanic & Atmospheric
Administration
National Oceanographic Data Center
Washington Navy Yard
Rockville, MD 20852